

**University of Alberta**

Production of arbitrary dose profiles in  
homogeneous phantom by dynamic collimation

by



Marc Alexander MacKenzie

A thesis submitted to the Faculty of Graduate studies and Research in partial  
fulfilment of the requirements for the degree of Master of Science

in

Medical Physics

Department of Physics

Edmonton, Alberta  
Fall 1996



National Library  
of Canada

Acquisitions and  
Bibliographic Services Branch

395 Wellington Street  
Ottawa, Ontario  
K1A 0N4

Bibliothèque nationale  
du Canada

Direction des acquisitions et  
des services bibliographiques

395, rue Wellington  
Ottawa (Ontario)  
K1A 0N4

*Your file* *Votre référence*

*Our file* *Notre référence*

The author has granted an irrevocable non-exclusive licence allowing the National Library of Canada to reproduce, loan, distribute or sell copies of his/her thesis by any means and in any form or format, making this thesis available to interested persons.

L'auteur a accordé une licence irrévocable et non exclusive permettant à la Bibliothèque nationale du Canada de reproduire, prêter, distribuer ou vendre des copies de sa thèse de quelque manière et sous quelque forme que ce soit pour mettre des exemplaires de cette thèse à la disposition des personnes intéressées.

The author retains ownership of the copyright in his/her thesis. Neither the thesis nor substantial extracts from it may be printed or otherwise reproduced without his/her permission.

L'auteur conserve la propriété du droit d'auteur qui protège sa thèse. Ni la thèse ni des extraits substantiels de celle-ci ne doivent être imprimés ou autrement reproduits sans son autorisation.

ISBN 0-612-18294-0

**Canada**

**University of Alberta**

**Library Release Form**

Name of Author: Marc Alexander MacKenzie

Title of Thesis: Production of Arbitrary dose profiles in homogeneous phantom by dynamic collimation

Degree: Master of Science

Year this Degree Granted: 1996

Permission is hereby granted to the University of Alberta Library to reproduce single copies of this thesis and to lend or sell such copies for private, scholarly, or scientific purposes only.

The author reserves all other publication and other rights in association with the copyright in the thesis, and except as hereinbefore provided neither the thesis nor any substantial portion thereof may be printed or otherwise reproduced in any material form whatever without the author's prior written permission.



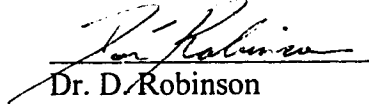
10644 65 Ave.  
Edmonton, AB  
T6H 1V4


August 12, 1996

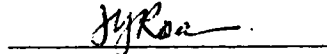
**University of Alberta**

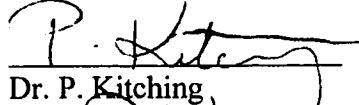
**Faculty of Graduate Studies and Research**

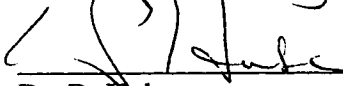
The undersigned certify that they have read, and recommended to the Faculty of Graduate Studies and Research for acceptance, a thesis entitled **Production of arbitrary dose profiles in homogeneous phantom by dynamic collimation** submitted by **Marc Alexander MacKenzie** in partial fulfilment of the requirements for the degree of **Master of Science in Medical Physics**.

  
Dr. D. Robinson

  
Dr. R. Sloboda

  
Dr. W. Roa

  
Dr. P. Kitching

  
Dr. D. Hube

August 6, 1996

## ***Abstract***

Radiotherapy seeks to deliver a homogeneous tumouricidal dose to a volume which encompasses the gross tumour and subclinical invasions. This often requires the use of a number of radiation fields, some of which may have non-uniform intensity profiles in order to correct for tissue heterogeneities, surface irregularities, and, in general, to conform high dose regions closely to the clinical target volume. Such dose distributions are realised largely with static physical attenuators and, more recently, dynamic wedging. Advanced computerised linac control allows for the unidirectional sweep of opposing collimator jaws independently across a field during beam delivery, generating arbitrary one-dimensional dose distributions at depth in phantom; this is called dynamic compensation.

A model is presented for calculating required jaw motions to produce arbitrarily shaped one dimensional dose profiles at depth in a homogeneous phantom, or a one dimensional energy fluence profiles in air, with a proof of treatment time optimisation. This model accounts for the variation in output across the field due to the varying field sizes employed during dynamic treatment, for the variation due to non-uniformity of the primary fluence, and for changes in the fluence due to penumbral effects. The required energy fluence profile for a desired dose profile is achieved by iterative dose calculation and correction. This model is tested by comparing desired dose and fluence profiles with corresponding measurements of these quantities realised using dynamic compensation.

### *Acknowledgements*

I would like to offer my deep and sincere thanks to everyone who supported me throughout my efforts in this degree and throughout my research. In general, I would like to thank everyone in the Medical Physics Department for providing a supportive, friendly and productive atmosphere. I would also like to thank all my fellow graduate students in Physics who have become good friends, and all the faculty and staff of the Physics Department who have been helpful with courses and administrative details. At the risk of forgetting someone, I would nonetheless like to thank in particular:

A great number of professors who have taught or mentored me during my undergraduate degree, notably Drs. Hussein, Sharp, Lees, DeMille, Ross, Ross and Young.

All of the non-medical physics graduate students for their friendship.

HJ Kim, Lara Dyke and Parminder Basran for the always interesting and/or amusing conversations, and for, as applicable, the occasional pain killer, lending me bus change and keeping the coffee coming.

John Kollar for many an intriguing conversation on late nights, and for the whiteboard art work.

I would like to thank my supervisor Don Robinson for all his valuable guidance, and for many a useful blackboard session, as well as for all his general support.

Finally, I would like to thank most of all my wife, Christine Lesiak, for her continual support, love and understanding throughout my work on this degree. I would also like to thank my cats, Max and Zoot, and my dog Zachary, for being relatively domesticated.

## TABLE OF CONTENTS

	<u>Page</u>
<b>Chapter 1    Introduction.....</b>	<b>1</b>
<b>1.1    Cancer Basics.....</b>	<b>1</b>
<b>1.2    Treatment Procedures and Modalities.....</b>	<b>1</b>
<b>1.3    External Beam Radiotherapy.....</b>	<b>2</b>
1.3.1    Treatment Planning.....	2
1.3.2    Conformal Radiotherapy.....	4
1.3.2.1    Open Field Combinations.....	4
1.3.2.2    Wedged and Open Field Combinations.....	7
1.3.2.3    Tissue Compensators.....	10
1.3.2.4    Dynamic Wedge.....	11
<b>1.4    Development of Dynamic Compensation.....</b>	<b>14</b>
 <b>Chapter 2    Basics of Radiotherapy and Radiation Physics.....</b>	 <b>20</b>
<b>2.1    Definitions of Basic Radiation Units.....</b>	<b>20</b>
<b>2.2    Radiation Interactions.....</b>	<b>21</b>
2.2.1    Ionising Radiation Fields.....	21
2.2.2    Radiation Interactions in Matter.....	22
2.2.2.1    Photoelectric Effect.....	24
2.2.2.2    Compton Effect.....	24
2.2.2.3    Pair Production.....	25
2.2.2.4    Rayleigh Scattering.....	26
2.2.2.5    Photonuclear Interactions.....	26
2.2.3    Dose Deposition.....	26
2.2.3.1    Radiative and Collision Events.....	27
2.2.3.2    Stopping Powers.....	28
2.2.3.3    Charged Particle Equilibrium.....	29
2.2.3.4    Kerma and Dose.....	30
<b>2.3    Beam Production.....</b>	<b>31</b>
2.3.1    Pre Target Mechanisms.....	32
2.3.2    Gantry Head Physics.....	34
<b>2.4    Beam Measurements.....</b>	<b>38</b>

2.4.1	General Field Descriptors.....	38
2.4.1.1	Percent Depth Dose.....	38
2.4.1.2	Tissue Air Ratio.....	39
2.4.1.3	Scatter Air Ratio.....	39
2.4.2	Ion chambers.....	40
2.4.3	Diodes.....	42
2.4.4	Radiographic film.....	43
<b>Chapter 3</b>	<b>Dynamic Field Techniques.....</b>	<b>45</b>
<b>3.1</b>	<b>Field Delivery.....</b>	<b>45</b>
3.1.1	Dynamic Simulation with Summed Fields....	45
<b>3.2</b>	<b>Calculation Techniques.....</b>	<b>46</b>
3.2.1	Wedge Calculation.....	48
3.2.2	Numerical Optimisation.....	50
3.2.2.1	Simplex.....	51
3.2.2.2	Simulated Annealing.....	54
3.2.3	Analytic Solution.....	55
<b>3.3</b>	<b>Dynamic Field Corrections.....</b>	<b>58</b>
3.3.1	Relative Output Off the CAX (AOF).....	58
3.3.1.1	Determination of AOF Values.....	59
3.3.2	Relative Output with Field Size (ROF).....	61
3.3.2.1	Determination of ROF Values.....	62
3.3.3	Collimation and Penumbra Effects.....	64
3.3.3.1	Modelling of Penumbra.....	66
<b>3.4</b>	<b>Dose Calculation.....</b>	<b>73</b>
3.4.1	Calculation Technique.....	73
3.4.2	Evaluation of Dose Algorithm.....	79
3.4.3	Iterative Correction.....	80
<b>3.5</b>	<b>Dynamic Field Verification.....</b>	<b>80</b>
3.5.1	Comparisons.....	81
3.5.1.1	Predicted Fluence.....	81
3.5.1.2	Dose Profiles Using ATP.....	84
3.5.2	Beam Measurements.....	84
3.5.2.1	Fluence Measurements.....	84
3.5.2.1.1	Film.....	84
3.5.2.1.2	Diode.....	85
3.5.2.1.3	Ion Chamber.....	85
3.5.2.1.4	Ion Chamber Array....	86
3.5.2.2	Dose Measurements.....	86
3.5.2.2.1	Film.....	86



3.5.2.2.2	Ion Chamber Array....	87
-----------	-----------------------	----

<b>Chapter 4</b>	<b>Results.....</b>	<b>88</b>
4.1	<b>Dosimeters.....</b>	<b>88</b>
4.1.1	Fluence Measurements.....	88
4.1.2	Dose Measurements.....	93
4.2	<b>Corrections.....</b>	<b>95</b>
4.2.1	AOF Corrections.....	95
4.2.2	ROF Corrections.....	97
4.2.3	Penumbral Model and Corrections.....	100
4.3	<b>Dynamic Fluence Profiles.....</b>	<b>107</b>
4.4	<b>Dynamic Dose and Isodose Profiles.....</b>	<b>118</b>
<b>Chapter 5</b>	<b>Discussion and Conclusions.....</b>	<b>127</b>
5.1	<b>Calculation.....</b>	<b>127</b>
5.2	<b>Dosimetry.....</b>	<b>128</b>
5.3	<b>Corrections.....</b>	<b>129</b>
5.4	<b>Simulated DBD.....</b>	<b>129</b>
5.5	<b>True DBD.....</b>	<b>130</b>
5.6	<b>Overall Model Evaluation.....</b>	<b>130</b>
5.7	<b>Future Work.....</b>	<b>130</b>
	<b>Bibliography.....</b>	<b>132</b>

*List of Tables*

	<u>Page</u>
Table 3.1      Initial tableau for example Simplex optimisation.....	52
Table 3.2      Final tableau for example Simplex optimisation.....	54

## *List of Figures*

	<u>Page</u>
Figure 1.1	Relevant volumes in radiotherapy..... 3
Figure 1.2	Parallel opposed fields..... 5
Figure 1.3	Four beam arrangement..... 6
Figure 1.4	Open vs. wedged fields..... 7
Figure 1.5	Open vs. wedged treatment fields..... 8
Figure 1.6	Two wedge field..... 8
Figure 1.7	Three field arrangement with open and wedged field..... 9
Figure 1.8	Use of bolus in treatment..... 10
Figure 1.9	Use of retracted field compensator..... 11
Figure 1.10	Realisation of standard and dynamic wedged fields..... 12
Figure 1.11	Standard wedge and dynamic wedge isodoses..... 13
Figure 1.12	Gross machine parameters..... 15
Figure 1.13	Gantry head parameters..... 16
Figure 1.14	Simple dynamic treatment..... 17
Figure 1.15	More complex dynamic treatment..... 18
Figure 2.1	Photon interactions in matter..... 23
Figure 2.2	Photoelectric effect..... 24
Figure 2.3	Compton effect..... 25
Figure 2.4	Dose deposition in matter..... 27
Figure 2.5	Charged particle equilibrium..... 29

Figure 2.6	Beam production in typical linac.....	32
Figure 2.7	The cylindrical waveguide.....	33
Figure 2.8	The cylindrical waveguide with disks.....	33
Figure 2.9	The cylindrical waveguide with off-axis coupled chambers.	34
Figure 2.10	The gantry head.....	35
Figure 2.11	Relative energy fluence in air.....	37
Figure 2.12	Percent depth dose.....	38
Figure 2.13	Tissue air ratio.....	39
Figure 2.14	Scatter air ratio.....	40
Figure 2.15	Cylindrical ion chamber.....	41
Figure 2.16	Semiconductor diode detector.....	43
Figure 2.17	H & D curve.....	44
Figure 3.1	Effect of step size on dynamic wedge simulations.....	45
Figure 3.2	Flow chart of dynamic compensation.....	47
Figure 3.3	Calculated dose for dynamic wedge treatment.....	49
Figure 3.4	Example relative fluence profile.....	56
Figure 3.5	AOF measurement.....	58
Figure 3.6	AOF factor and in-air beam profile.....	59
Figure 3.7	Measurement of in-air beam profile for a large field.....	60
Figure 3.8	Extrapolation of in-air beam profile for a large field.....	61
Figure 3.9	Measurement of ROF.....	62
Figure 3.10	ROF as a function of field size.....	63

Figure 3.11	ROF from standard and far field settings.....	64
Figure 3.12	Penumbra for a 10x10 field in air.....	65
Figure 3.13	Simple geometric model for penumbra.....	67
Figure 3.14	Extended geometric model for penumbra.....	68
Figure 3.15	Geometry of visible x-ray source.....	69
Figure 3.16	Calculating extent of visible x-ray source.....	70
Figure 3.17	Calculation of a dSAR value.....	74
Figure 3.18	Equivalent circular field calculation.....	75
Figure 3.19	Calculating a dSAR pencil.....	76
Figure 3.20	Calculation of the scatter contribution from slabs.....	77
Figure 3.21	Dose calculation using slabs made using dSAR values.....	78
Figure 3.22	Radii used in calculating slabs.....	79
Figure 3.23	Dose distribution from dSAR technique for open field.....	80
Figure 3.24	Probe response for scanning of slit beam.....	81
Figure 3.25	Probe response for integrated measurement of slit beam.....	82
Figure 3.26	Measuring effect of buildup on fluence measured with film.	83
Figure 4.1	Blurring of signal on film.....	89
Figure 4.2	Experimental set up for measuring blurring.....	89
Figure 4.3	Measured thin slits with and without buildup.....	89
Figure 4.4	Measured vs. predicted (no blurring) open asymm. profiles.	90
Figure 4.5	Measured vs. predicted (w. blurring) open asymm. profiles.	91
Figure 4.6	Thin slits meas. w. ion chamber (acrylic and brass buildup).	92

Figure 4.7	Open field meas. (acrylic and brass buildup) vs. prediction..	93
Figure 4.8	Dynamic wedge isodoses (film and ion chamber array).....	94
Figure 4.9	Desired and modified input profiles.....	96
Figure 4.10	Measured (w. & w.out AOF correction) vs. ideal profile.....	97
Figure 4.11	A second dynamic field, with and without ROF correction..	98
Figure 4.12	Dynamic field generated with and without ROF correction..	99
Figure 4.13	Calculated and measured penumbra.....	100
Figure 4.14	Calculated and measured penumbra (with transmission)....	101
Figure 4.15	Step profile, measured vs. ideal.....	102
Figure 4.16	Predicted (fr. penumbral model) and measured step profile..	103
Figure 4.17	Step profile generated w. and w.out correction, vs. ideal.....	104
Figure 4.18	Symmetric open field (no corrections).....	105
Figure 4.19	DBD flattened symmetric open field (AOF corrections).....	105
Figure 4.20	DBD flattened symm. open field (AOF, ROF corrections)...	106
Figure 4.21	DBD flattened symm. field (AOF, ROF, pen. corrections)...	106
Figure 4.22	Electrometer measurement versus monitor unit setting.....	107
Figure 4.23	Film vs. ion chamber array, true DBD; simple wedge.....	108
Figure 4.24	Film vs. ion chamber array, true DBD; split wedge.....	109
Figure 4.25	Film vs. ion chamber array (true DBD); step profile.....	110
Figure 4.26	True DBD vs. sum of static fields, film; simple wedge.....	111
Figure 4.27	True DBD vs. sum of static fields, film; split wedge.....	112

Figure 4.28	Desired and predicted fluence profile (ion chamber array); simple wedge.....	113
Figure 4.29	Desired and predicted fluence profile (ion chamber array); split wedge.....	114
Figure 4.30	Desired and predicted fluence profile (ion chamber array); multiple split wedge.....	115
Figure 4.31	Complex fluence profile, fr. summed static fields (film).....	116
Figure 4.32	Complex profile, true DBD field (ion chamber array).....	117
Figure 4.33	ATP dynamic wedge isodose calc. vs. measured isodose.....	118
Figure 4.34	ATP isodoses for Varian STT and STT from model.....	119
Figure 4.35	ATP isodose for STT for dyn. flattening at 20cm depth.....	121
Figure 4.36	Measured profiles, open (20cm depth) vs. desired flat.....	122
Figure 4.37	Open and DBD flattened profile, measured vs. desired.....	123
Figure 4.38	Relative dose wedge, measured at 10cm depth.....	124
Figure 4.39	Relative dose split wedge, measured at 10cm depth.....	125
Figure 4.40	Relative dose complex profile, measured at 10cm depth.....	126

### *List of Symbols*

D	Dose
E	Energy
h	Planck's constan.
K	Kerma
L	Stopping power
S	Restricted stopping power
X	Exposure
Z	Atomic number (number of electrons/protons)
$\rho$	Density
$\sigma$	Interaction cross-section
$\Omega$	Solid angle
$\mu$	Linear attenuation coefficient
$\nu$	Frequency
$\Phi$	Fluence
$\phi$	Fluence rate
$\Psi$	Energy fluence
$\psi$	Energy fluence rate
$\delta$	Delta ray
$\gamma$	Photon
$\kappa$	Pair production interaction cross-section



- $\tau$       Photoelectric effect interaction cross-section
- $\omega$       Angular frequency

*List of Abbr.*

Abbr.	Abbreviations
ACB	Alberta Cancer Board
AECB	Atomic Energy Control Board
AECL	Atomic Energy of Canada Limited
AOF	Asymmetric Output Factor
CAX	Central Axis
CCI	Cross Cancer Institute
CTV	Clinical Treatment Volume
DBD	Dynamic Beam Delivery
Dmax	Depth of maximum dose
dSAR	differential Scatter Air Ratio
f.s.	field size
GI	Gastro intestinal
GTV	Gross Tumour Volume
ICRP	International Commission on Radiological Protection
ICRU	International Commission on Radiation Units and Measurements
IEC	International Electrotechnical Commission
IV	Irradiated volume
KERMA	Kinetic Energy Released per unit MAss
MLC	Multileaf Collimator

MU	Monitor Units
OD	Optical Density
PDD	Percent Depth Dose
PTV	Planning Treatment Volume
RBE	Radiobiological Effects
ROF	Relative Output Factor
SAD	Source to Axis Distance
SAR	Scatter Air Ratio
SBD	Source to Bottom of jaw Distance
SDD	Source to Detector Distance
SJD	Source to Jaw Distance
STD	Source to Top of jaw Distance
SSD	Source to Surface Distance
TAR	Tissue Air Ratio
TAR0	Tissue Air Ratio for zero field size

## Chapter 1

### Introduction

#### 1.1 Cancer Basics

Cancer is a class of diseases characterised by the unchecked and improper proliferation of a single cell into a tumorous mass. Broadly, it encompasses four main groups: carcinomas, which are epithelial in origin, sarcomas, which arise from connective tissues, leukaemias which arise from the cells of the bone marrow and lymphomas which arise from the cells of the immune system. Tumours may be benign, that is to say localised and non-invasive to surrounding tissue, or malignant, which may be locally invasive or capable of metastasis (i.e. spreading to distal locations); it is the malignant tumours which are known as cancers.

Cancer is responsible for about 40, 000 deaths a year in Canada, and 500, 000 deaths a year in the United States [Rubin 1993]. Radiation therapy is used to treat tumours in approximately 55% of all cases here in Alberta [Field 1988], either alone or in conjunction with other treatment modalities, and either with curative or palliative intent. The benefit of modern radiation treatment is evident when one examines the survival figures of those receiving treatment today as compared to those who received treatment in the past [Johns and Cunningham 1983].

#### 1.2 Treatment Procedures and Modalities

Once a patient has been diagnosed with a possible cancer their treatment will go through a number of steps. Firstly, the diagnosis must be confirmed. The tumour then is staged on a scale from one to four: stage 1 represents a totally localised tumour, and 4 represents a tumour with distal metastatic involvement [Rubin 1993]. Once a tumour has been confirmed and staged a treatment plan may be formulated. The physician will then decide on the best course of action.

If the tumour is deemed treatable, then a treatment modality, or combination of modalities will be selected. If the tumour cannot be treated with a curative intent, then a course of palliative treatment may be prescribed. In broad terms, there are three main treatment modalities for cancer: surgical intervention, chemotherapy, and radiation therapy. Surgical intervention involves the resection of the primary tumour, as well as perhaps the regional lymph nodes, depending on the staging of the tumour. A round of chemotherapy involves the administration of drugs which seek to inhibit the growth of the tumour by blocking the enzymatic pathways used by the tumour cells for proliferation. Radiation therapy seeks to deliver a radiation dose to the tumorous region sufficient to kill all tumour cells present; this may be accomplished with external beam radiation (also called teletherapy; this involves photons, electrons,

or heavy particles), by direct application of a radiation source to the mass, called brachytherapy, or by introducing certain radiopharmaceuticals, such as  $\text{NaI}^{131}$ , directly into the patient's bloodstream. Cancer therapy is commonly multidisciplinary over these treatment modalities, with adjuvant therapies being prescribed to complement each other (e.g. surgical resection, such as a mastectomy, coupled with radiation therapy to kill any remaining cancer cells, and thus to help guard against future recurrence of the tumour).

### **1.3 External Beam Radiotherapy**

In the treatment of cancer, radiation therapy can lay claim to being one of the oldest modalities, with radioactivity being used very shortly after its discovery by Becquerel in 1896 to treat skin lesions [Carrier and Cormack 1995]. It is no surprise that over the nearly one hundred years which have followed, significant improvements in both the techniques and results of radiation therapy have been realised. With the invention of the cobalt teletherapy unit here in Canada in the 1950's, external beam radiotherapy became a far more useful tool in the fight against cancer and a new era was ushered in for radiotherapy [Urtasun 1992].

Any treatment that involves external beam radiation will require a treatment plan which defines a planning treatment volume (PTV), as well as the dose that will be delivered, and the dose delivery schedule (number of ports, fractionation, dose per port). The oncologist will draw up such a plan, sometimes with the help of a physicist. Dosimetrists will then formulate beam arrangements, as well as the shape and relative weighting of each beam. Finally, radiation technologists will execute the plan over a number of treatment sessions.

In this work, external x-ray beams shall be looked at exclusively.

#### **1.3.1 Treatment Planning**

Treatment planning has, since the beginning, always had a goal that has remained constant - the delivery of a uniform tumouricidal dose to a tumour volume while minimising the dose to surrounding healthy tissue and sparing sensitive organs. This goal has become further refined in recent years to include a number of standard defined volumes [ICRU 1993] that are involved in radiotherapy treatment planning. These are pictured in figure 1.1.

The gross tumour volume (GTV) is the visible, palpable portion of the tumour mass. The clinical target volume (CTV) includes the GTV, as well as an area around the tumour which includes the microscopic invasions of tumour cells; this is the volume of clinical concern that must receive a net tumouricidal dose during the course of treatment. The planning target volume (PTV) is a still larger volume that encompasses the CTV. This is the volume which will have to be treated with a tumouricidal dose in order for the CTV to receive a tumouricidal dose. It is larger

than the CTV since the CTV may move during the course of treatment due to positioning errors, changes in internal organ positions, or patient movements during treatment; the PTV allows for this motion, and will be much larger than the CTV in certain cases (such as lung tumours), and very close to the shape of the CTV in other cases (such as with small skin tumours).

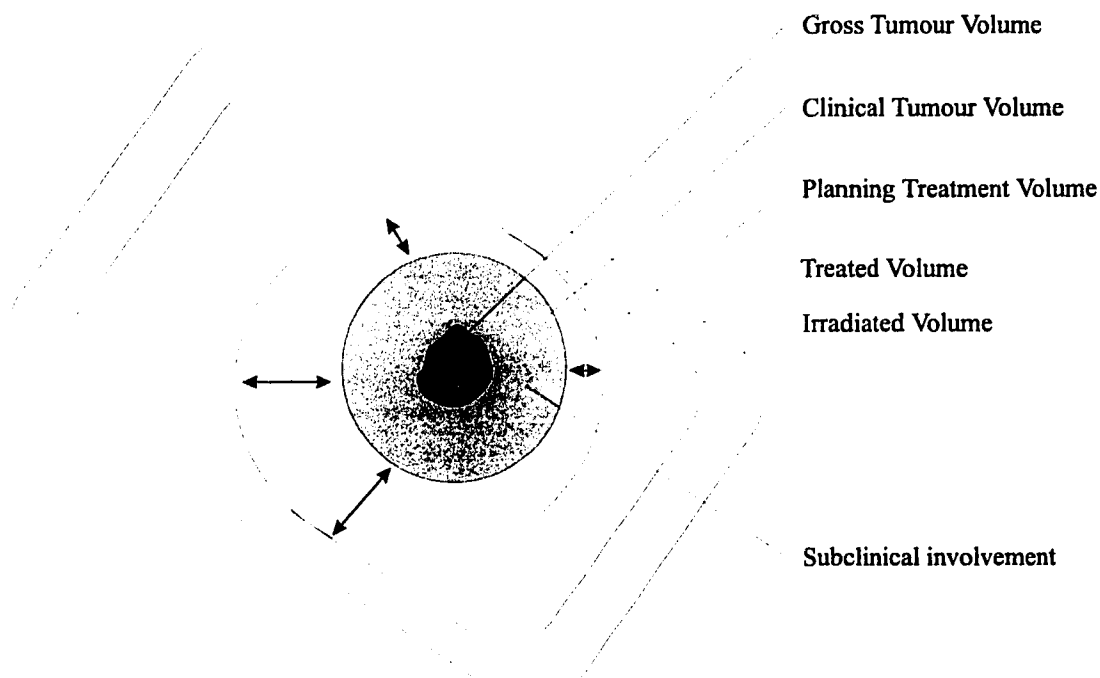


*Figure 1.1 Schematic of volumes relevant to radiotherapy.*

Ideally, the PTV would be the volume planned for irradiation, but due to limitations in technique, the treated volume (TV) is the volume which must be planned for (and which receives a tumouricidal dose). These limitations are in part imposed by beam arrangement in order to attempt to spare sensitive structures (e.g. the spinal cord), and also due to unavoidable irradiation of the tissue above and below the tumour along the beam path. The irradiated volume (IV) is the volume which, although not receiving a tumouricidal dose, receives a dose that is considered significant in relation to normal tissue tolerance (e.g. greater than 50% of the dose specified for target dose).

The achievement of improved dose distributions is thought to lead to increased local tumour control [Spirou and Chui 1994; Urtasun 1992]. In order to achieve this, a typical treatment plan will employ a number of fields (also called portals, often simply called ports). As well, delivering the desired dose distribution at

depth may require the use of non-uniform intensity profiles in order to correct for tissue heterogeneities, such as body cavities like the lung or GI tract (it is normally assumed that tissue is water equivalent) and surface irregularities (i.e., a non-flat body contour), as well as to conform the high dose regions as closely as possible to the treatment volume. Finally, the treatment must take into account the radiosensitivity of certain organs, a notable example already mentioned being the spinal cord. The goal of achieving a treatment volume which is identical to the planning treatment volume is referred to as conformal radiotherapy.

### **1.3.2 Conformal Radiotherapy**

A number of techniques exist to achieve the desired dose distribution within a PTV. A treatment may employ multiple fields in order to realise the desired level of dose homogeneity. As well, for a given treatment field, beam modifying devices such as bolus, lead or steel wedges, retracted tissue compensators, or specially constructed shielding blocks may be employed. These are used either to shape a beam, as in the case of shielding blocks, or to achieve a differential distribution of radiation across the field. A combination of beam modifying devices and multiple treatment fields is often used.

#### **1.3.2.1 Open Field Combinations**

The simplest treatment field is an open field (at left, figure 1.2). The characteristics of the photon beam from a medical linear accelerator impinging on the flat surface of a homogeneous tissue equivalent volume are well known [Khan 1994; Johns and Cunningham 1983]. Notable features are the homogeneous dose profiles normal to the beam (within a few percent through most of the field), and the decrease of this dose with depth in a well defined manner, defined along the central beam axis (CAX) as the percent depth dose (PDD) -- cf. 2.4.1.1.

For most treatments, multiple fields are used to treat a tumour volume. There are several advantages to using multiple field arrangements. With the use of several ports, it is possible to achieve a relatively homogeneous dose distribution. As well, it becomes possible to conform the net dose distribution more closely to the PTV, the dose to the tissue outside the PTV can be lowered, and one may more easily plan to avoid critical organs. A relatively simple multiple beam arrangement would be the parallel opposed open beam pair (see figure 1.2, at right).

Slightly more complex set-ups are often used and, through these techniques, varying degrees of dose homogeneity can be realised. Using open fields, one can achieve still greater homogeneity with a four beam arrangement (see figure 1.3).

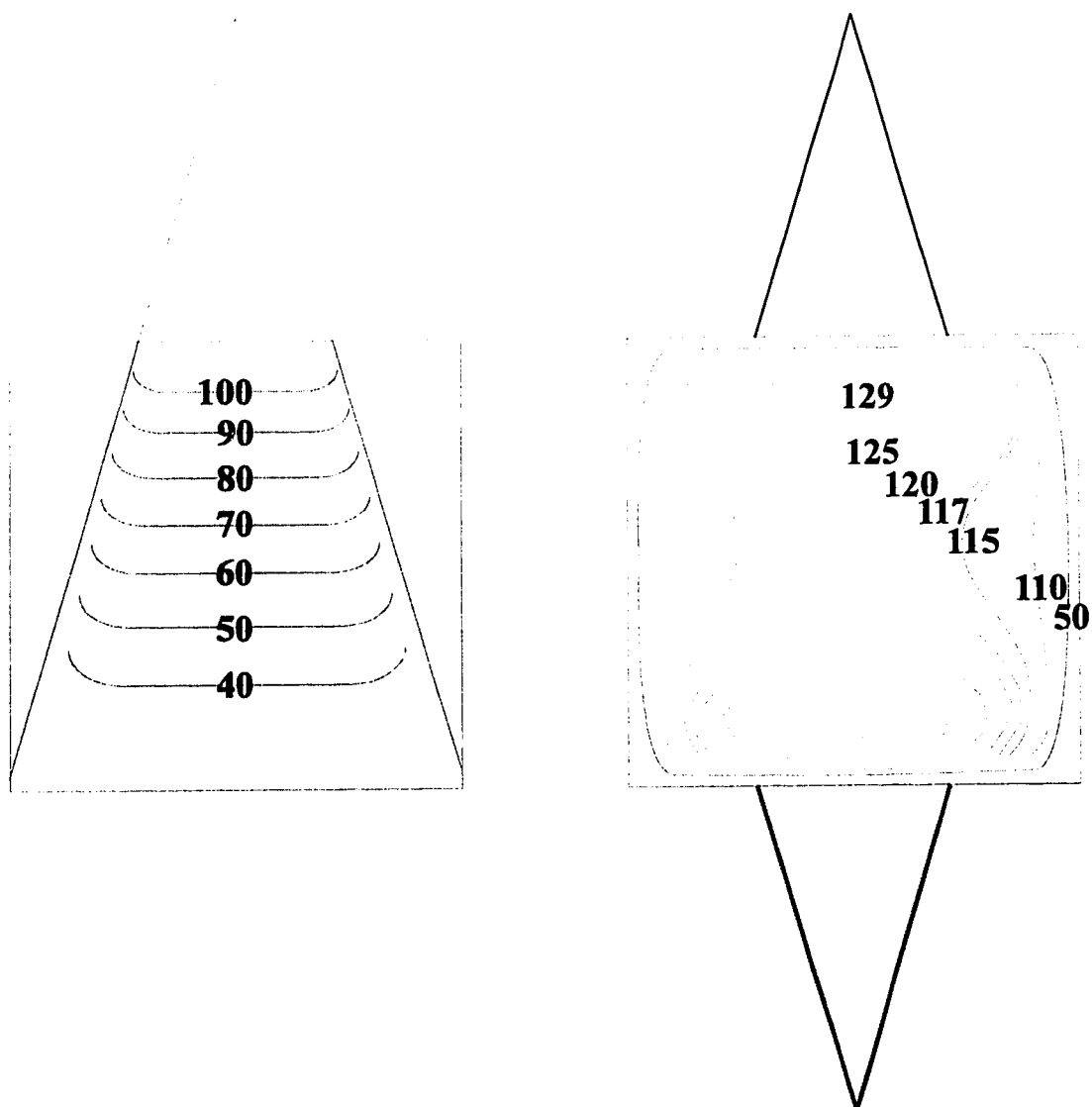


*Figure 1.2 Isodose distributions for an open beam on a flat phantom (left), and a parallel opposed open beam arrangement (right), with equal beam weightings of 100 at  $D_{\max}$  (the depth of maximum dose).*



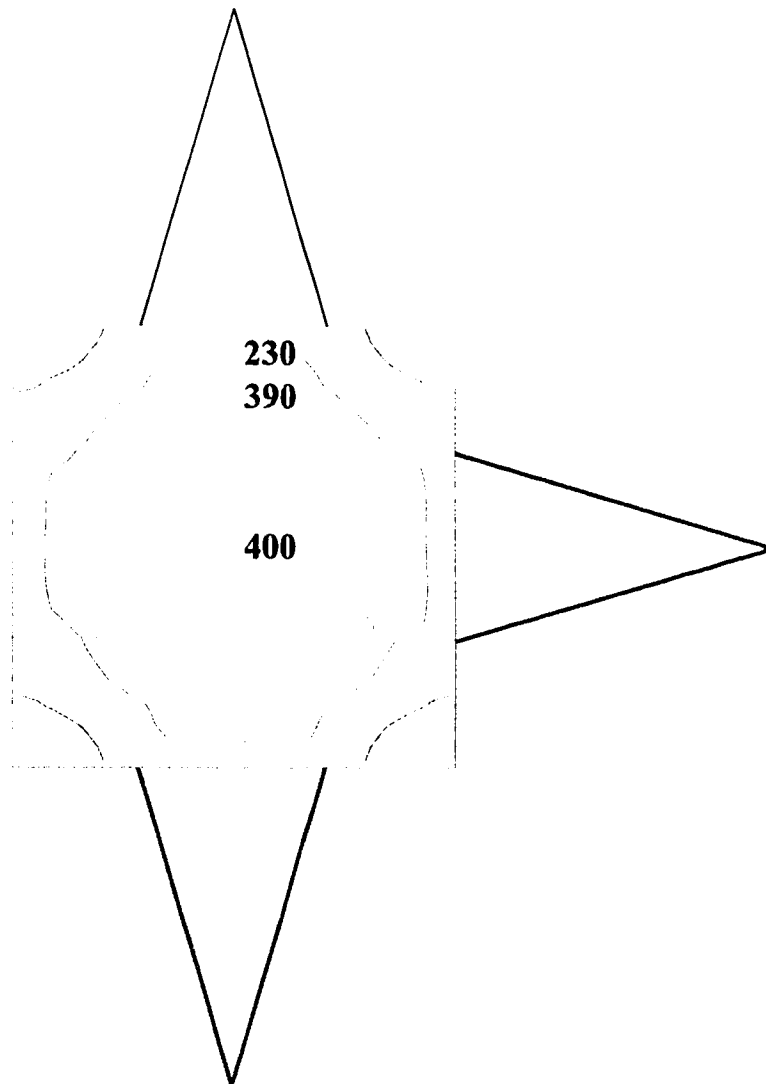


*Figure 1.3 The isodose distributions for a four open beam arrangement, with equal beam weightings of 100 at isocentre (which is located at the phantom centre in this case).*

### 1.3.2.2 Wedged and Open-Wedged Field Combinations

The application of wedged fields is a fairly common example of the use of a beam modifying device. 15, 30, 45 and 60 degree lead or steel wedges are standard in radiotherapy. They produce a tilt of 15, 30, 45 and 60 degrees in the isodose line passing through the point on the central axis (CAX) at 10 cm depth in a flat water phantom for at least 1/4 of the field size in both directions from the CAX (see figure 1.4).

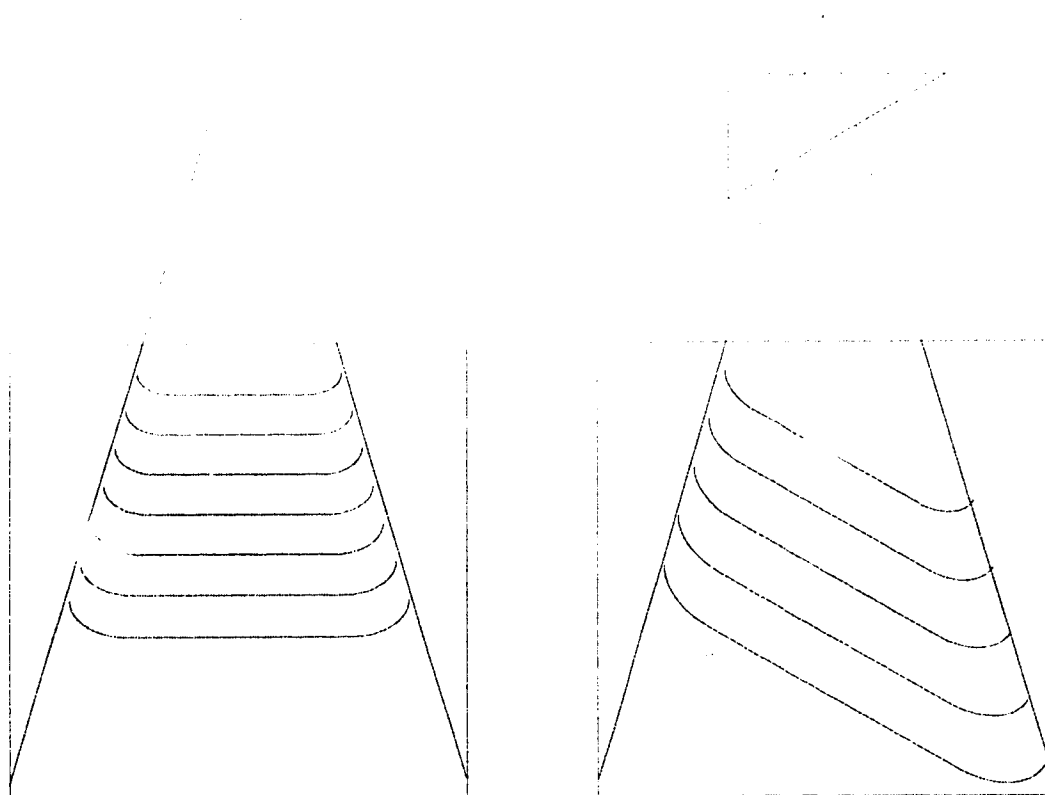


*Figure 1.4 A comparison of an open field isodose profile to a standard wedge isodose profile.*

These wedges find limited use in correcting for one dimensional uniform grades (see figure 1.5), or internal inhomogeneities with very simple geometries. In order to correct for more complex grades or inhomogeneities, retracted compensators may be employed, but these are both time consuming and costly to manufacture, and are specific to one individual field and patient.

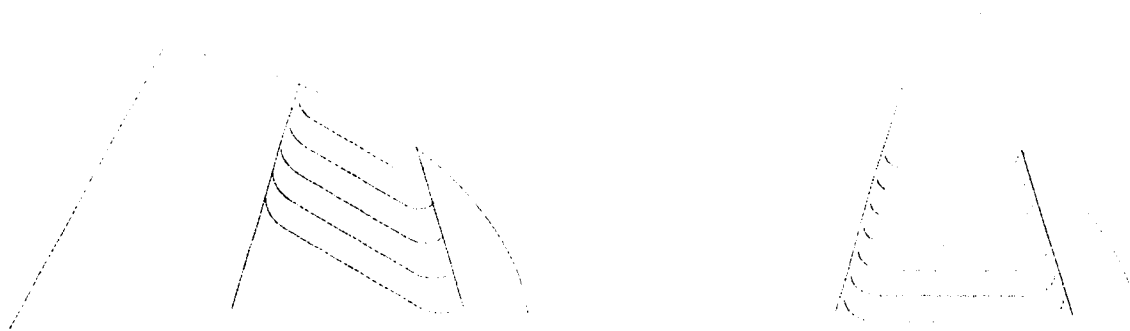


*Figure 1.5 A comparison of an uncompensated and compensated (wedged, in this case) isodose profile for a treatment field.*

There are a number of drawbacks to using the solid wedge. If the physical attenuator is made of high  $Z$  material, the beam hardening (i.e. loss of low energy components in the beam energy spectrum) which results is not always fully taken into account by many current treatment planning algorithms. As well, the wedge affects the beam characteristics by introducing low energy scatter that increases the surface dose to the patient, and it distorts beam flatness in the non-wedged direction. The wedge also has a maximum field size with which it can be used, and there is a degree of uncertainty in positioning it that introduces some variability in dosimetry.

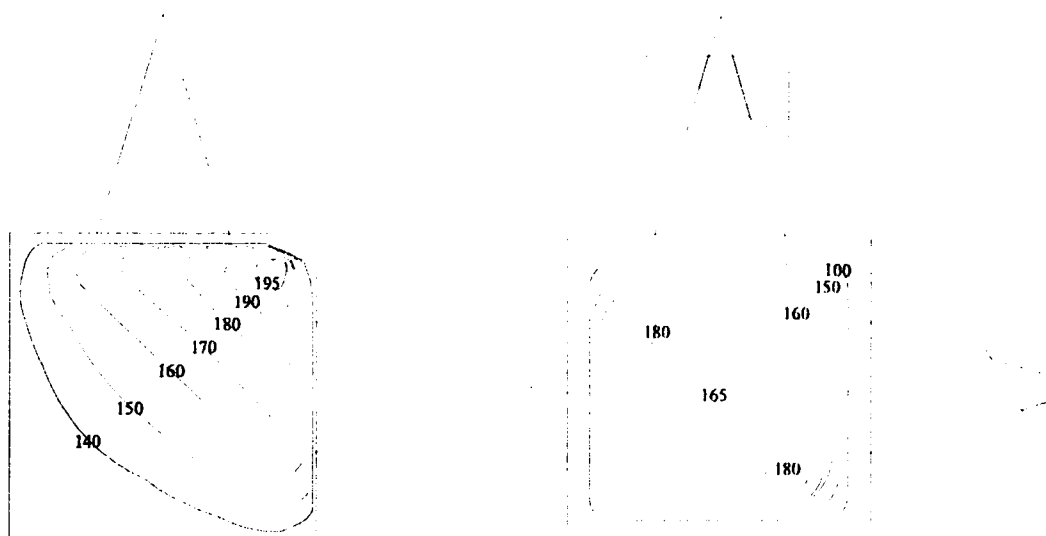


*Figure 1.6 A comparison of angled field treatment isodose distributions for two open (left) and two wedged (right) fields.*

Wedged fields are often used in combination with open fields and other wedged fields to achieve greater degrees of dose homogeneity about a tumour. Two open orthogonal fields, such as might be used to treat a superficial tumour volume, result in a very non-uniform dose distribution (figure 1.6, left). By wedging these two fields, the dose homogeneity can be significantly improved (figure 1.6, right).

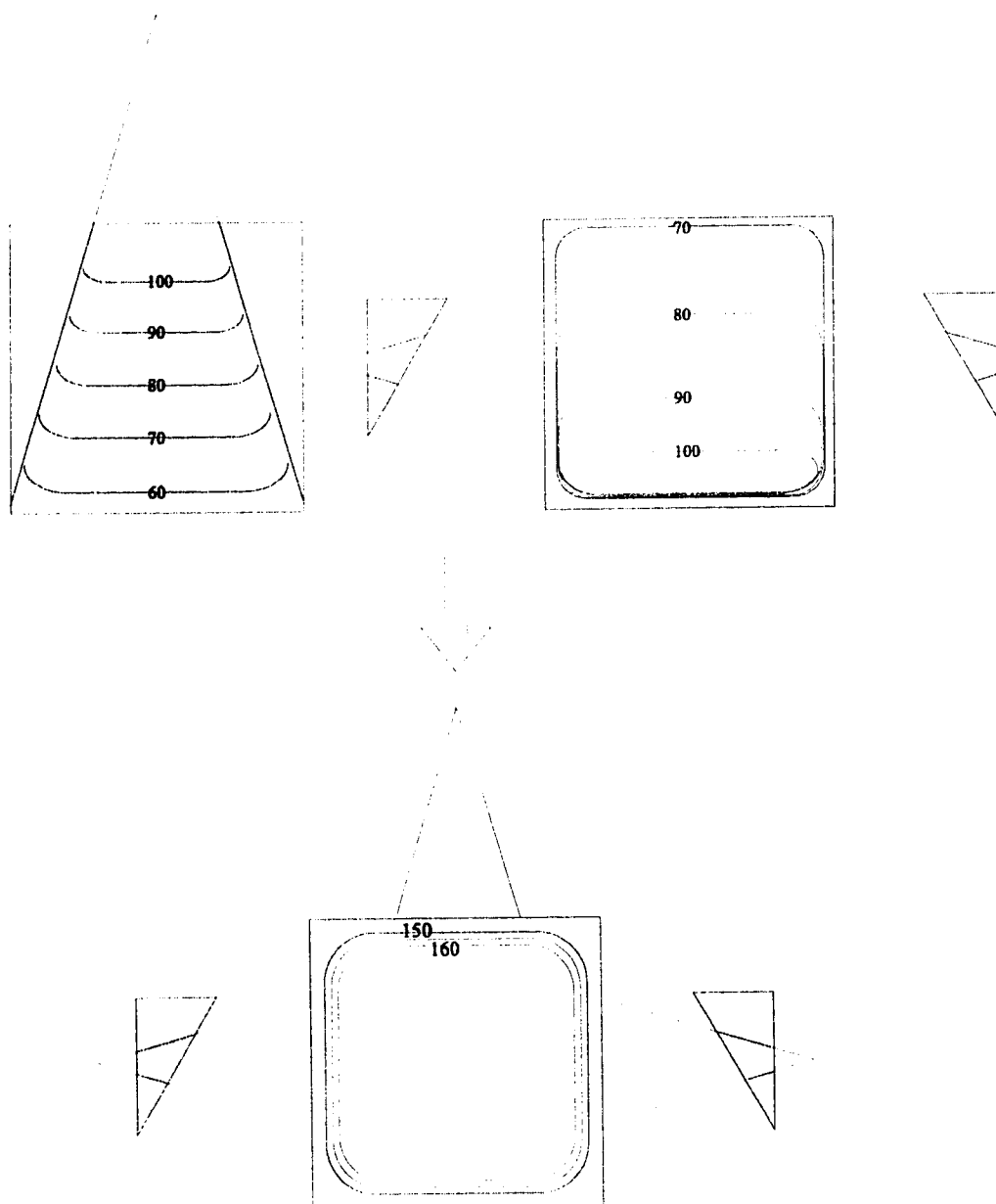


*Figure 1.7 A three field treatment, using two wedged and one open field.*

Open and wedged fields may also be employed in a treatment plan to achieve improved dose homogeneity within a given field. In the example in figure 1.7, a single open and two parallel opposed wedged fields are combined to achieve a high degree of dose homogeneity. This particular use of wedged fields is referred to as dose gradient compensation.

### 1.3.2.3 Tissue Compensators

Bolus is tissue equivalent material that is placed directly against the patient (see figure 1.8). This serves to either provide additional build-up to bring the depth of maximum dose,  $d_{\max}$ , to the patient surface, or to level out patient contours -- a non-retracted tissue compensator. Use as an unretracted compensator can be undesirable in some cases, namely for megavoltage treatments, as this negates the skin sparing one achieves without bolus present. In such cases, a retracted compensating filter is often used in the place of the bolus in order achieve a contour correction.

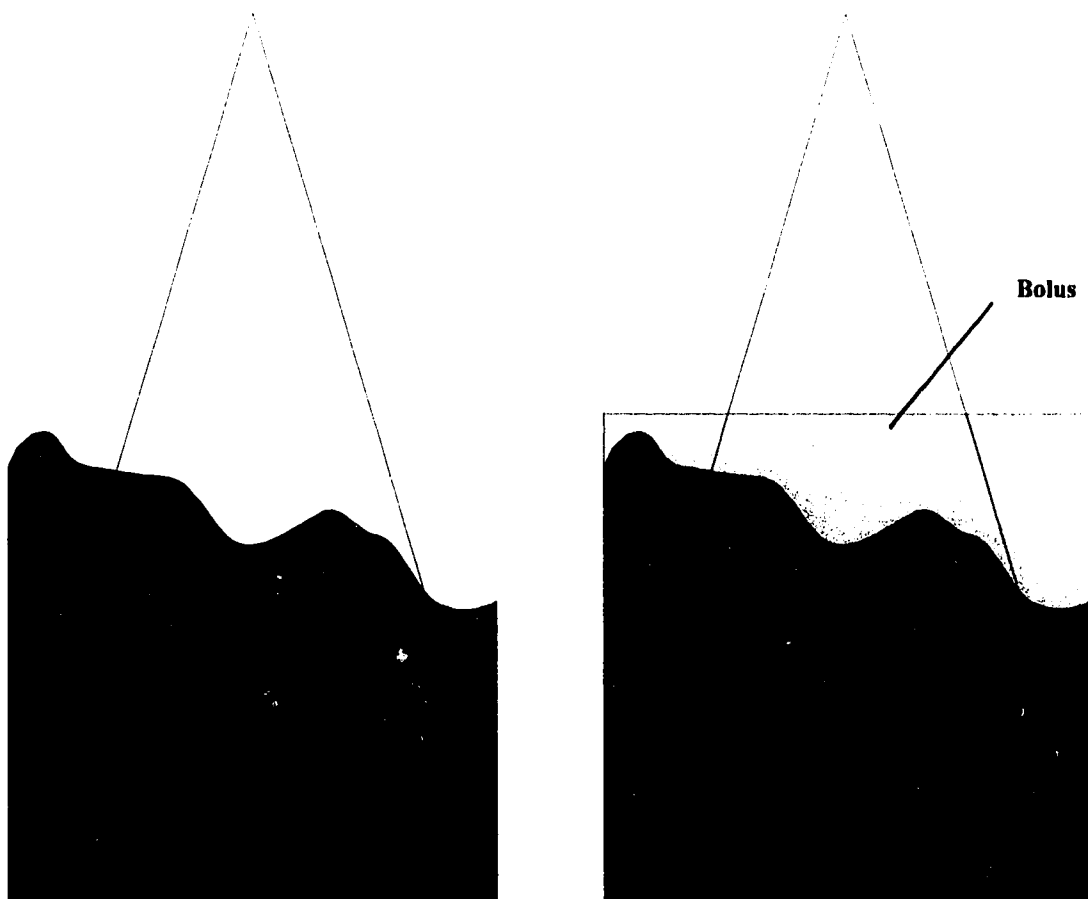


*Figure 1.8 Bolus being used to correct for a non-uniform surface grade on a patient.*

A retracted compensating filter (see figure 1.9) is an irregularly shaped block with a profile varying in one or two dimensions. The thickness as a function of the lateral field co-ordinates ( $x,y$ ) is such that the x-ray beam is attenuated so that the transmitted beam has a relative intensity which is the same as if it had passed through the 'missing' tissue. The thickness of the filter varies much as would compensating bolus thickness along a coincident ray from the source, in order to correct for the variations in patient contour.

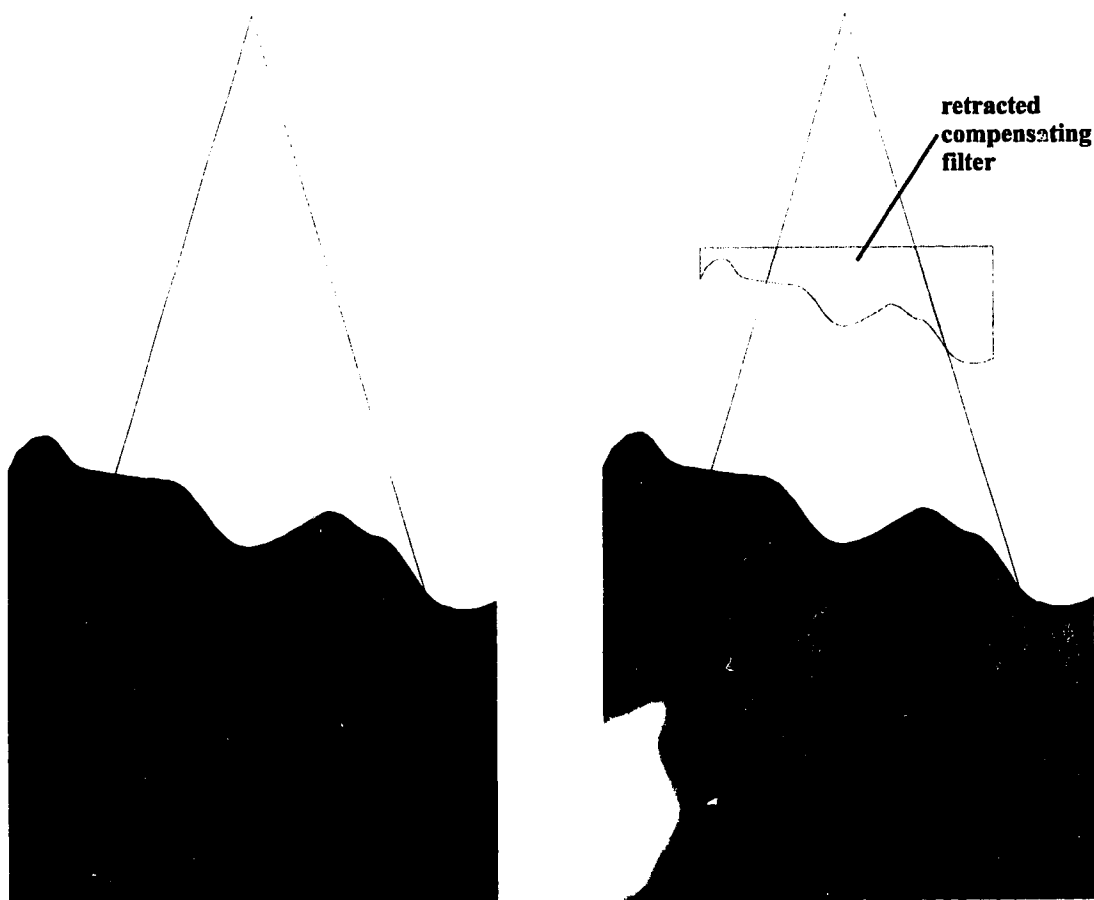


*Figure 1.9 A retracted missing tissue compensator is used to correct for the same non-uniform surface grade as seen in figure 1.8*

#### **1.3.2.4 Dynamic Wedge**

The concept of achieving a desired dose distribution by means of moving the collimator jaws during treatment has, it would seem, existed in one form or another since the late 1940's [Björngard and Kijewski 1976], but it was not until the seminal

paper in the area of dynamic collimation by Kijewski et. al. [Kijewski *et. al.* 1978] that a theoretical model for calculating the jaw position as a function of time to produce a given wedge angle was proposed. It was also around this time that it became possible to exercise the necessary computer control over the machine parameters during treatment, achieving the precision required in timing and positioning. This modality was dubbed the 'dynamic wedge'. The dynamic wedge seeks to replace standard wedges with the dynamic motion of one of the jaws during treatment. Using this technique, one of the collimator jaws of the accelerator is closed during beam delivery in a sweep across the field toward the opposite jaw, until the field is almost closed (see figure 1.10). This produces a monotonically increasing beam profile in the direction of jaw travel, much as one would achieve with a physical wedge. This motion is used to produce an isodose profile whose wedge angle is the same as that of a physical wedge according to the IEC [IEC 1989] and ICRU [ICRU 1976] definition.

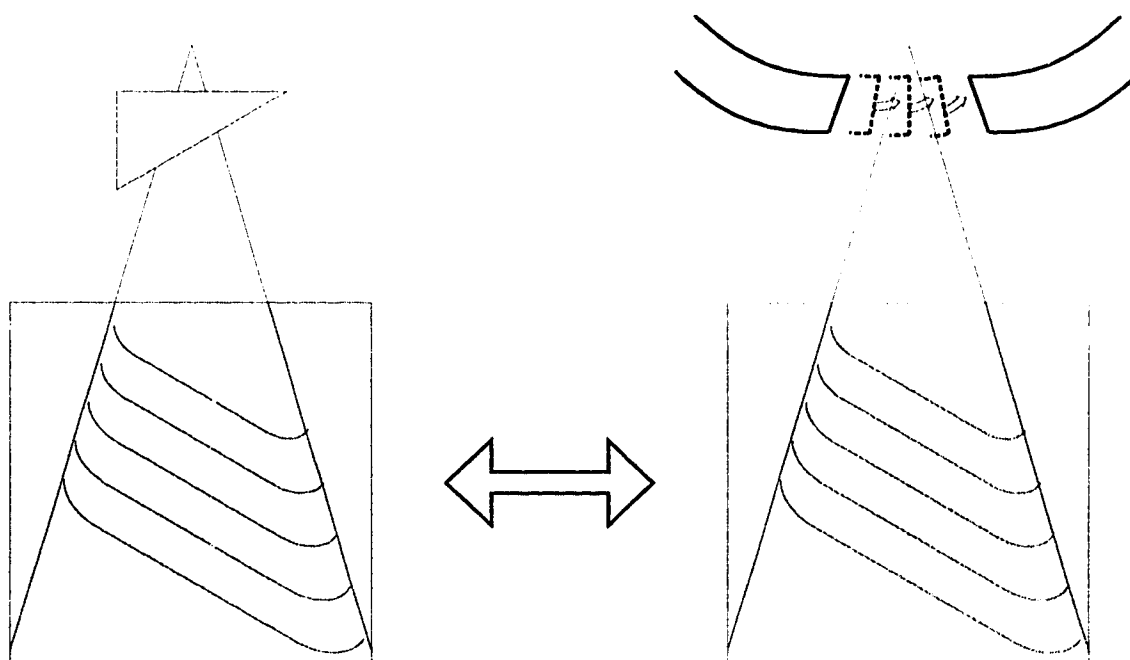


*Figure 1.10 A comparison of field compensation using the standard wedge to field compensation using the dynamic wedge.*

Limited use has already been made of this dynamic collimation technique to reproduce simple wedged fields (the 15, 30, 45 and 60 degree wedges) on Varian C-series linear accelerators. This feature allows replacement of the four standard

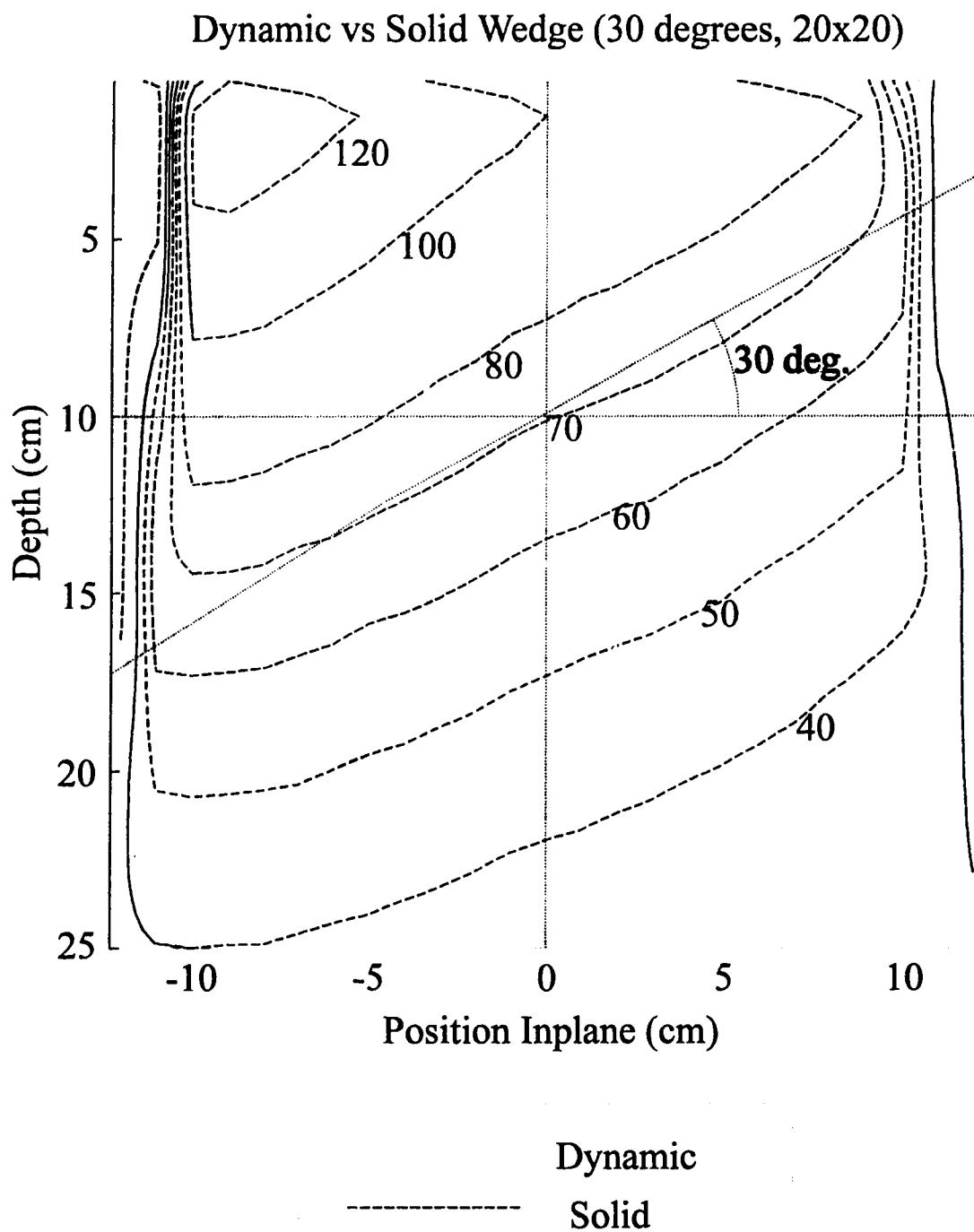


*Figure 1.11 A comparison of standard and dynamic wedge isodoses (measured with ion chamber array, Varian 2300C/D, 6MeV).*



physical wedges with their dynamic counterparts. In the latest version, called enhanced dynamic wedge, angles varying from 10 to 30 degrees (inclusive) in 5 degree increments, as well as 45 and 60 degrees, are available. The benefits of dynamic wedging over physical wedges are well known [Leavitt *et. al.* 1990b; Leavitt 1994b; Huntzinger 1994], namely better adherence to the wedge angle at depth (see figure 1.11), an absence of beam hardening, lower patient surface dose and potentially increased patient throughput since the technician would not have to enter the treatment room for wedge placement. In addition, the beam has spectral characteristics much closer to those of the open field. These same advantages would apply to the use of dynamic compensation over specially fabricated static attenuators, while at the same time saving the time of fabricating a static compensator.

Despite these potential advantages, little has been done to explore the full potential of dynamic collimation, except for this simple case of a monotonically increasing or decreasing dose distribution. Ideally, one would drive both jaws across the field, defining a variable size aperture, to achieve greater control over beam profile shape. This would yield the ability to create profiles having multiple minima and maxima. In order to achieve this, one must have full control over jaw motions, as well as a model which will accurately predict the jaw motions needed to achieve a desired dose profile.

#### **1.4 Development of Dynamic Compensation**

As discussed above, the production of compensated fields can also be realised with a technique known as dynamic compensation. This new modality employs the temporal modulation of collimator jaws or multileaf positions during irradiation to achieve a desired dose or fluence distribution. Although it had been proposed as early as the 1940's [Björngard and Kijewski 1976] that an arbitrary net dose distribution could be achieved by moving the collimating jaws during treatment, it was only with the advent of sufficient computer control over machine parameters during treatment, allowing for precise spatial and temporal positioning of the jaws, that this could be seriously pursued.

Dynamic wedging may be viewed as a subset of the broader class of field compensation strategies known as dynamic compensation. The complexity required for the dynamic wedge technique is greatly reduced by virtue of the fact that it requires the motion of only one jaw. More complex beam profiles can be achieved by exercising computer control over additional machine parameters. A radiotherapy linac has a number of machine parameters that one may wish to control during treatment such as gantry angle, collimator angle, couch height, angle and lateral displacement, as well as the position of all four of the collimating jaws (see figure 1.12).

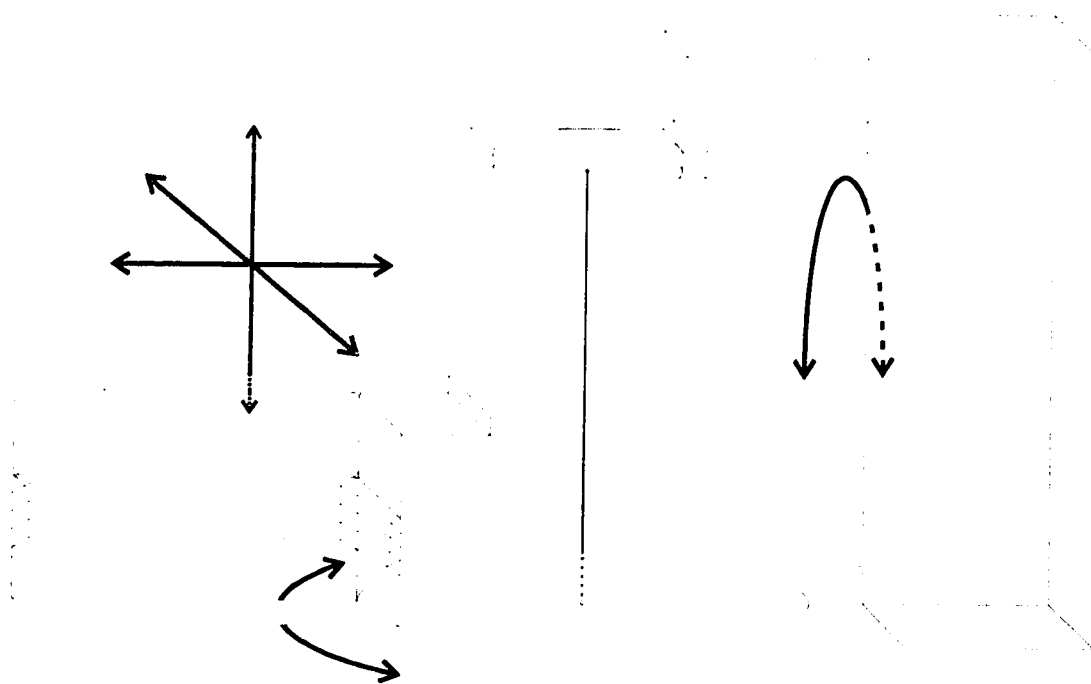


*Figure 1.12 The gross machine parameters (excluding gantry head parameters), including gantry rotation, couch rotation and translation (lateral, horizontal and vertical motion).*

A slightly more complex case than the dynamic wedge would be the motion of two opposing jaws, either in the inplane or crossplane direction (see figure 1.13) during beam on. One should be able to achieve an arbitrary one dimensional dose profile with a single, independent and unidirectional sweep of each of the jaws across the field during beam delivery. The same advantages apply to the use of dynamic compensation as to dynamic wedging compared with specially fabricated static attenuators, while at the same time saving the time of fabricating a static compensator. In order to generate this desired profile, however, it is necessary to know what the jaw positions should be as a function of time or cumulative dose. In order to calculate these position values, one requires a model for the beam delivery process.

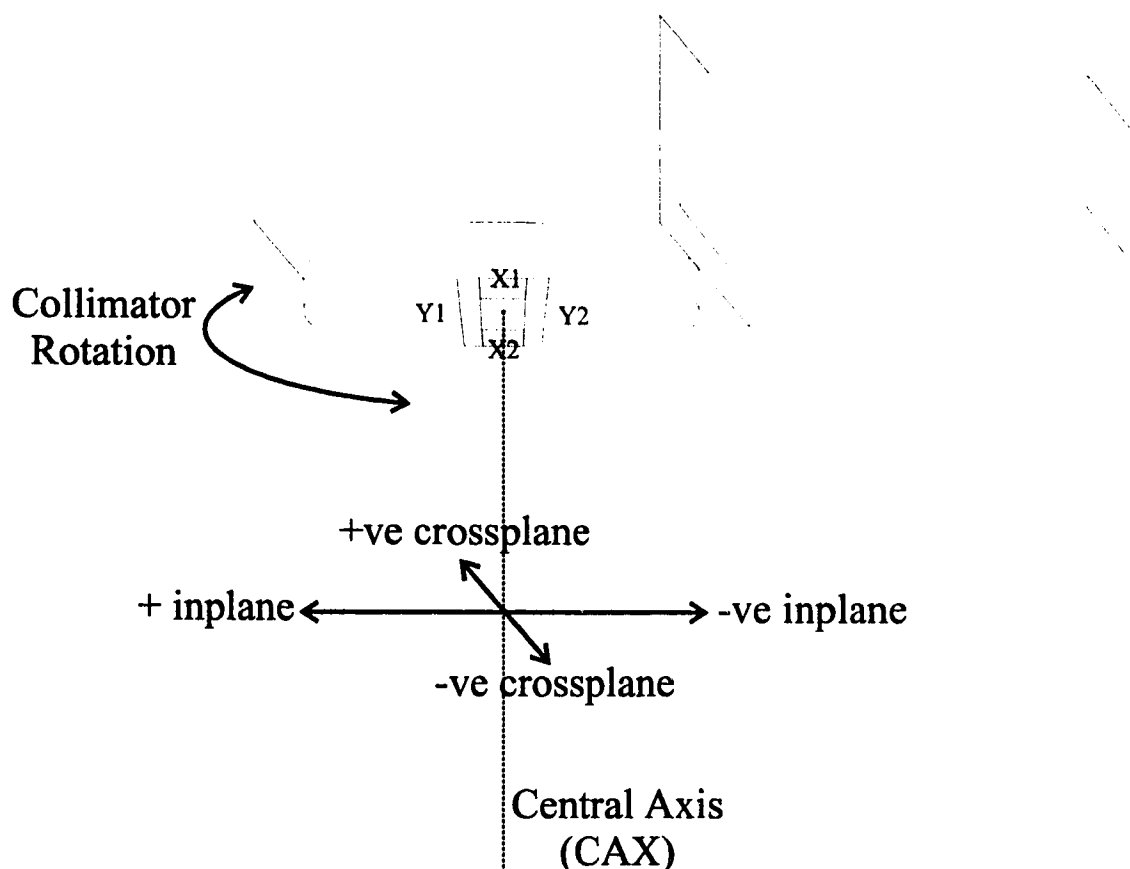


*Figure 1.13 The gantry head parameters, which include collimator rotation, and independent motion of the X and Y collimator jaws in the crossplane and inplane directions respectively.*

A simple example of a dynamic treatment involving the motion of opposing jaws in a unidirectional sweep across a field to modulate an arbitrary one dimensional fluence profile is pictured in figure 1.14. The in-air relative energy fluence profile to be generated is shown at the bottom of the figure; the jaws are moving as a function of time (the number of cumulative monitor units delivered is proportional to time). The requisite jaw motions shown are calculated making a number of simplifying assumptions (no jaw transmission, no head scatter, no variation of field intensity with field size or position, and perfect collimation).

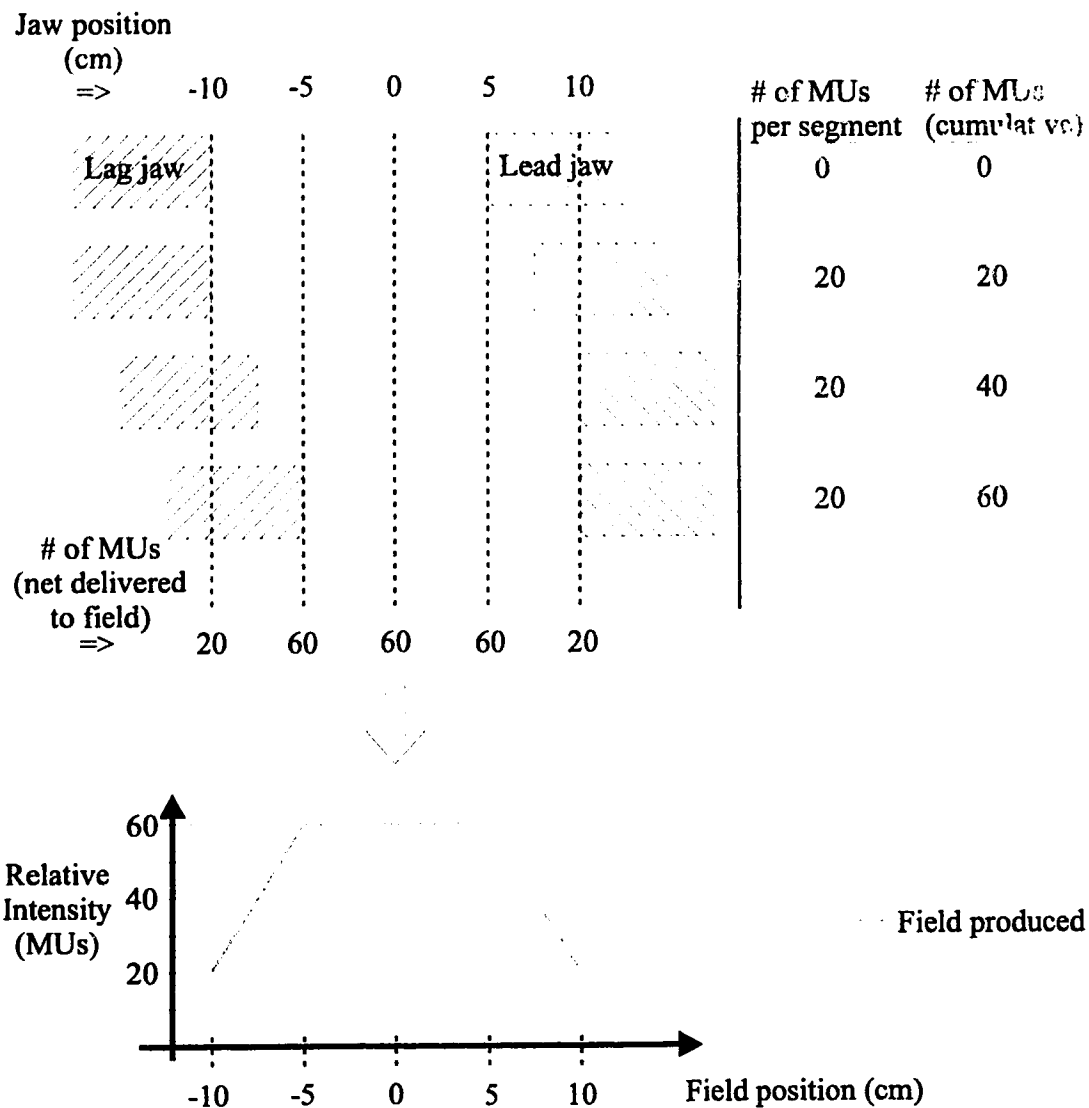


Figure 1.14 A very simple example of a dynamic treatment.

More complex profiles may be realised by defining a greater spatial resolution (i.e. by specifying more points within a given space). Another, slightly more complex example is pictured in figure 1.15.

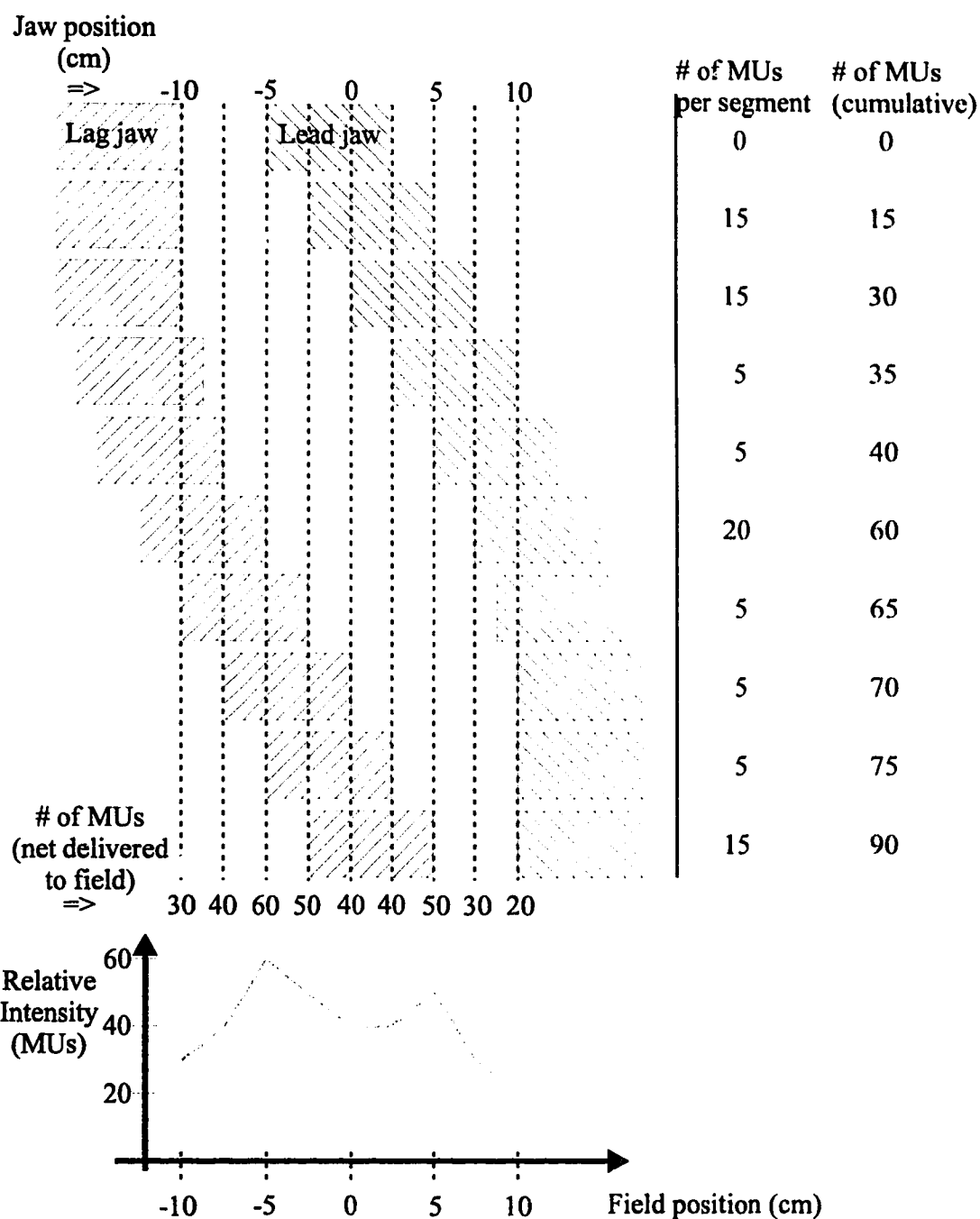


Figure 1.15 A more complex example of a dynamic treatment.

The idea of producing an arbitrary beam profile was addressed for the first time in 1992 [Convery and Rosenbloom 1992]. It was realised then that there were in fact an infinite number of solutions to this problem if one allowed for variable jaw

motions and dose rate. An early attempt to solve this problem employed a Simplex optimisation routine, assuming optimisation with respect to treatment time, and this produced seemingly correct results for the problem. It has been subsequently found that this problem could be solved analytically, also assuming optimisation with respect to treatment time.

It can also be shown [Svensson *et. al.* 1994; Spirou and Chui 1994; section 3.2.3] that the optimal solution for the problem of dynamic collimation for two opposing jaws is found when one of the jaws moves at maximum velocity. This more general theoretical solution was first proposed by Svensson, Källman and Brahme [Svensson *et. al.* 1994] but was not implemented. As well, several practical factors were ignored, such as collimator scatter, penumbral effects, and variation in accelerator output with field position and size.

Accounting for the practical factors mentioned above, as well as the experimental production and verification of dynamic fields, has been the focus of this work. In this work, two different techniques for the calculation of the basic jaw motions required for dynamic fields are tested: initially a numerical optimisation technique, then an analytic solution (given with a new proof that the optimal treatment time is found with this technique). As well, the utility of correcting for various practical factors in the production of dynamic fields is investigated.

## *Chapter 2*

### **Basics of Radiotherapy and Radiation Physics**

#### **2.1 Definitions of Basic Radiation Units**

In order to quantify any beam of radiation, one must first define a number of terms which describe its energy spectrum and intensity. One may define a quantity called the fluence as the expectation value of the number of particles ( $N_e$ ) across a given area ( $A$ ),

$$\Phi = \frac{d}{dA} N_e \quad [2.1]$$

which normally has units of  $m^{-2}$ . In order to describe how the fluence may vary with time, one may further define a quantity called the fluence rate, or flux density

$$\phi = \frac{d}{dt} \Phi \quad [2.2]$$

and this is usually is given units of  $m^{-2}s^{-1}$ . The energy carried by the field across some small area may be described in terms of an energy fluence

$$\Psi = \frac{d}{dA} E \quad [2.3]$$

The flux of energy across a given area over some period of time is the energy fluence rate

$$\psi = \frac{d}{dt} \Psi \quad [2.4]$$

For a polyenergetic beam, one must integrate over the energy spectrum as well as time in order to obtain the total energy carried by the field.

Historically, one of the earliest means of defining the energy of a beam of photons was its ability to ionise a given quantity of air. This quantity, called exposure, is defined as

$$X = \frac{dQ}{dm} \quad [2.5]$$

$dQ$  is the total charge produced by electrons that are set in motion by photons in a mass  $dm$  of dry air, from the time they are set in motion until they are stopped. Exposure is measured in C/kg (SI units) or in Roentgens, which is the historical unit of exposure, where  $1 \text{ R} = 2.58 \times 10^{-4} \text{ C/kg}$ . Exposure does not, according to the International Commission on Radiation Units and Measurements (ICRU) definition, include ionisation arising from bremsstrahlung.

A quantity which is closely related to radiation dose is kerma, which stands for Kinetic Energy Released per unit Mass, and so is reasonably defined as

$$K = \frac{dE_{tr}}{dm} \quad [2.6]$$

This quantity differs from dose (energy absorbed per unit mass), since the energy released at any given point in a medium may not remain at that point. For example, the energy may be transferred to an electron via a Compton interaction, and that electron may travel some distance before depositing its kinetic energy in the medium via numerous Coulomb interactions.

Radiation dose,  $D$ , is given in units of energy per unit mass, and is defined as

$$D = \frac{dE_{dep}}{dm} \quad [2.7]$$

This differs from kerma in that it is the energy absorbed at a point in a medium from charged particles, either directly or indirectly ionised by the radiation, and is measured in SI units of Gray (J/Kg). Historically, dose was measured in rads (100 ergs/g) -- this is the reason for the continued widespread use of cGy. In order to give an idea as to scale in terms of radiobiological effects (RBE), typical treatments give somewhere in the neighbourhood of 50 to 80 Gy in 2 Gy daily fractions, whereas a single whole body dose in the region of 5 Gy is usually fatal.

## 2.2 Radiation Interactions

### 2.2.1 Ionising Radiation Fields

Ionising radiation can be defined as any radiation with energy in the 4 eV to 25 eV and over range, as this is enough energy to eject the most loosely bound electrons from an atom's valence shell. Electrons so liberated will in general have



some fraction of the energy imparted to them left over as kinetic energy. This energy will be transferred to atoms in the vicinity by numerous Coulomb interactions. Photons are referred to as indirectly ionising radiation, as they impart their energy to media in relatively few large interactions. The electrons they set in motion interact with many other atoms, depositing a certain amount of energy per unit mass (i.e. dose). These electrons are referred to as directly ionising radiation.

### 2.2.2 Photon Interactions in Matter

As photons pass through matter, they may undergo a number of interactions. There are basically five major interactions of radiation with matter: photoelectric effect, Compton interaction, pair production, Rayleigh scattering, and photonuclear interactions (see figure 2.1). For each of these effects, one can say that, if an incident beam of intensity  $I_0$  particles is incident on  $N$  nuclei per unit area (most often measured in barns, in the case of cross-sections; 1 barn =  $10^{-24}$  cm<sup>2</sup>), with a transmission of particles  $I_{trans}$ , then the total interaction cross-section is defined as

$$\sigma = \frac{I_{trans}}{(I_0)(N)} \quad [2.8]$$

The combined interaction cross section for all the pertinent effects is the sum of the individual interaction cross sections for each of the photoelectric ( $\tau$ ), Compton ( $\sigma$ ), pair production ( $\kappa$ ), Rayleigh ( $\sigma_{coh}$ ), and photonuclear ( $\sigma_{p.n.}$ ) interactions; so

$$\mu = \sigma_{total} = \sigma + \sigma_{coh} + \sigma_{p.n.} + \tau + \kappa \quad [2.9]$$

This term  $\mu$  is the linear attenuation coefficient. Another important term, called the mass attenuation coefficient ( $\mu/\rho$ ), has units of cm<sup>2</sup>/g and describes the linear attenuation apart from the influence of density. From [2.9], the fractional loss of fluence across a distance  $dx$  is

$$\frac{dI}{I} = -\mu dx \quad [2.10]$$

In other words, the transmitted intensity through a length of material  $L$  is

$$I = I_0 e^{-\mu \cdot L} \quad [2.11]$$

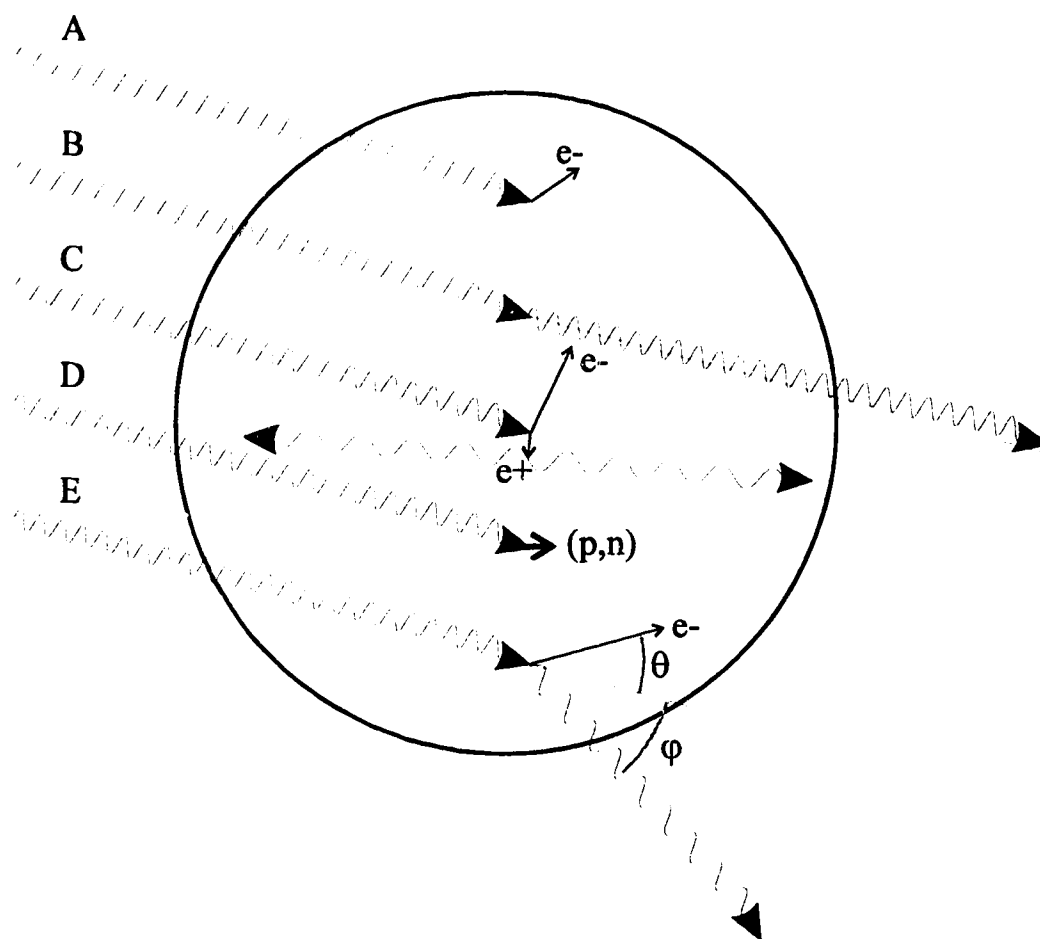


*Figure 2.1 Various possible reactions of photons in matter. Represented here are the photoelectric effect (A), Rayleigh scattering (B), pair production (C;  $e^+$  -  $e^-$  production, in this case, with the  $e^+$  undergoing an annihilation), photonuclear reaction (D) and Compton scattering (E).*

The various interactions mentioned above and depicted in figure 2.1 tend to dominate in different energy domains or, for some, do not contribute appreciably to energy deposition. Roughly, the photoelectric effect dominates at low energies (0-100 keV), the Compton effect dominates at medium energies (100 keV - 5 MeV), and pair production dominates at very high (high for the purposes of radiotherapy, at least) energies (5 MeV+). The photonuclear effect has a very low contribution for radiotherapy energies, and Rayleigh scattering tends to be unimportant for dose deposition.

### 2.2.2.1 Photoelectric Effect

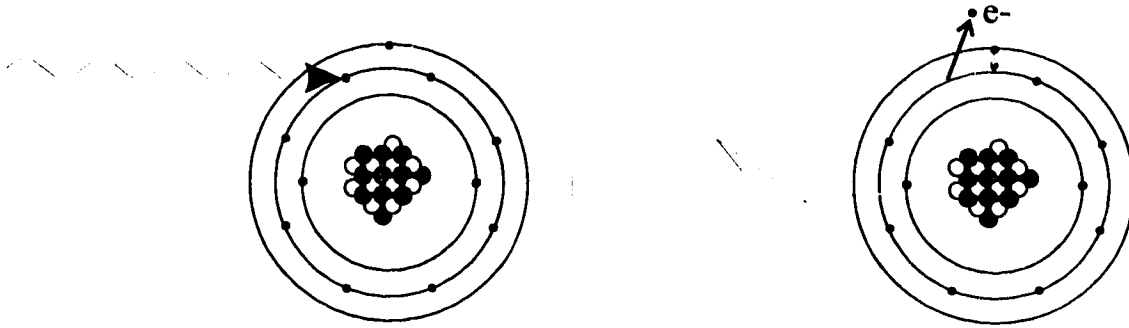


Figure 2.2 The photoelectric effect.

The photoelectric effect (see figure 2.2) is the name given to the interaction in which a photon is absorbed by an atom and an orbital electron, known as a photoelectron, is ejected. These photoelectrons have an energy of

$$T_{e^-} = h\nu - E_b - T_{\text{atom}} \quad [2.12]$$

where  $T_{e^-}$  is the kinetic energy of the ejected electron,  $h\nu$  is the energy of the incident photon,  $E_b$  is the binding energy of the electron, and  $T_a$  is the kinetic energy given to the atom (this is almost zero). The  $E_b$  term varies depending on the energy of the electron, based on what shell it is in. The mass attenuation cross section for this effect is approximately [Attix 1986]

$$\frac{\tau}{\rho} \propto \left( \frac{Z}{h\nu} \right)^3 \quad [2.13]$$

The interaction cross section for the photoelectric effect is really the sum of the cross section values for the different shells (i.e.  $\tau = \tau_K + \tau_L + \tau_M + \dots$ ).

### 2.2.2.2 Compton Effect

The Compton effect (see figure 2.3), named after Sir Arthur Holly Compton, who first described it, involves the scattering of a photon from an electron, deflecting the photon and setting the electron into motion. The electron is assumed to be a “free” electron -- both unbound and stationary. This is an acceptable assumption as the photon energies are relatively large compared to the electron binding energies.

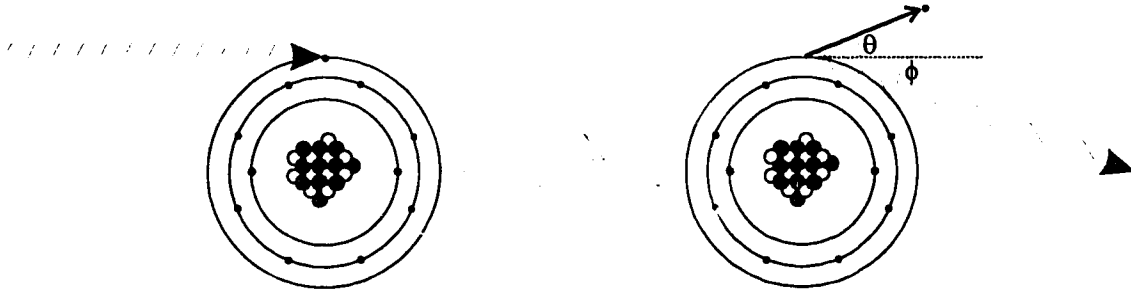


Figure 2.3 The Compton effect.

The relationship of the incident photon energy, kinetic energy of the electron, and angles of scattering are well known. A fraction of the energy of the photon is transferred to the electron, which in turn transfers its energy via Coulomb interactions to other atoms in its path. The kinetic energy of the electron thus set in motion is

$$T = h\nu - h\nu' \quad [2.14]$$

The energy of the scattered photon,  $h\nu'$ , the angle  $\theta$  through which the electron is scattered, are found in numerous texts [e.g. Attix 1986].

The mass attenuation cross section for Compton scattering is

$$\frac{\sigma}{\rho} = \frac{N_A Z}{A} \sigma_c \quad [2.15]$$

where  $N_A$  is Avogadro's number,  $Z$  is the number of electrons per atom,  $A$  is the atomic mass, and  $\sigma_c$  is the cross section per electron [Attix 1986].

### 2.2.2.3 Pair Production

Provided a photon is of sufficient energy (e.g., greater than 1.022 MeV for electron-positron creation), it may interact with the electromagnetic field of a nucleus to form a particle/antiparticle pair (the electron/positron pair is the most common at lower energies). The particles created will have rest mass and kinetic energy dictated by

$$h\nu_0 = T^+ + T^- + m_p c^2 + m_p c^2 \quad [2.16]$$

The mass attenuation cross section for this effect is [Attix 1986]

$$\frac{\kappa}{\rho} = \frac{r_0^2}{137} Z^2 \bar{P} \frac{N_A}{A} \quad [2.17]$$

where  $r_0$  is the classical electron radius,  $Z$  is the electron/proton number,  $N_A$  is Avogadro's number,  $A$  is the atomic mass, and  $\bar{P}$  is slowly function of photon energy and  $Z$ .

#### 2.2.2.4 Rayleigh Scattering

Rayleigh scattering is the scattering of a photon by an atom without imparting energy to liberate an electron, and with the whole atom recoiling only very slightly to conserve momentum. Rayleigh scattering is also called coherent scattering since the collision is elastic; this, of course, implies no kinetic energy is transferred to the atom, and hence Rayleigh scattering does not contribute to dose deposition. The angle of scattering is energy and  $Z$  dependent -- for lead, the scattering angle is about  $30^\circ$  for 0.1 MeV,  $4^\circ$  for 1 MeV and about  $1^\circ$  for 10 MeV. The mass attenuation cross section for this effect is roughly [Attix 1986]

$$\frac{\sigma_R}{\rho} \propto \frac{Z}{(h\nu)^2} \quad [2.18]$$

#### 2.2.2.5 Photonuclear Interactions

The photonuclear effect is a direct interaction of the photon with the atomic nucleus which results in the ejection of a neutron or a proton. For this interaction to take place an incident photon must be of sufficient energy (about 5 to 15 MeV), since the nucleon set in motion must overcome the nuclear binding energy. This effect only contributes, relatively speaking, about 5% of the kerma that pair production does [Attix 1986] at these high energies, and so is of relatively negligible importance.

### 2.2.3 Dose Deposition

The deposition of dose in a given volume element is ultimately the result of the transfer of energy from the radiation field to the medium. The transfer of energy from x-ray photons to a medium results when these photons set charged particles (electron, proton, alpha particle, ...) in motion through various interactions (cf. 2.2.2). Deposition of energy is a two step process, with the photons giving rise to energetic particles, which in turn impart energy to the medium or to other particles via multiple Coulomb events.

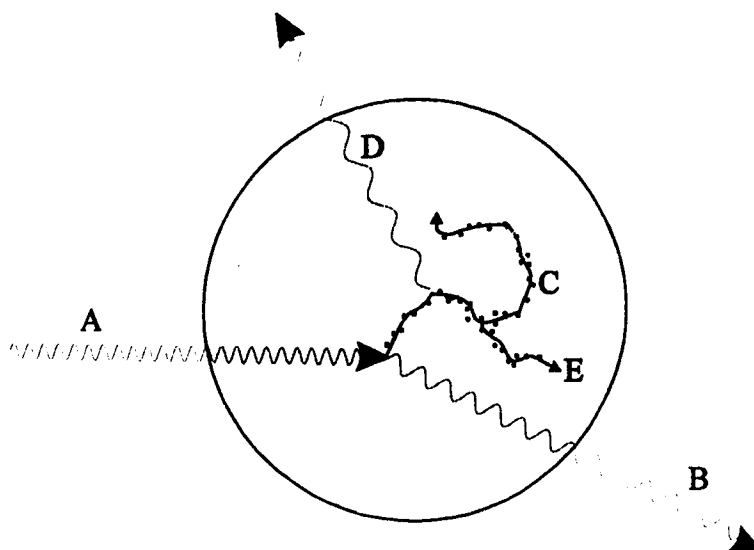


*Figure 2.4 Dose deposition in matter. Track A is the incoming photon, B is a scattered photon, C is the energetic charged particle set in motion, D is a photon from a radiative interaction, and E is a delta ray (an electron set in motion from a direct  $e^- - e^-$  collision event).*

### 2.2.3.1 Radiative and Collision Events

The energy released by a charged particle in a medium comes from two sources: collisional energy losses by the particle and radiative energy losses. The collisional losses are chiefly due to Coulomb scattering from atomic electrons, the so called 'soft' collisions, or from direct 'knock on'  $e^- - e^-$  collisions. If the charged particles are electrons, the scattering angle for electron-electron interactions and elastic scattering with the nucleus can be quite large, hence the erratic nature of the electron tracks [Krane 1988]. The radiative losses arise from the energy released when the electrons undergo sudden accelerations in the Coulomb field; this radiation, due to acceleration of the particle, is called bremsstrahlung radiation.

At distances which are considerably greater than the atomic radius, charged particles interact with the atomic electrons via small Coulomb interactions. These 'soft' collision interactions are the most prevalent of the charged particle interactions. They may account for up to half of the energy transferred to the medium [Attix 1986].

At distances on the order of the atomic nucleus, direct collisions occur which result in energetic free electrons; these electrons are known as delta rays or secondary electrons. A delta ray will give rise to a second charged particle track along which energy will be deposited independently of the primary electron. The total energy

transferred by these direct collisions is comparable to the energy transferred by the 'soft' collisions, but the energy transferred per collision is greater and there are fewer of these direct 'knock on' interactions.

For distances smaller than the atomic radius, one has mostly elastic collisions which have a differential cross section of

$$\frac{d\sigma}{d\Omega} \propto Z^2 \quad [2.19]$$

In a very few cases, on the order of 2 - 3 % [Attix 1986], there will be an inelastic collision. A significant portion of the electron's energy, sometimes all of it, may be given up as a radiative loss from this sudden acceleration in the Coulomb field of the nucleus.

Radiative losses are negligible for nonrelativistic particles, but become appreciable for high velocity particles. The ratio of radiative to collisional losses along some small distance is [Krane 1988]

$$\frac{(E)_r}{(E)_c} \approx \frac{T + mc^2}{mc^2} \frac{Z}{1600} \quad [2.20]$$

This relation may be used to give the relative weighting of the collisional and radiative events for various electron energies and various materials with differing Z values.

### 2.2.3.2 Stopping Powers

As has been said, the collisional and radiative energy losses account for the energy imparted to the medium. Examining the change in energy of the charged particle along some small distance  $dx$  of its path resulting from these two main energy loss mechanisms, one has

$$\frac{dE}{dx} = \left( \frac{dE}{dx} \right)_c + \left( \frac{dE}{dx} \right)_r \quad [2.21]$$

This quantity, the amount of energy imparted to the medium by a charged particle, is known as the stopping power. This is given in most general terms as  $\left( \frac{dE}{dx} \right)_{E,P,Z}$  which is to say that the amount of energy lost by a charged particle along its track is a function of energy  $E$ , particle type  $P$  and atomic number  $Z$  of the material it is moving

through. In more specific terms, one often talks in terms of mass collision stopping powers  $\left( \frac{dE}{\rho dx} \right)$  where  $\rho$  is the density of the medium in question. One may speak of the mass collision stopping power and the mass radiative stopping power, as per [2.21]. The mass collision stopping power may be further subdivided into the mass collision stopping powers for the soft and hard terms. One may also talk about the restricted mass collision stopping power, a term which ignores delta rays with energy greater than a certain value -- this allows the computation of the dose in a thin foil as energy is being carried out of the volume of interest by delta rays of greater than a certain cut-off energy, and not being replaced by other incoming delta rays. The restricted mass collision stopping power is also related to a very important concept, namely that of the linear energy transfer (LET), which is the same as the restricted mass collision stopping power without the mass dependency; it gives the kinetic energy transferred per unit length of the charged particle's track and it is related to the relative biological effectiveness of the radiation in question.

### 2.2.3.3 Charged Particle Equilibrium

If there exists the condition of charged particle equilibrium then for every charged particle that leaves a volume of interest, another one of the same type and with the same energy expectation value enters (see figure 2.5). This means that even

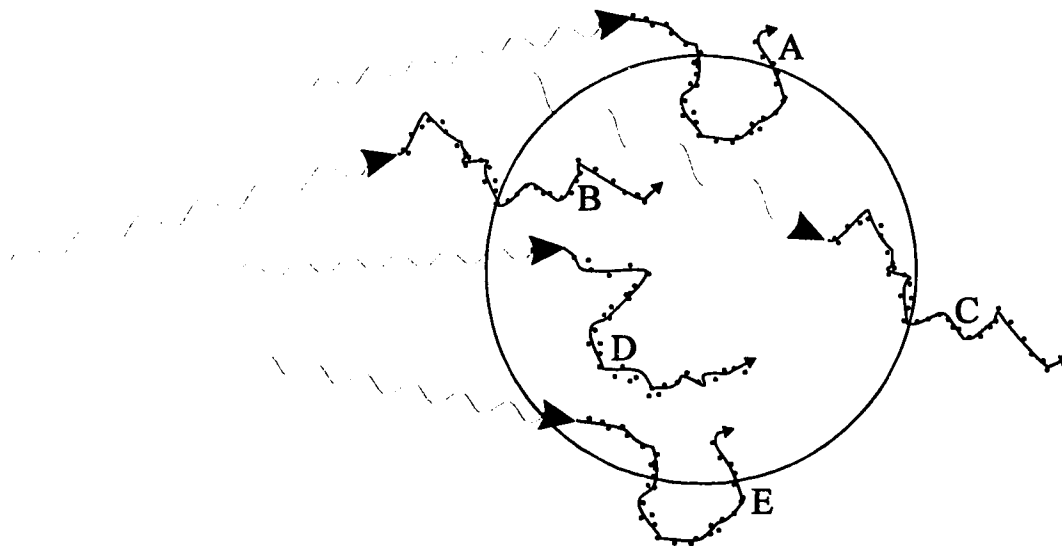


*Figure 2.5 Charged particle tracks. For the pairs A and E, and B and C, the portion of one track which lies outside of the region of interest is balanced by the other track which has a analogous track which lies inside the region (so A and E, for example, would combine to effectively give one track completely inside the region of interest).*



though the energy imparted to some particles in a volume of interest may be deposited outside that volume by these particles, it is likely that for every one of these particles that deposit some of its dose outside that volume, another particle which was set in motion outside the volume of interest will deposit an equal amount of energy inside the volume.

### 2.2.3.4 Kerma and Dose

As has already been noted, the transfer of kinetic energy to a particle in a medium (kerma) is not the same as dose deposition. The energetic particles may, after acquiring kinetic energy, move along a path giving up this energy through many small Coulomb interactions. The path will terminate when the particle comes to rest, and this may occur some distance from where it was initially set in motion. Consequently, it may be that much of the energy the particle received is deposited outside the volume of interest. The energy released may also be radiated as a photon, which again may leave the volume of interest before imparting any or all of its energy.

Recalling [2.6], which defines kerma as the energy transferred to the medium, we can further refine this as

$$K = K_c + K_r \quad [2.22]$$

which is to say that kerma has two components: a collision component ( $K_c$ ) and a radiative term ( $K_r$ ).

At the lower range of energies of particles (almost entirely electrons) which are set in motion in a given medium, energy is transferred to the medium via numerous collision interactions (very little is re-radiated at lower energies). The collision kerma is related the fluence (cf. [2.4])

$$K_c = \left( \frac{\bar{\mu}_{en}}{\rho} \right)_{E,Z} \psi \quad [2.23]$$

where  $\left( \frac{\bar{\mu}_{en}}{\rho} \right)_{E,Z}$  is the mass-energy absorption coefficient (which is a function of energy  $E$  and atomic number  $Z$ ). Where electronic equilibrium exists one may equate dose to kerma, so

$$D = K_c = \left( \frac{\bar{\mu}_{en}}{\rho} \right)_{E,Z} \psi \quad [2.24]$$

Alternatively, and more generally (making no assumptions regarding CPE), one can say that the dose which is deposited by energetic electrons set in motion by photons is given by

$$D = \Phi_{e^-} \left( \frac{1}{\rho} \frac{dT}{dx} \right)_C \quad [2.25]$$

which is the particle fluence times the mass collision stopping power ( $dT$ , change in kinetic energy, over a small distance  $dx$  due to collisions). If one integrates this expression over all kinetic energies,  $T=0$  to  $T=T_{\max}$ , and divides by the integral over the spectrum of energies, then one obtains a value which is called the average mass collision stopping power

$$\left( \frac{\bar{S}}{\rho} \right)_{C,M} = \frac{\int_0^{T_{\max}} \Phi_{e^-}(T) \left( \frac{1}{\rho} \frac{dT}{dx} \right)_{C,M} dT}{\int_0^{T_{\max}} \Phi_{e^-}(T) dT} = \frac{D_{C,M}}{\Phi_{e^-}} \quad [2.26]$$

which can be used to calculate the dose in a cavity (C) or medium (M). This relation is used in conjunction with cavity theory [Johns and Cunningham 1983].

### 2.3 Beam Production

The goal of radiation therapy is to deliver a tumouricidal dose to a treatment volume, while sparing as much of the surrounding tissue as possible. In order to deliver such a dose from an external source, a sufficient dose rate is required such that the dose can be delivered in a reasonable amount of time. As well, having a beam that is also of high energy is desirable, since higher energy beams have the effect of 'skin sparing' (the surface dose is not the maximum dose; the depth of maximum dose is on the order of centimetres for megavoltage treatments). This is particularly beneficial for more deeply seated tumours.

A number of devices can be used to produce a radiation beam. A cobalt-60 therapy unit which uses a small cylinder of activated cobalt as a radiation source (e.g. the Theratron 780<sup>1</sup>) may be employed for the production of a beam of photons. A number of accelerating devices are available which can produce either a beam of photons or electrons, such as the microtron, the betatron, or the linear accelerator, the x-rays being produced by bremsstrahlung in each of these by accelerating electrons to impinge on some high  $Z$  target. Cyclotrons have been used for proton therapy, and for the production of negative pions as well.

<sup>1</sup> Theratronics International, Kanata, Ontario

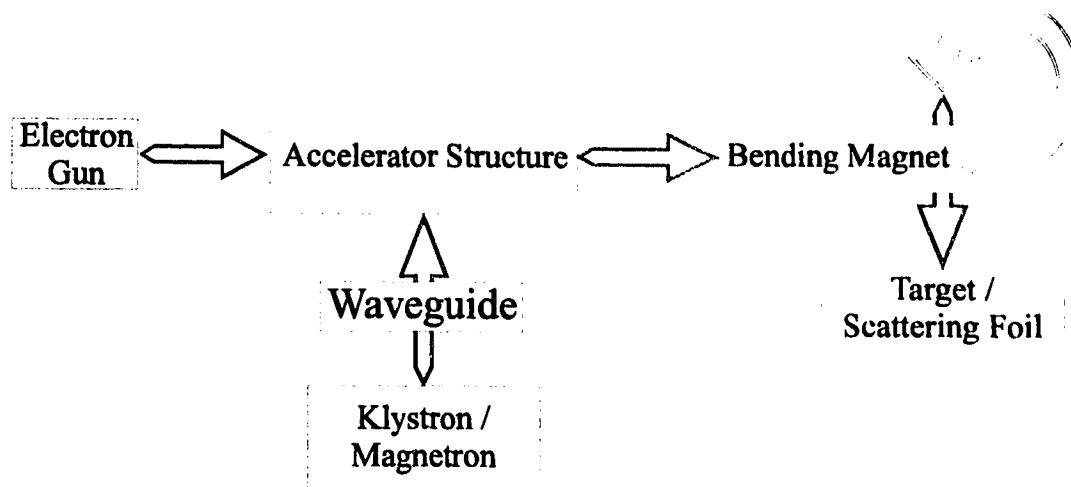


*Figure 2.6 The production of a high energy electron/photon beam in a typical medical linac.*

The most prevalent treatment machine in use today is the medical linear accelerator (see figure 2.6 for a simple schematic). It has the advantage of being able to produce high energy electron and x-ray beams, without being as space intensive as a microtron, provides higher dose rates than are available with a betatron, and yields greater beam energies than possible with a cobalt unit which has an effective beam energy of about 1.25 MeV.

### **2.3.1 Pre-Target Mechanisms**

The production of a beam inside the linear accelerator (see figure 2.6) ultimately begins with the thermionic emission of electrons by an electron gun into an evacuated accelerating structure. The electrons are then bunched in the accelerating structure and accelerated by a microwave electric field. This field is produced by a klystron or magnetron, and directed into the accelerating structure by another waveguide. The electrons are ultimately directed onto either a bremsstrahlung target or an electron scattering foil, giving a clinically usable beam of electrons or photons.

The magnetron is the source of the microwave power for most low energy linacs. It is a high power oscillator which produces microwave pulses on the order of  $\mu\text{s}$  in duration, with a pulse repetition frequency of the order of 1-500 Hz. The klystron, although not a microwave source itself, serves to amplify the microwaves produced by a low power microwave source.

The waveguide serves to deliver the microwaves produced by the magnetron or klystron to the accelerator structure. It is typically of the simple rectangular

waveguide variety, with the dimensions chosen such that the allowed frequencies for the waveguide include the desired value (in the case of medical linacs, in the neighbourhood of 3000 MHz).

The accelerator structure is a cylindrical waveguide whose job it is to accelerate electrons to the appropriate energy (6 MeV, for example). This waveguide is generally one of two kinds: a travelling wave, or standing wave. Most modern linacs are of the standing wave variety. The electric field in the accelerator structure can be described by

$$\vec{E}(x) = \vec{E}_0 e^{i(\omega t - k_n x)} \quad [2.27]$$

where  $x$  is the direction of travel for the electrons in the tube. The electric field in a cylindrical waveguide at some time  $t = n(2\pi)/T$ , where ( $n=1,2,3,\dots$ ) and  $T$  is the period, is depicted in figure 2.7.

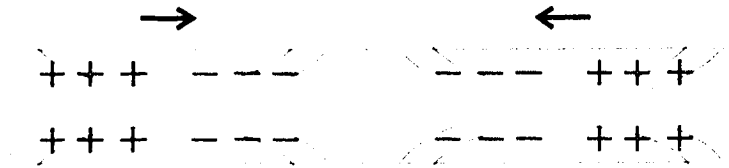


Figure 2.7 The electric field in a cylindrical waveguide

The phase velocity of the electric field as shown in figure 2.7 exceeds that of an electromagnetic wave in free space. The field in the accelerator waveguide is not like this, however, as a number of disks are introduced in order to reduce the phase velocity of the electric field to less than  $c$ . The electric field in the waveguide becomes, as a function of time, as shown in figure 2.8. Electrons may thus be accelerated by the electromagnetic field established in the waveguide as depicted in figure 2.8 with the arrows indicating the direction of the electric field (these would move to the right, every  $(\pi/2)$  cycles).

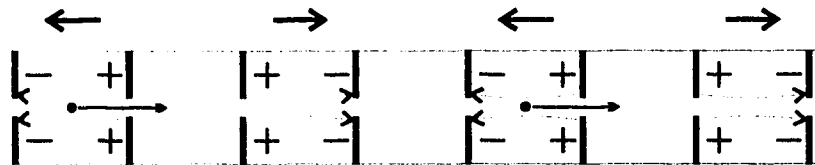
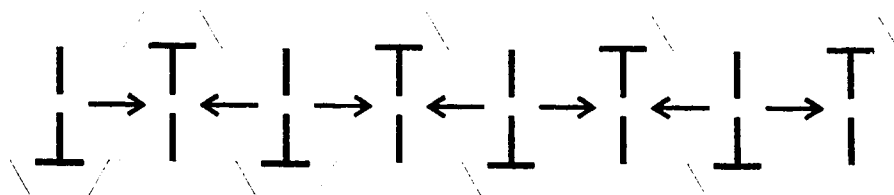


Figure 2.8 The electric field in a cylindrical waveguide with disks

Since space is at a premium for medical linear accelerators, the zero field portions of the waveguide are moved off axis, the so called off axis coupled chambers. So, the final result is that most modern accelerating wave guides look something like figure 2.9



*Figure 2.9 The cylindrical waveguide with off-axis coupled chambers*

A few other generalisations can be made about the accelerating wave guide. It is a cylindrical cavity, standing wave waveguide with off axis coupled chambers. The microwave power supply furnishes the waveguide with a roughly 3000 MHz ( $\lambda=10$  cm) wave. The cavities are about 10 cm in diameter, and 2.5 to 5 cm in length. The initial cavities are nonuniformly spaced in what is known as the buncher (the buncher serves to increase the phase velocity of the electric field, to accommodate the accelerating electron bunches, as well as to concentrate the electrons into discrete groups). The electrons is typically injected with a 1 - 30 kV spectrum [Karzmark 1984].

### **2.3.2 Gantry Head Physics**

The design of the gantry head (see figure 2.10), which is the heavily shielded location of key beam production components, can greatly influence the energy distribution of the treatment beam (either electron or photon) that is ultimately produced. The chief components of the head are the bending magnet (if one is employed), x-ray target (for photon beam), primary collimator, beam flattening filter (for photons), scattering foil (for electrons), the monitor ion chambers, field defining light source and mirror, and the secondary collimators. The magnet, target (if in x-ray mode) and filter or foil have the greatest effect on the character of the beam produced.

The bending magnet for the electron beam directs the beam onto the x ray target. The electrons then impinge on the small focal spot of a target (see figure 2.10), which according to most measurements [Jaffray *et. al.* 1993; Munro *et. al.* 1988; Lutz *et. al.* 1988] is on the order of 2 mm in diameter.

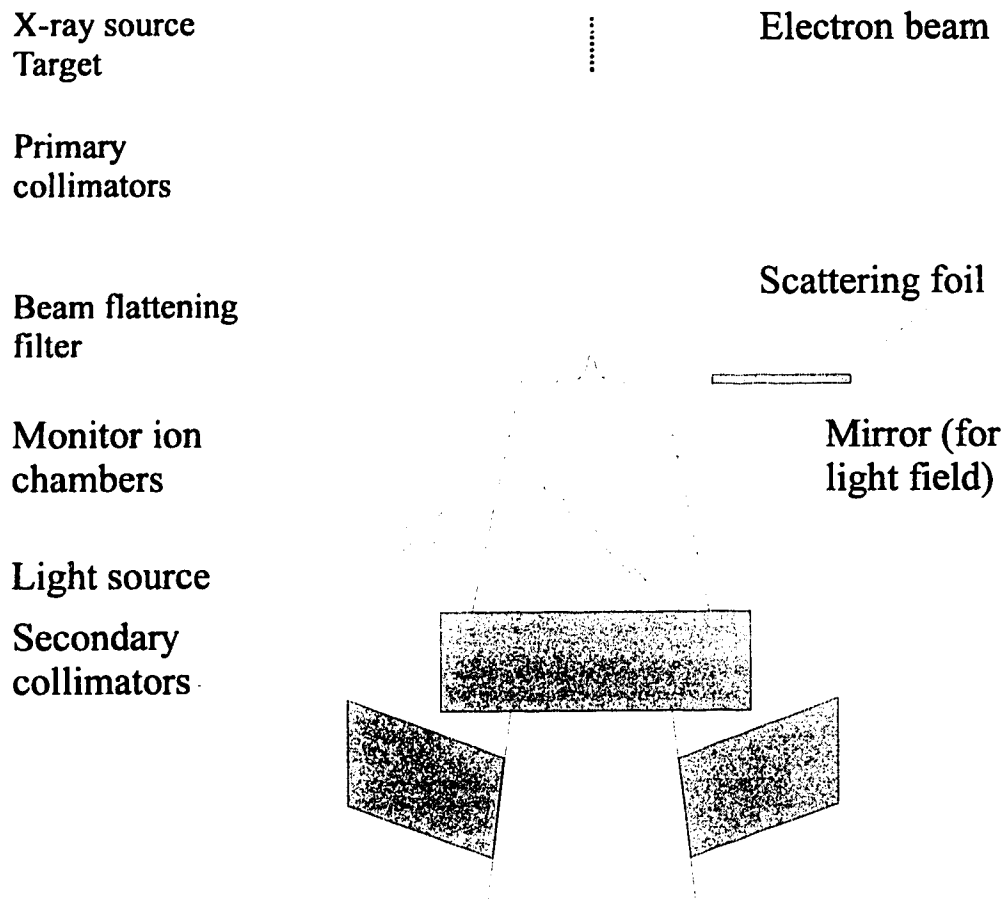


Figure 2.10 Basic gantry head schematic

The electron beam terminates at a high  $Z$  target, usually tungsten or a tungsten alloy. These electrons undergo numerous collisions and scatterings, but at the high energies of megavoltage machines, an appreciable amount of radiation results from changes in acceleration due to scattering (cf. 2.2.3.1); this is called bremsstrahlung, or braking radiation. The efficiency of an x-ray target can, for electrons, be simplified to

$$\text{Eff.} = 9 \times 10^{-10} (Z)(V) \quad [2.28]$$

where  $Z$  is the atomic number for the nucleus, and  $V$  is the acceleration potential in volts. This means, for 6 MeV electrons, that radiative losses account for about 40 % of energy losses in tungsten ( $Z=74$ ), a common x-ray target material.

For this investigation, the electrons in the wave guide are accelerated to 6 MeV and then strike a tungsten alloy target. This produces a photon beam with an energy spectrum from 0 to 6 MeV (called a 6 MV beam) -- this spectrum can be

approximately calculated using a thin slab bremsstrahlung approximation and has an angular distribution of intensity as described by the Sommerfeld equation [Panofsky and Philips 1962]

$$I = (\text{const.}) \frac{\sin^2 \theta}{\left(1 - \frac{v}{c} \cos \theta\right)^5} \quad [2.29]$$

The character of the primary beam is not considered clinically ideal in its initial form, either for electron treatments or for x-ray mode. The desired output from the linac is a 'flat' beam over some given field size -- a beam with a roughly homogeneous energy fluence distribution over the whole field normal to the direction of the initial (pre-target) electron beam. Different beam modifying devices may be employed to achieve the desired radiation distribution, depending on the radiation type: a conical beam flattening filter for x-rays, and a thin flat scattering foil for electrons.

The beam produced by the target does not have the desired characteristics for a treatment beam, namely flat isodose contours in a phantom normal to the treatment beam. Instead the beam intensity is forward peaked as per [2.29]. In order to achieve a beam which has a roughly flat profile in phantom, a beam flattening filter is introduced into the beam. This filter is a bicomposite material of proprietary design, but it must clearly be conical in shape, thereby creating more attenuation at the centre as compared to the edges of the filter. The flattening filter can attenuate 50 to 90 % of the central axis (CAX) photon intensity [Karzmark 1984].

The photon energy fluence upstream from the secondary collimating jaws but below and distal to the flattening filter is relatively flat, but has a definite rise at points away from the CAX, with a variation upwards of 7-9% at the extreme field edges (see figure 2.11). This is by design so as to give a flat dose profile in phantom around 10 cm depth. The rise is to account for beam divergence, the difference in attenuating path length, and scatter away from the CAX.

There is a set of four main monitor ion chambers inside the gantry head, along with backup chambers. These ion chambers register collected charge as arbitrary 'monitor units' (MUs). The machine output is often calibrated such that one monitor unit is equal to the energy fluence required to give 1 cGy of dose to a point at the centre of a 10 by 10 cm field, at 1.5 cm depth in a water phantom for a 6 MV beam and at 100 cm SDD (source to detector distance). This sort of calibration allows an easy determination of absolute dose for most cases.

The megavoltage x-ray beam is collimated with a set of four collimating blocks, two opposing pairs in the inplane and crossplane direction respectively. A

typical collimator may be approximately 7.8 cm thick (for the Varian 2300CD), and are made of a high Z material (e.g. lead, tungsten, or some alloy); this yields, assuming lead blocks (approximately  $\mu/\rho=0.045 \text{ cm}^2/\text{g}$  for 2 MeV;  $\mu=0.51 \text{ cm}^{-1}$ ), an attenuation of

$$I = I_0 e^{-\mu \cdot L} = 100(e^{-(0.51 \text{ cm}^{-1})(7.8 \text{ cm})}) = I_0(0.019) \quad [2.30]$$

or about 2 % transmission.

The radiation field produced below the secondary collimators can be measured with various dosimeters: film, ion chamber, ion chamber array, and diodes. By measuring for the largest possible field size, one may observe what the field is presumably like just below the beam flattening filter (see figure 2.11). The energy fluence follows a roughly linear rise in the region from about 3 cm out from the CAX to the field edge except in the penumbral region, as measured perpendicular to the CAX at 100 cm from the source. The field characteristics in the penumbral region are discussed further in 3.3.3.

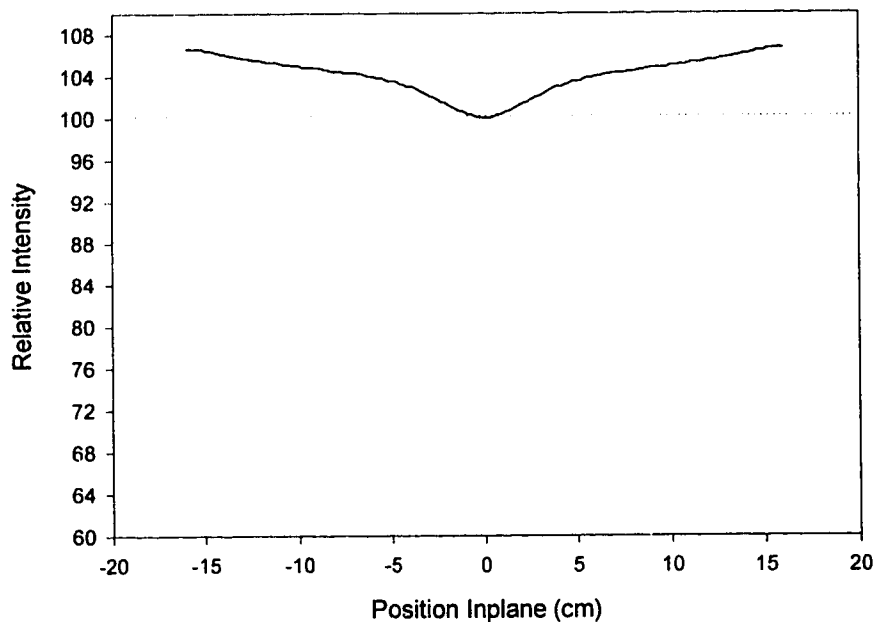


*Figure 2.11 Relative energy fluence in air, measured with an ion chamber (Varian 2300C/D, 6 MV, 100 SDD).*



## 2.4 Beam Measurements

### 2.4.1 General Beam Descriptors

There are a number of quantities that are used with respect to teletherapy radiation beams to characterise them. These are usually determined from measurements made in phantom. Empirical relations can then be used in the determination of various quantities such as dose distributions for patient treatments.

#### 2.4.1.1 Percent Depth Dose

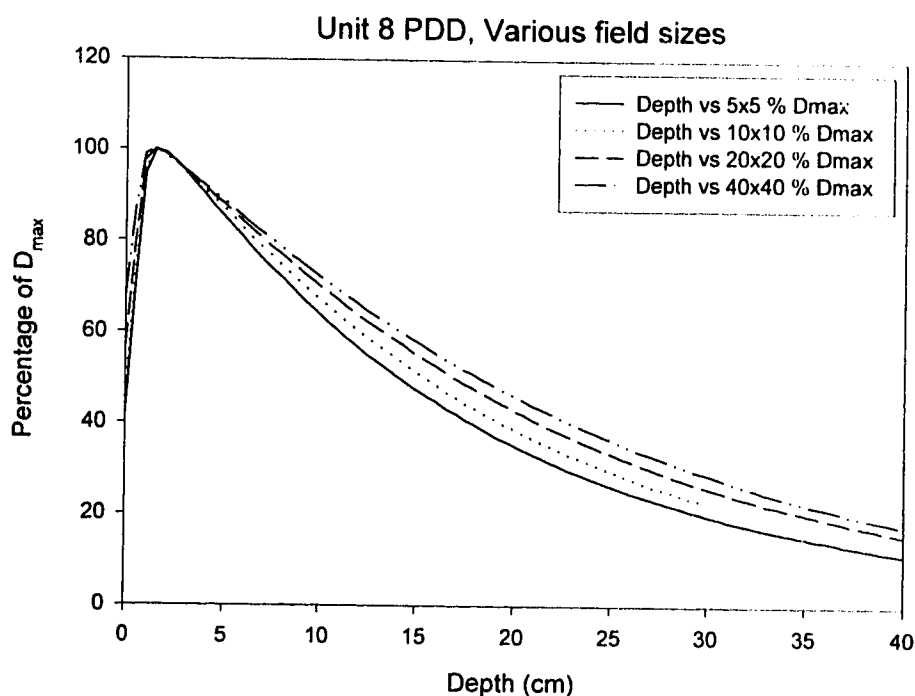


Figure 2.12 Percent depth dose curves for various field sizes, 6 MV beam (Varian 2300 CD)

Percentage depth dose is the measure of the dose at some depth  $d$  along a ray line (usually, but not necessarily the CAX), normalised to the dose at some reference depth, most often the depth of maximum dose. There are a number of functional dependencies which govern the depth dose in phantom: field shape and size ( $w_d$ ), beam energy ( $h\nu$ ) or energy spectrum, and source to surface distance (SSD). Numerically, the PDD is defined as

$$\text{PDD}(\text{SSD}, d, w_d, hv) = \frac{D(\text{SSD}, d, w_d, hv)}{D(\text{SSD}, d_0, w_d, hv)} \quad [2.31]$$

### 2.4.1.2 Tissue Air Ratio

The tissue air ratio, originally called the 'tumour air ratio', was introduced in the 1950's [Johns *et. al.* 1953] to help with treatment planning for rotation therapy. It is the ratio of the dose measured in phantom to the dose measured in a small mass (enough to establish CPE) in air at the same spatial position, that is to say

$$\text{TAR}(\text{SSD}, d, w_d, hv) = \frac{D_{\text{phantom}}(\text{SSD}, d, w_d, hv)}{D_{\text{air}}(\text{SSD}, d, w_d, hv)} \quad [2.32]$$

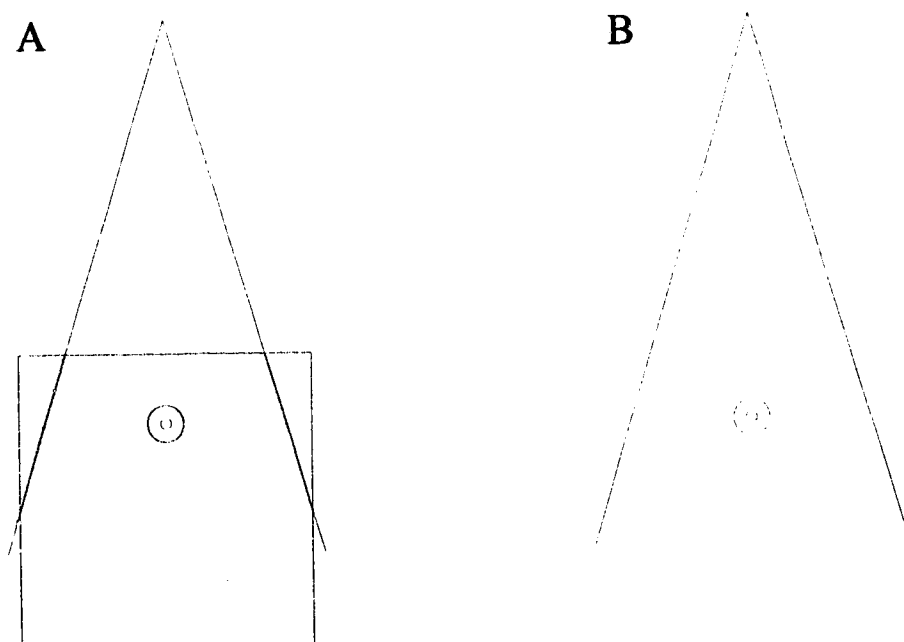


Figure 2.13 Tissue air ratio measurements

### 2.4.1.3 Scatter Air Ratio

The scatter air ratio is a quantity which is related to the tissue air ratio. The difference in dose measured at A as compared to B of figure 2.13 must be due to two things, namely addition of scatter from the surrounding material at A, and attenuation of the primary incident beam by the phantom material above A. By subtracting the

effect of the attenuated primary, a measure of the magnitude of the contribution scatter makes to total dose is obtained. One can obtain a value for the magnitude of the contribution due to the primary radiation at a depth  $d$  by looking at the zero field size TAR, which is

$$\text{TAR}(0) = \text{TAR}(\text{SSD}, d, w_d = 0, hv) = e^{-\mu(d-d_m)} \quad [2.33]$$

where  $d_m$  is depth of maximum dose. A value called the scatter air ratio may now be defined as

$$\text{SAR}(\text{SSD}, d, w_d, hv) = \text{TAR}(\text{SSD}, d, w_d, hv) - \text{TAR}(\text{SSD}, d, 0, hv)$$

otherwise stated as

$$\text{SAR} = \text{TAR}_D - \text{TAR}_0 \quad [2.34]$$

which is to say, the ratio of the dose for field A to C, minus the ratio of the dose for B to D, resulting in the scatter from the area shown at E (cf. figure 2.14)

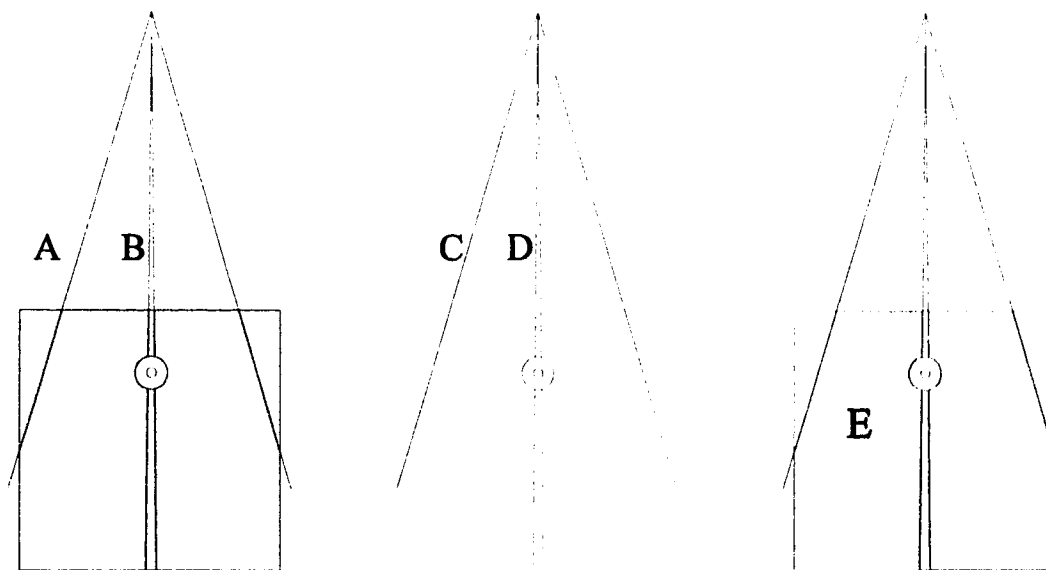
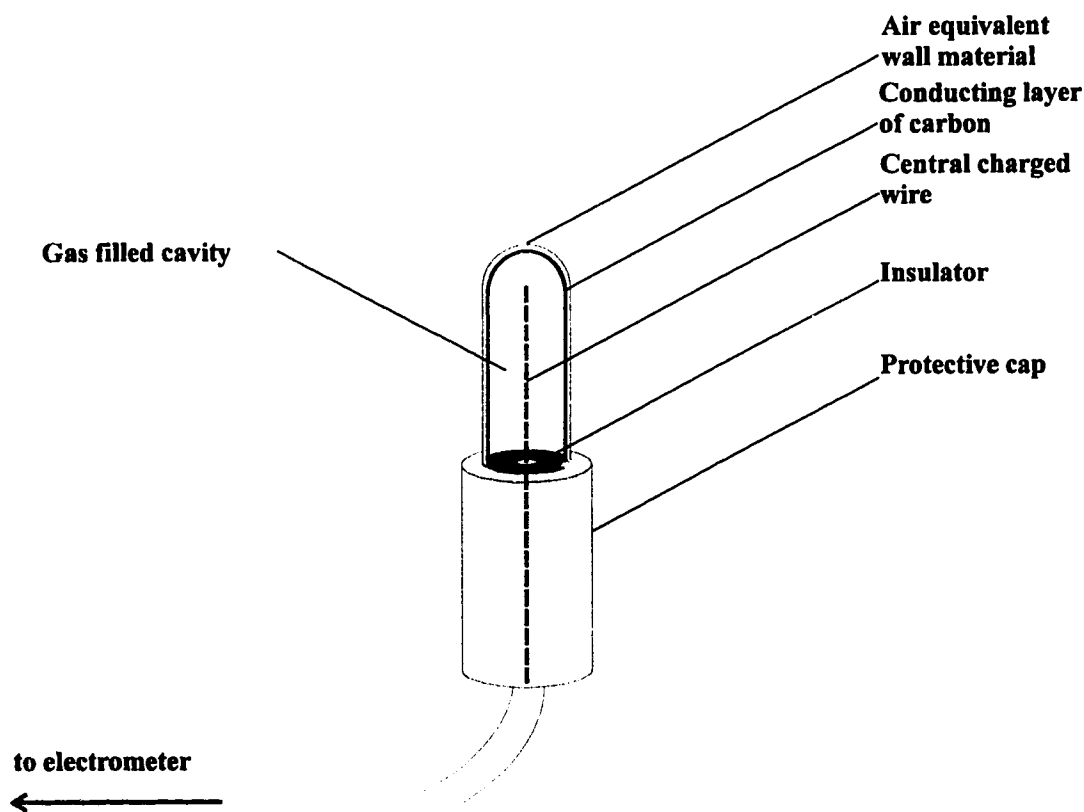


Figure 2.14 Scatter air ratio measurements

#### 2.4.2 Ion chambers

The ion chamber has long been recognised as the gold standard for dosimetric measurements. This is for a number of reasons: high precision, relatively little energy

dependency, relative ease of use, good long term stability and their ability to perform direct measurements, unlike TLDs and film. Furthermore, readings taken from an ion chamber can, upon calibration at a national standards lab (NRC for Canada), be readily and reliably converted to dose [AAPM 1983] through the use of cavity theory. Ion chambers are also popular for relative measurements as well, since the electrometer readouts they produce are directly proportional to dose when CPE exists. The drawbacks of the ion chamber are that it requires electronic equilibrium in order to give meaningful data, a requirement of cavity theory, and it does not lend itself to easy acquisition of time dependent field data (the collection of which requires a number of time consuming point measurements in order to achieve reasonable spatial resolution).



*Figure 2.15 Cylindrical ion chamber*

The basis of ion chamber operation is that it measures the ionisation of the air inside its chamber. For typical practical ion chambers, this is a small volume of air, typically on the order of  $0.1 - 3 \text{ cm}^3$  [Attix 1986]. The mean amount of energy

expended to produce a single ion pair in dry air at NTP,  $W$ , is equal to 33.97 eV (33.97 J/C). This value is roughly invariant over a wide range of electron energies and gas pressures. The ionisation measured can be converted to the exposure,  $X$ , (see [2.5]) for a certain amount of collected charge and known mass of air. This value of exposure can, knowing the value of  $W$ , be related to dose by

$$D_{\text{air}} = \left( \frac{\overline{W}}{e} \right) \cdot X = K_c \quad [2.35]$$

under the assumption of CPE.

For cylindrical chambers (see figure 2.15), there is a central charged wire and an outer charged shell held at a fixed potential (usually around 300 V) with respect to one another. The wall of the chamber is made of a high density material with many of the radiological properties of air. Charge generated in the air volume is collected by either the wire or the outer conductor (depending on the polarity). The charge thus collected is proportional to the radiation dose deposited within the chamber volume and can be related to the dose that would have been given to the medium at that point, using cavity theory as discussed in the previous section. For practical ion chambers, the volume of air used is quite small, so the signals are typically small (this means a longer data acquisition time is required for point measurements compared to other dosimeters).

### 2.4.3 Diodes

Another popular type of detector is the solid state or diode detector (see figure 2.16), such as the silicon-germanium detector (this is a fairly pure piece of silicon, doped with germanium). They function by holding the active material at some potential, and collecting the charge that results when this material is irradiated (as charged particles cross the active volume of the crystal, they form electron-hole pairs).

In contrast to ion chambers, silicon diode detectors often show directional, energy and temperature dependence, and they are damaged by radiation over time (thus varying in output). They do, however, have a very small active area (2mm x 2mm, 50  $\mu\text{m}$  thick), and have good signal amplitude -- the signal from the diode is about ten fold that of ion chambers -- making them ideal for relative measurements. They are chiefly used for electron dosimetry.

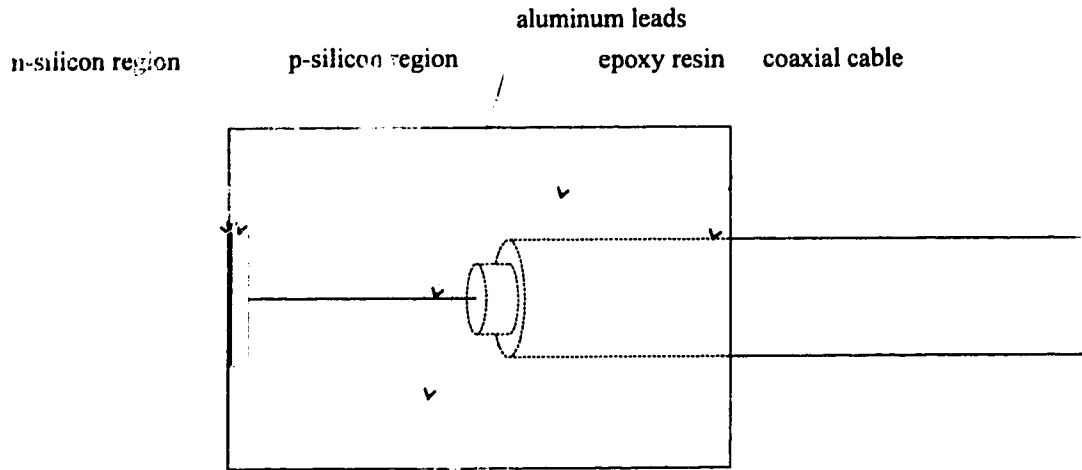


Figure 2.16 The silicon diode detector

#### 2.4.4 Radiographic Film

Film dosimetry is based on the response to irradiation of an emulsion of microscopic grains of the crystal silver bromide (AgBr) on a cellulose substrate. When a film is exposed to a beam of radiation, any parts of the silver bromide crystals which interact with charged particles are converted to neutral silver, and the bromide diffuses into the gel matrix of the film. The neutral silver constitutes a latent image of the field. Developing converts the rest of the silver in the grains to neutral silver. This reaction acts on all the grains, but as it acts much more rapidly in areas with a latent image, the developing is terminated after a very brief time so that only the latent image is revealed. The film is then treated with a stop bath to halt the developing process, and the undeveloped AgBr is then removed with a 'hypo' solution, leaving the opaque silver grains.

The resulting optical density (OD) is measured as

$$OD = \log\left(\frac{I_0}{I_t}\right) \quad [2.36]$$

where  $I_0$  is the incident intensity of the light and  $I_t$  is the transmitted intensity. The optical density is then converted to dose using a calibration function. Film dosimetry of radiation fields has a long history, dating back to the discovery of radiation. The relative response of film was characterised early-on by Hurter and Driffield, and this response is thus named the H and D curve (see figure 2.17).

Film has a number of advantages over other detectors, as well as a number of drawbacks. Film is very dependent on the emulsion (batch characteristics), processing conditions and energy spectrum of the incident radiation. It does, however, have a fair ease of use, very high spatial resolution, good reproducibility, and not only serves as an integrating dosimeter, but also gives a permanent record of the field, once it is processed.

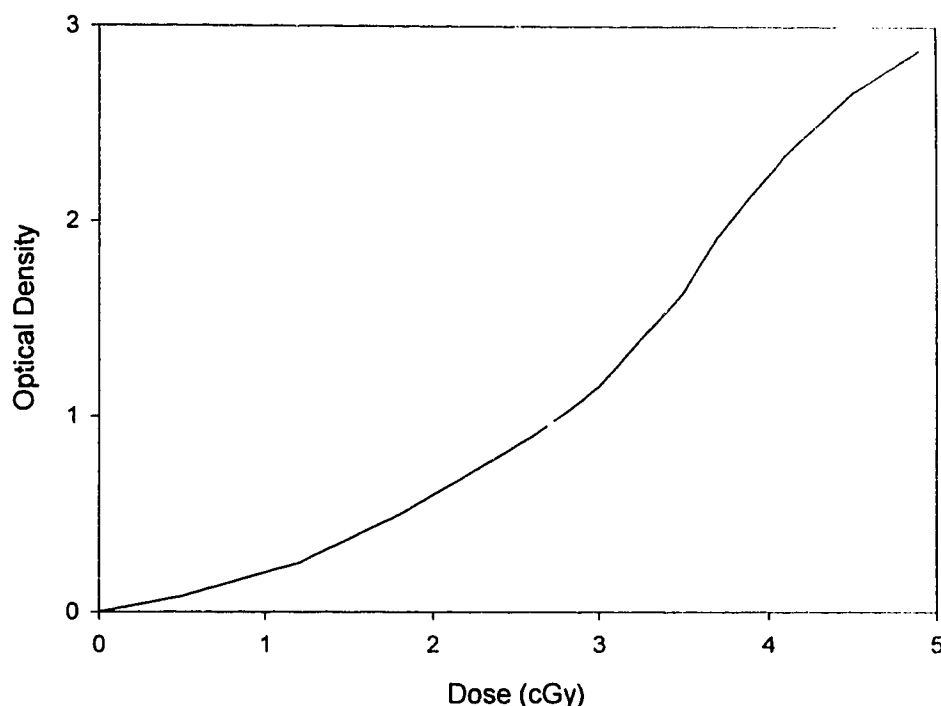


*Figure 2.17 The Hunter and Driffeld (H & D) characteristic film response curve.*

The chief drawback of film is its relative over-response to the low energy component of the impinging radiation field. The relative sensitivity of film for photon energies under 200 keV can be as much as 25 times greater than for photons over 200 keV [Johns and Cunningham 1983]. This is due to the predominance of the photoelectric effect at these low energies. It is particularly problematic for film, as the film response depends on the interaction of the photons with the silver, and the reaction cross section for the photoelectric effect is proportional to the cube of the atomic number (with silver,  $Z=47$ , so the photoelectric effect is particularly pronounced). This leads to a differential response of the film with increasing depth in phantom, initially due to the hardening of the beam and as well due to the increase in the low energy scatter component of the beam.

## Chapter 3

### Dynamic Field Techniques

#### 3.1 Field Delivery

##### 3.1.1 Dynamic Field Simulation From Sum of Static Fields

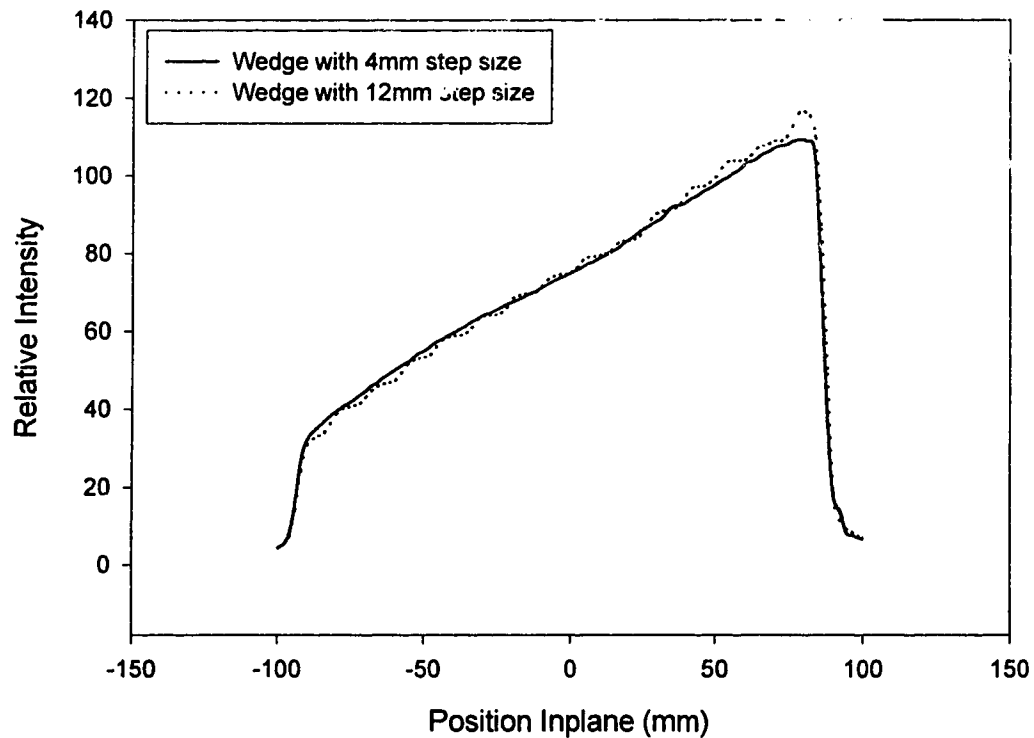


*Figure 3.1 The effect of varying step size on the production of simulated dynamic field (20 by 20 cm<sup>2</sup> field, 6 MV, Varian 2300CD, in-air measurement with film).*

In the absence of true dynamic control over the collimating jaws, dynamic control can be simulated by the summation of static fields, provided that the step size between the jaw movements is small enough. Initially, as has been done by others [Leavitt *et. al.* 1990b], a summation of static fields was employed to simulate the time varying fields that one would obtain from dynamic control over the collimating jaws. It has been demonstrated [Leavitt *et. al.* 1990b] that with a simulated dynamic wedge,



a sufficiently small spacing between the summed segments is required in order to achieve a relatively smooth profile (0.5 cm seems to be sufficient). Experimental results I obtained in our laboratory (see figure 3.1) concur. Some later studies were carried out with dynamic beam delivery research software (referred to as true DBD).

### 3.2 Calculation Techniques

In order to deliver a given dynamic treatment, one must know the jaw positions as a function of time or as a function of cumulative number of monitor units. The solution set of jaw positions as a function of time which will result in a given distribution does not consist of a single unique solution. In order to arrive at a single solution, one must impose a constraint. The constraint employed in this work is that the treatment time for the dynamic field must be a minimum; the clinical justification of this constraint is evident. There are two ways one may arrive at the required position vs. time values: calculate them using some numerical minimisation technique, such as the Simplex method or simulated annealing, or develop the solution analytically. All three of these techniques will be discussed, although I only employed two of them (Simplex optimisation and the analytic approach). The final work was performed exclusively using the analytic solution to the problem for reasons discussed later (cf. section 3.2.3).

The model employed here relies on the constraint of treatment time minimisation in order to calculate a solution for the required jaw motions, or fluence delivery prescriptions, as a function of jaw position in a unidirectional sweep across the field. The model assumes that the input is the desired fluence profile (if a dose profile is entered, the required fluence profile is arrived at iteratively -- cf. section 3.4). Once this is entered, a correction is performed (all corrections are discussed in section 3.3) to the profile to ensure proper output, and then the jaw motions are calculated. Further corrections are performed and the final result is written to a file giving the jaw motions as a function of cumulative monitor unit (MU) delivery. In terms of a flow diagram, the model functions as per figure 3.2.

This flow chart is valid whether the optimal solution is achieved through analytical means or through numerical means, except that the two steps which indicate the calculation of jaw motions would be combined as one in the case of numerical optimisation.

Assumptions made in some recent papers include disregarding penumbral effects, ignoring scattered radiation, and presuming infinite jaw acceleration [Convery and Rosenbloom 1992; Spirou and Chui 1994; Svensson *et. al.* 1994; Yu *et. al.* 1995]. In addition, correcting for the non uniformity of the energy fluence of the beam (the beam profile as measured in air below the secondary collimators) is not sufficient as the effective output is also a function of the field size, a factor not explicitly mentioned in other papers. Further, allowing the fluence rate to vary and examining the consequences of this is dealt with only weakly or not at all in other works.

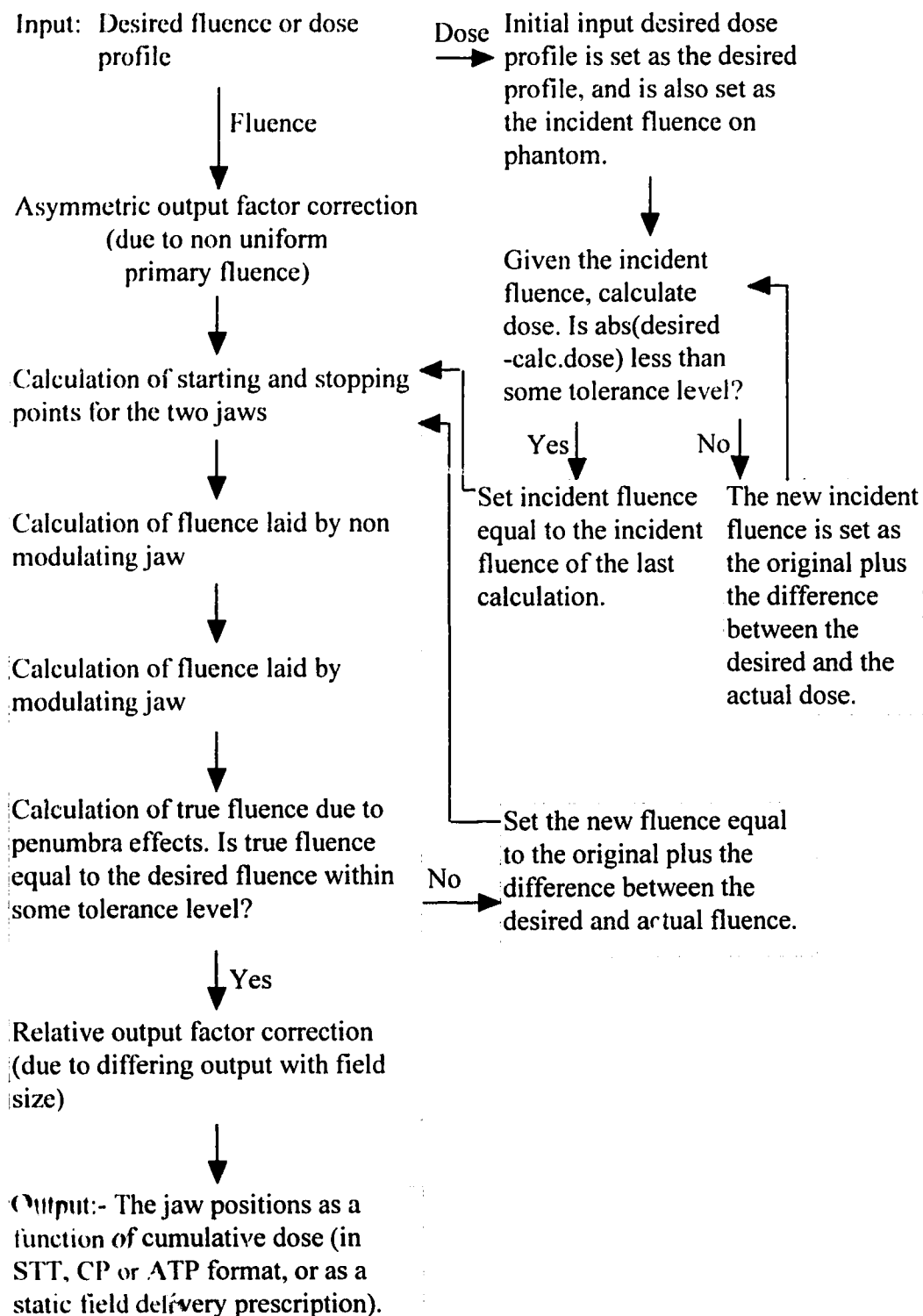


*Figure 3.2 Flow chart of the various actions carried out in the computation of the jaw motions required to produce a given dose or relative energy fluence profile.*

As with other models of this type, the assumption is made that the two jaws will move in a unidirectional sweep across a field. The jaws will initially be in a position such that one jaw defines one edge of the final dynamic field, and the other will initially be positioned somewhere inside the field. At the end of the treatment, the jaw which did not start at the field edge will come to a stop at the other edge of the final dynamic field. The jaw which defines the field edge at the start of the treatment is dubbed the lag jaw, and the jaw which defines the other field edge at the end of the treatment is dubbed the lead jaw. The terms lead and lag jaw are due to the fact that the lag jaw often remains motionless during the beginning of dynamic treatments. The basic constraint for this problem is

$$I(x) = I_{\text{lag}}(x) - I_{\text{lead}}(x), \quad \text{or} \quad [3.1]$$

$$\Psi(x) = \int_0^{t_{\text{total}}} \Psi_{\text{lag}}(x) - \int_0^{t_{\text{total}}} \Psi_{\text{lead}}(x)$$

where  $I$  is the intensity in MU, and  $\Psi$  is the energy fluence. This is to say that the net fluence to a point is the cumulative fluence delivered between the time the lead jaw exposes a point and the lag jaw covers that same point. It should be noted that the intensity  $I$  to a point is directly proportional to the fluence at that same point.

The model I used in this work employs an analytic approach to the problem of calculating required jaw motions. Use of maximum jaw speed by one of the jaws is indicated by the results of the Simplex method, and a simple proof of this has been published [Spirou and Chui 1994]. At present, infinite jaw acceleration is assumed, but lacking real time control over collimator motion renders this point moot. The validity of this assumption may, however, be questioned in the case of certain extreme examples. Given that the model employs two independent jaws, and not a multileaf collimator (MLC), one is free to vary the dose rate in order to achieve smaller differences between field segments (for individual cumulative jaw fluence), or lower net fluence to a low fluence region (other approaches to this problem have involved slowing down the non-modulating jaw while still in the non-modulating region, although this would increase overall treatment time, and is therefore not desirable). The fluence rate for the two jaws may be adjusted accordingly.

### 3.2.1 Dynamic Wedge Calculation

As an example of a dynamic beam calculation, let us look at the technique originally used to calculate the dynamic wedge. In order to achieve some desired effective wedge angle, the beam must be modulated such that the heel of the 'wedge' (the part receiving the least radiation) transmits the beam for only part of the treatment, whereas the toe of the 'wedge' (the part receiving the most radiation) transmits for the entire duration of the treatment. As well, in accordance with the definition of wedge angle, the isodose line through the 10 cm depth point on the CAX

(dashed line at left, figure 3.3) must be at the desired angle  $\theta$  to an isodepth line at 10 cm (this is the IEC definition of the wedge angle). The original paper put forth for the calculation of the required jaw positions as a function of time for a given wedge angle [Kijewski *et. al.* 1978] gave the jaw positions for a desired wedge angle and field size, as well as for an arbitrary depth of definition. The calculation by Kijewski *et. al.* is an iterative technique which first assumes an open, stationary field. With this as the initial assumption, the dose along a line at the desired wedge angle  $\theta$  to the isodepth line is calculated (see figure 3.3, at left). The dose profile along this line will be sloped in shape (see figure 3.3, line A).

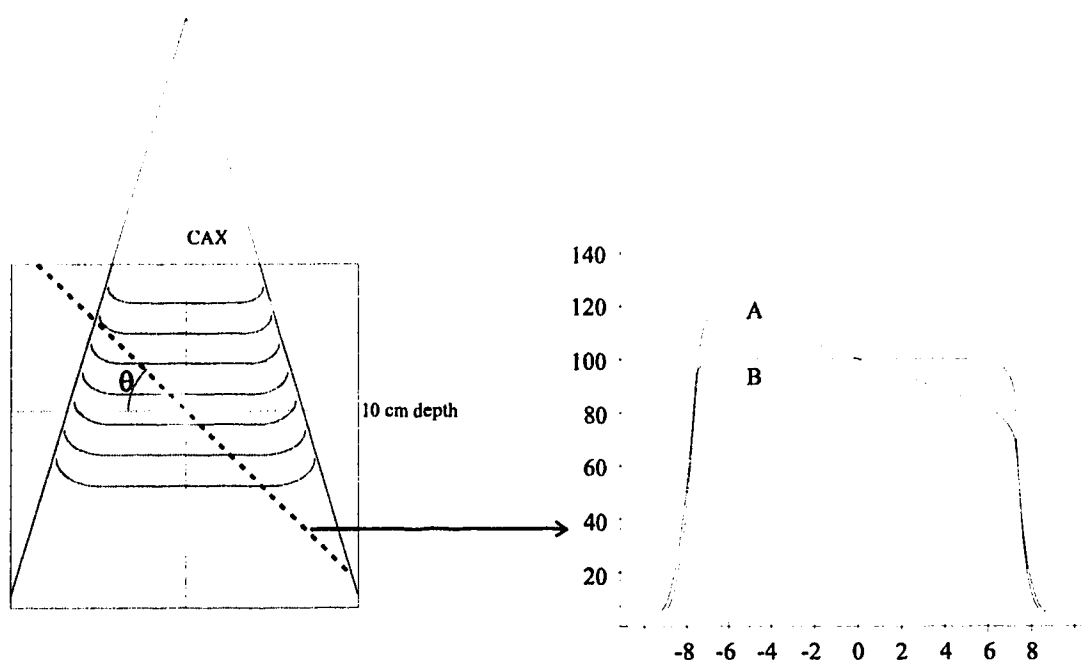


*Figure 3.3 The relative dose as measured along a line at 45 degrees to the 10 cm depth line for an open field (A, shown at right), and the desired dose profile along this line for a 45 degree dynamic wedge (B, also at right).*

Instead of a sloped line, a straight line is desired -- a uniform dose along the line at angle  $\theta$  to the isodepth line (see figure 3.3, line B). With this in mind, and assuming that the dose at the reference depth and on the CAX is correct, one must increase the relative amount of time an underdosed point is exposed to the beam, and likewise decrease the relative time an overdosed point is exposed. After calculating the dose for the open field (the first iteration), the new exposure time,  $t_2$ , for a point (x,z) is given by

$$t_2(x) = t_1(x) \frac{D(0, d)}{D_1(x, z)} \quad [3.2]$$

This is not the solution, since changing the relative weightings of the different parts of the beam changes the amount of scatter, so one must iterate toward the final solution, recalculating the dose each time. Eventually one converges on the  $(i+1)$  iteration to

$$t_{i+1}(x) = t_i(x) \frac{D(0, d)}{D_i(x, z)} \quad [3.3]$$

which is to say that the amount of time calculated for any given point  $x$  for the  $i+1$  iteration is equal to the amount of time calculated by the  $i^{\text{th}}$  iteration, times the ratio of dose on the CAX at the depth of angle definition to the dose at the point  $x$  for the amount of time for the  $i^{\text{th}}$  iteration.

### 3.2.2 Numerical Optimisation

The computer analysis which was used initially in this work was loosely based on the simple model proposed by Convery and Rosenbloom [Convery and Rosenbloom 1992]. Given an intensity profile in monitor units (MUs) as a function of a one-dimensional field position value, the jaw motions required to produce this field are determined. This model assumes a single unidirectional sweep of both jaws. It sets up the problem by considering the number of cumulative MUs delivered by the time the jaws reach given field positions. One jaw is denoted the A jaw, and the other the B jaw. The A jaw delineates the start of the field, and the B jaw delineates the end. The difference between the cumulative number of MUs delivered by the time the A jaw or the B jaw reaches some given point  $x$  gives the set of equality constraints on the problem; this difference must be equal to the desired intensity at that point (cf. [3.1]). A set of inequality constraints can be calculated based on the maximum velocity of the jaws during treatment, creating a lower bound on the number of MUs that can be delivered between two points. The constraints describing the problem are set up in the form of a matrix, and with the cumulative number of MUs delivered by the time the A jaw reaches its final point as an objective function, the matrix is minimised by the Simplex method.

The model as presented by Convery and Rosenbloom ignores the effect of collimator scatter and leakage, as well as penumbral effects (i.e. it assumes perfect collimation). Variation in output as a function of field position and size is also not addressed in their paper. As well, they start with a desired intensity profile (MUs vs field position), when for most practical applications, one would wish to start with a desired dose profile (cGy vs. field position).

### 3.2.2.1 Simplex

There are numerous numerical techniques which may be used for calculating the optimal jaw motions required to produce a desired energy fluence profile. Two such methods are simulated annealing and simplex optimisation.

Simplex optimisation [Press *et. al.* 1989; Gill *et. al.* 1981], which was used in the early studies of the dynamic collimation problem for this work, was used to determine optimal jaw motions for a given input intensity profile, subject to the following constraints:

- a) The equality constraint that the cumulative number of MUs delivered between exposing and covering up a point by the jaws must be equal to the number of desired MUs to be delivered to that point.
- b) Jaw velocity is constrained not to exceed the maximum allowed jaw velocity at any time.
- c) Minimisation of the overall treatment time.

The simplex method, arrived at in 1948 by G.B. Dantzig, is an iterative matrix calculation technique which converges on an optimal solution, given a set of constraints.

The general form of the Simplex problem takes the form of maximising, or minimising, a given equation:

$$f = c_1x_1 + \dots + c_nx_n$$

subject to a set of equality constraints of the form

$$\begin{aligned} a_{11}x_1 + \dots + a_{1n}x_n &= b_1 \\ a_{21}x_1 + \dots + a_{2n}x_n &= b_2 \\ &\dots\dots\dots \\ a_{m1}x_1 + \dots + a_{mn}x_n &= b_m \end{aligned}$$

as well as a set of inequality constraints of the form

$$x_i \geq 0 \quad (i = 1, \dots, n)$$

Once the problem is so formulated, there are essentially three operations that are performed:

- 1) Test for convergence to optimal solution

- 2) Determine a better solution
- 3) Make transition to the better solution

The process then starts over with step 1.

The problem is formulated in terms of a matrix, and a number of linear operations are performed on the matrix in order to achieve the desired optimal solution. To define a few terms, the function for which the optimal solution is sought is known as the objective function, any set of numbers  $x_1 \dots x_n$  that satisfy the constraints of the problem are termed to be a feasible vector, and the optimal solution for the problem is therefore known as the optimal feasible vector.

Example:

Suppose one wishes to optimise the function

$$z = 2x_2 - 4x_3$$

subject to the constraints

$$\begin{aligned} x_1 &= 2 - 6x_2 + x_3 \\ x_4 &= 8 + 3x_2 - 4x_3 \\ x_i &\geq 0 \quad (i = 1, \dots, 4) \end{aligned}$$

This may be stated in the form of a table (Table 3.1)

	Constants	$x_2$	$x_3$
$z$	0	2	-4
$x_1$	2	-6	1
$x_4$	8	3	-4

*Table 3.1 Initial tableau for Simplex optimisation*

The tableau, as it is called, is arrived at by setting the right hand variables ( $x_2$  and  $x_3$ ) to zero, giving the leftmost entries (the constants column). This left hand column represents the initial feasible vector (if any of the basic variables are negative, one must rearrange to get new basic variables). The remaining rows (1,2 ; 1,3), (2,2 ; 2,3) and (3,2 ; 3,3) represent the coefficients of the right hand side of the equality constraints.

The condition indicating optimisation is that the coefficients in the z row must be zero or negative -- a negative sign indicates that the column in question cannot increase in value since, by the inequality constraint,  $x_i$  must be greater than or equal to zero and one cannot make z larger by increasing the value of the variables in that column. If the initial feasible vector is not optimal, one must move to another feasible solution for z which is larger. This begins by optimising a column (a right hand variable) with a positive z row coefficient. The column is chosen by finding the one which has the element which first blocks further increase (the basic variable cannot become negative!), and amongst those elements that first block increase, it gives the largest increase. This element will be called the pivot element.

Any positive elements in the column of interest (the  $x_2$  column in this case) will not restrict the increase of this variable, since increasing it will not drive any of the left hand variables negative. One must find which of the negative entries in this column will first limit the increase of this right hand variable. This entry is the called the pivot element -- it will be the negative element which, when the element in the constant column is divided by it, gives the smallest value. If one must decide amongst several possible pivots, then it must be determined which one yields the largest possible overall increase: the change in the optimal feasible vector will be

$$\left| \left( \frac{\text{const.}}{\text{pivot}} \right) \text{z row element} \right|$$

The only such column in this case is the  $x_2$  column, where the z row entry is 2. This variable  $x_2$  is now increased from its present value of 0. Due to the constraint that all variables must be greater than zero, one must increase the variable without driving one of the right hand variables negative. The pivot (-6 in this case) is identified and given the maximum increase possible without driving the basic variable negative (it goes to zero). The new value of  $x_2$  is found by exchanging it with  $x_1$ , which is the basic variable whose row intersects the pivot element's column. Solving the  $x_1$  row for  $x_2$ ,

$$\begin{aligned} x_1 &= 2 - 6x_2 + x_3 \\ 6x_2 &= x_3 - x_1 - 2 \\ x_2 &= 1/6x_3 - 1/6x_1 - 2/6 \end{aligned}$$

Substituting this into the old z row, one gets

$$\begin{aligned} z &= 2x_2 - 4x_3 \\ &= 2(1/6x_3 - 1/6x_1 - 2/6) - 4x_3 \\ &= 1/3x_3 - 1/3x_1 - 2/3 - 4x_3 \end{aligned}$$



$$= 11/3x_3 - 1/3 x_1 - 2/3$$

What effectively is being done is moving one of the basic variables out of the position of 'basic variable', and setting it equal to zero (becoming a right hand variable), and exchanging it with one of the right hand variables, which now becomes a basic variable.

Inspecting the new tableau, it can be seen that it has converged on an optimal solution (all the coefficients in the z row are negative) and thus the process is complete.

	Constants	$x_1$	$x_3$
z	2/3	-1/3	-11/3
$x_2$	1/3	-1/6	1/6
$x_4$	9	-1/2	-7/2

*Table 3.2 Final tableau for Simplex optimisation*

The optimal solution is therefore  $z = 2/3$ , and this is found when  $x_2=1/3$ ,  $x_4=9$ , and  $x_1=x_3=0$ .

### 3.2.2.2 Simulated Annealing

Simulated annealing [Metropolis *et. al.* 1953], also called combinatorial minimisation, is a computational process which derives its name from the physical process of annealing. An initial guess of the solution (again, an initial feasible vector) is defined, and then one randomly computes changes to the initial guess. One defines a objective function to determine whether the initial feasible vector will change its state to a new value -- this will allow all vectors to change their state to some other state. This change is always made for any solution which is more optimal, but not always made for 'uphill' guesses which temporarily move away from an optimal solution; a probability function determines the likelihood of an 'uphill' change. The probability that any given vector will change its state upward gets smaller with each successive iteration, and the probability of an individual change depends on how much larger the objective function becomes.

The probability, because of the statistical thermodynamics analogy being used, is based on the Boltzmann probability distribution, namely

$$P(E) \sim e^{-\frac{E}{kT}} \quad [3.4]$$

In the case of simulated annealing, the energy  $E$  corresponds to the value of the objective function being minimised, and  $T$  is the 'temperature' -- a user defined parameter whose value drops at some rate as a function of the number of iterations. Since this is a minimisation problem, the goal is to achieve the lowest value of  $E$  possible. As with physical annealing, the system 'slowly' (in terms of number of iterations, not necessarily in terms of calculation time) settles into a near-global minimum. The probability of any change is

$$p = e^{-\frac{(E_2 - E_1)}{kT}} \quad [3.5]$$

where  $E_2$  is the value of the new guess and  $E_1$  is the value of the previous guess. One can see that for any values of  $E_2 < E_1$ , one gets  $p > 1$ , so the change is certain. If  $E_2 > E_1$ , it is still possible for the objective function to change to this new value even though it is larger than the current solution. It is this feature of the technique which allows one to avoid getting caught in a local minimum, and to continue to strive toward a global minimum. The convergence time for this method is usually on the order of a small power of  $N$ , where  $N$  is the number of points defining the initial feasible vector [Press *et. al.* 1989], and will converge on a relatively minimal, if not absolutely minimum, solution which often cannot, in practice, be improved upon to any great degree.

### 3.2.3 Analytic Solution

Arriving at the solution to the dynamic treatment problem analytically has definite advantages in terms of calculation times, a solution for some cases being arrived at orders of magnitude faster than by numerical optimisation techniques [Svensson *et. al.* 1994]. It is for this reason that the numerical optimisation technique was abandoned in favour of this technique.

Consider a desired energy fluence profile (see Figure 3.4). For any given point  $x$ , the net energy fluence delivered during a dynamic treatment is equal to the difference between the cumulative energy fluence that, in the absence of the lead jaw, would have been delivered prior to that point being exposed by the leading jaw and the cumulative energy fluence delivered before it is again covered by the lagging jaw. In other words,

$$\psi_E(x) = \int_0^{t_{lag}} \psi_{E_{lag}}(x) - \int_0^{t_{lead}} \psi_{E_{lead}}(x)$$

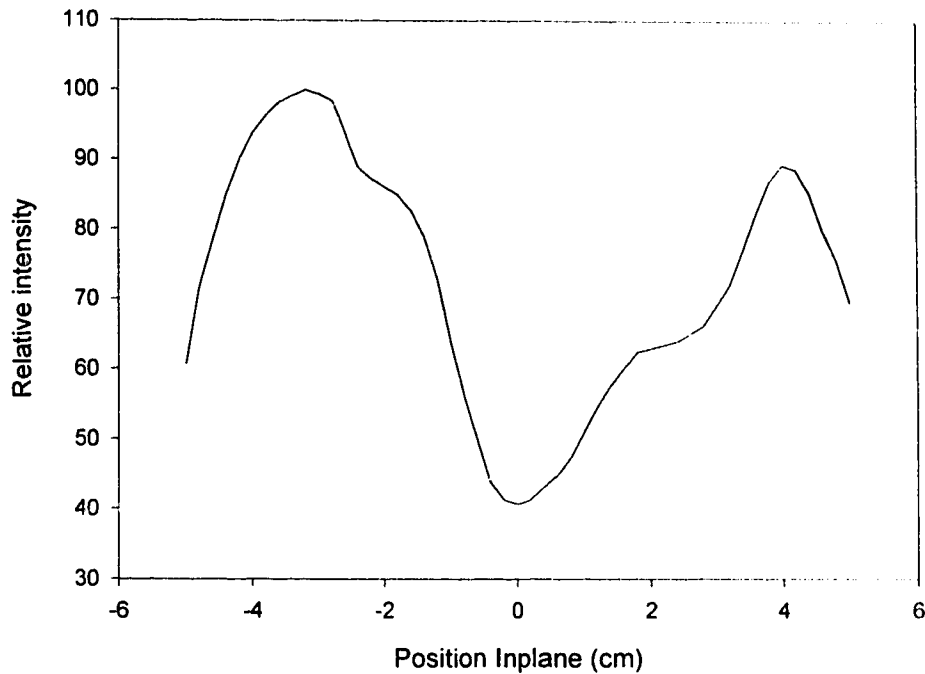


*Figure 3.4 An example of a relative dose or relative energy fluence profile.*

For any point  $x$  one has  $\Psi_E(x) = k(x) I(x)$ , where  $I$  is the intensity of the field, measured in arbitrary monitor units (MUs), and  $k(x)$  is a conversion function. Given this, the relationship can be restated in terms of MUs as

$$I_{\text{net}}(x) = I_{\text{lag}}(x) - I_{\text{lead}}(x)$$

where  $I_{\text{net}}$  is the desired or prescribed intensity. This is the commonly stated form of the equality constraint that is placed on the problem. The solution set for this equation is unbounded (all that needs to be done is to ensure that the desired intensity at point  $x$  is delivered between the time  $x$  is uncovered by one jaw and covered again by the other).

For a fixed 'dose rate'  $R$  (typically measured in MU/min), the jaw velocity for either of the two jaws in a given interval  $\Delta x$  is

$$v_{\text{jaw}} = (\Delta x) / (\Delta t) \quad [3.6]$$

and the change in cumulative intensity for the same interval, may be given as

$$\Delta I = (R)(\Delta t) = (R)(\Delta x) / (v_{\text{jaw}})$$

therefore, from the above, and [3.1],

$$\Delta I_{\text{net}}(x) = (R)(\Delta x) / (v_{\text{lag}}) - (R)(\Delta x) / (v_{\text{lead}}) \quad [3.7]$$

Dividing  $\Delta I_{\text{net}}(x)$  by the intensity rate  $R$  gives  $\Delta t_{\text{net}}(x)$ , the time for which point  $x$  is exposed to the beam. Further dividing by  $(\Delta x)$ ,

$$\Delta t(x) / (\Delta x) = 1 / (v_{\text{lag}}) - 1 / (v_{\text{lead}}) \quad [3.8]$$

which is to say that the time that any point  $x$  is exposed to the beam (which is directly related to the energy fluence at that point) is equal to, for a fixed dose rate  $R$ , the difference of the inverse jaw velocities. This can lead to several interesting conclusions. Imposing the further constraint that the dynamic treatment should be delivered in a minimum amount of time, which is a clinically useful constraint, then one can say that for a desired section of a profile  $\Delta I(x)$  with a positive gradient one must have  $(v_{\text{lead}}) > (v_{\text{lag}})$ ; similarly, for a desired section of a profile  $\Delta I(x)$  with a negative gradient,  $(v_{\text{lag}}) > (v_{\text{lead}})$ . In fact, stating that

$$\frac{(t_{\text{open}})}{(\Delta x)} = F(v_{\text{lag}}, v_{\text{lead}}) = \frac{1}{(v_{\text{lag}})} - \frac{1}{(v_{\text{lead}})}$$

where  $t_{\text{open}}$  is the amount of time a point is exposed, then the optimal solution is arrived at when

$$\left. \frac{\partial}{\partial v_{\text{lead}}} F \right|_{v_{\text{lead}} = \text{optimal}} = \left. \frac{\partial}{\partial v_{\text{lead}}} \left( \frac{1}{v_{\text{lag}}} - \frac{1}{v_{\text{lead}}} \right) \right|_{v_{\text{lead}} = \text{optimal}} = 0 \quad [3.9]$$

so that the solution converges to the shortest possible treatment time in this example as the lead jaw velocity tends toward infinity; i.e., the fastest jaw velocity possible for one of the jaws at all points gives the shortest possible treatment time. This a priori knowledge of one jaw velocity, and hence its contribution to  $I(x)$  allows, using the

equality constraint [3.1], the calculation of the other jaw's necessary contribution, and hence its velocity.

Alternatively, one may show, using proof by counter-example, that employing the maximum jaw speed for one of the jaws yields the minimum treatment time [Spirou and Chui 1994]. As well, one may compare results from this method to those obtained by Simplex minimisation to arrive at identical results.

### 3.3 Dynamic Field Corrections

In order to correctly deliver a prescribed dynamic treatment, one must examine a number of assumptions that have been made by others [Convery and Rosenbloom 1992; Svensson *et. al.* 1994; Spirou and Chui 1994] namely: uniform energy fluence with field position relative to the central axis, output does not vary with field size, and perfect collimation. If these assumptions prove to be invalid, then corrections must be made in order to account for them. All correction factors were tested with the Varian 2300CD, 6MV beam setting.

#### 3.3.1 Relative Output Off the CAX (AOF)

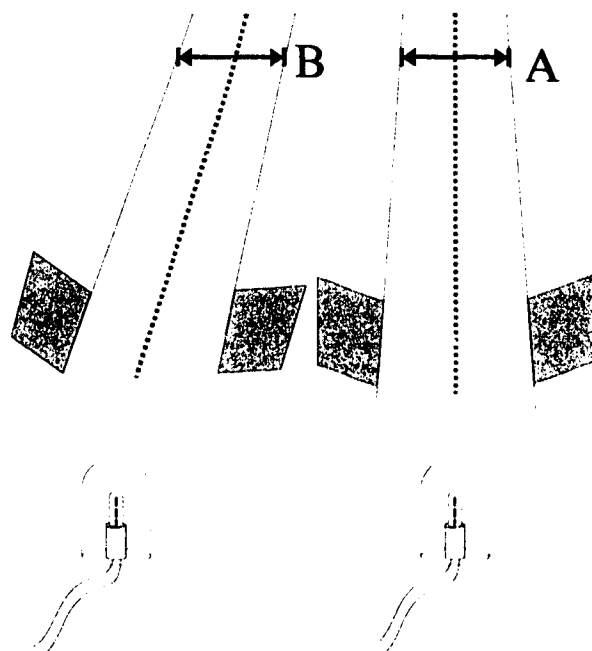


Figure 3.5 Measurement of asymmetric output factors.

The output for a particular asymmetric field of a given size relative to the output for a symmetric field (about the central beam axis) of the same size differs by a value which has been termed the Asymmetric Output Factor (AOF). This variation in output for two identically sized fields, one on the CAX and the other with an asymmetric offset (cf. figure 3.5), is due largely to the non-uniformity of the open field fluence profile. Numerically, the AOF is given by

$$\text{AOF} = \frac{\Psi_{\text{centre, field B}}}{\Psi_{\text{CAX, field A}}} \quad [3.10]$$

The primary fluence values for the field vary radially from the central axis in a well known manner (cf. 2.3.2), and this is due to the combination of the distribution of the bremsstrahlung radiation produced by the target, and the presence of the beam flattening filter which is designed to compensate for the bremsstrahlung distribution in such a fashion as to produce a flat dose profile at 10 cm depth in a flat, semi-infinite water phantom. The fluence variation for equally sized fields at various radial distances from the CAX was measured in order to determine AOF values.

### 3.3.1.1 Determination of AOF Values

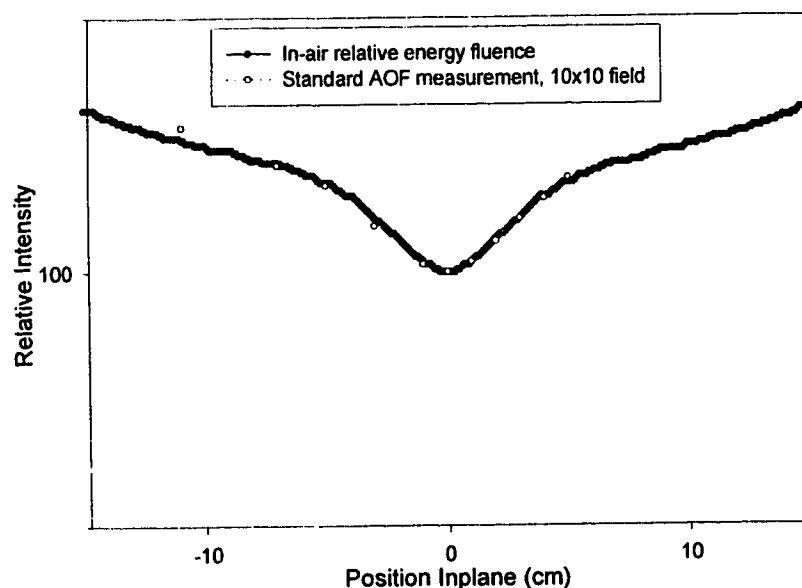


*Figure 3.6 Comparison of asymmetric output factors and in air beam profile (6MV beam, Varian 2300CD, ion chamber).*

One may compare the AOF values measured in the manner described in 3.3.1 to the open field in-air relative energy fluence profile (see figure 3.6), one finds the value of the in-air profile, at the point equal to the asymmetric offset, to be numerically equal to the AOF measured at that offset. Thus AOF values may be determined directly from the open field in-air relative fluence profile.

The relative value of the field intensity as a function of off-axis distance is determined from an in-air measurements in a large open field. Translating an ion chamber, with an appropriate minimum of buildup material across the maximum field size available yields the relative energy fluence profile. Buildup, just sufficient for the establishment of electronic equilibrium, effectively screens out contaminant electrons in the beam, and provides a signal from the electrometer which is proportional to the energy fluence at the point of measurement. A typical measurement for a  $40 \times 40 \text{ cm}^2$  field is shown in figure 3.7. Ignoring the penumbral region at the outer field edge, one can extrapolate the known data outward using linear interpolation to determine the fluence below the collimator jaws to the maximum radius available (see figure 3.8); this linear extrapolation seems to be valid for radii greater than 3 cm.

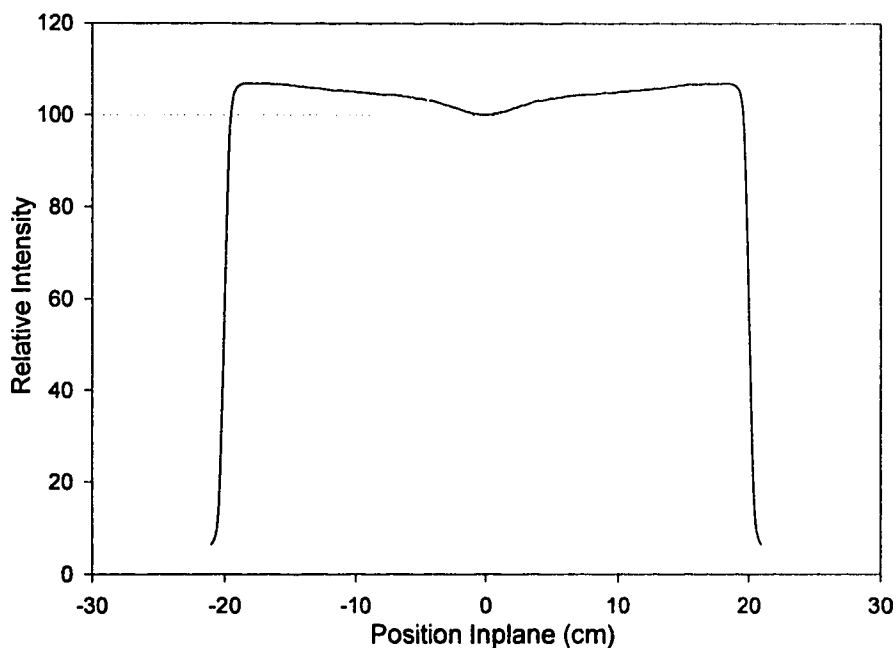


*Figure 3.7 Measurement of the in-air profile for a  $20 \times 20 \text{ cm}^2$  field (6MV beam, Varian 2300CD, ion chamber).*

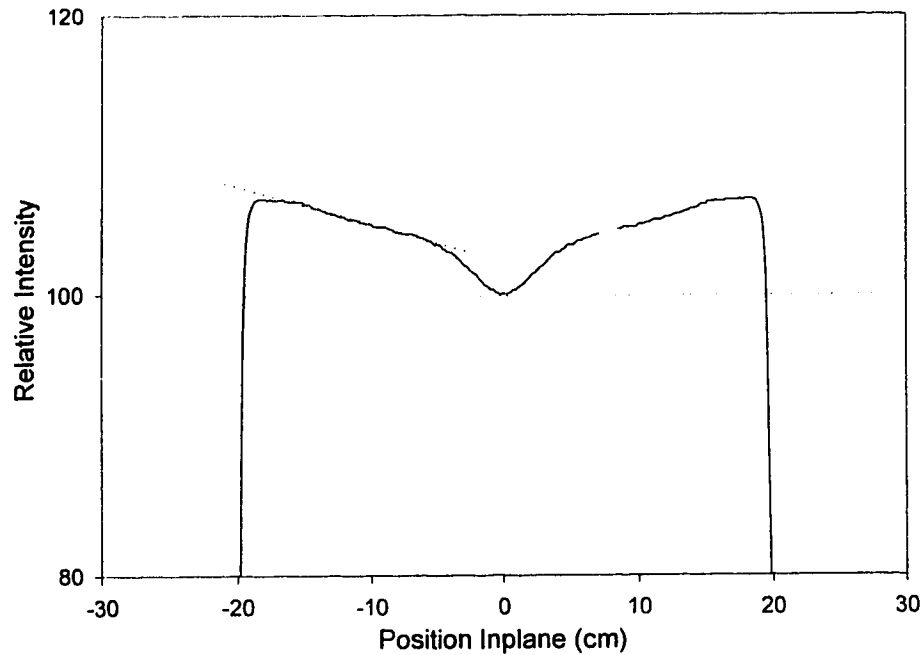


Figure 3.8 Extrapolation of measured in-air profile for a 20x20 cm<sup>2</sup> field (6MV beam, Varian 2300CD, ion chamber).

### 3.3.2 Relative Output With Field Size (ROF)

Another well established effect is the variation in linear accelerator output with field size. By setting the number of monitor units to a fixed value and varying only the settings of the secondary collimator jaws, substantial variations in measured output from the linac are observed. The ROF for a given field of dimensions (x,y) is defined as

$$\text{ROF}(\text{field size}) = \frac{\Psi_{\text{air}}(X \times Y)}{\Psi_{\text{air}}(10 \times 10)} \quad [3.11]$$

where  $\Psi_{\text{air}}(10 \times 10)$  is the energy fluence measured on the CAX for a 10 x 10 cm<sup>2</sup> symmetric field.



### 3.3.2.1 Determination of ROF Values

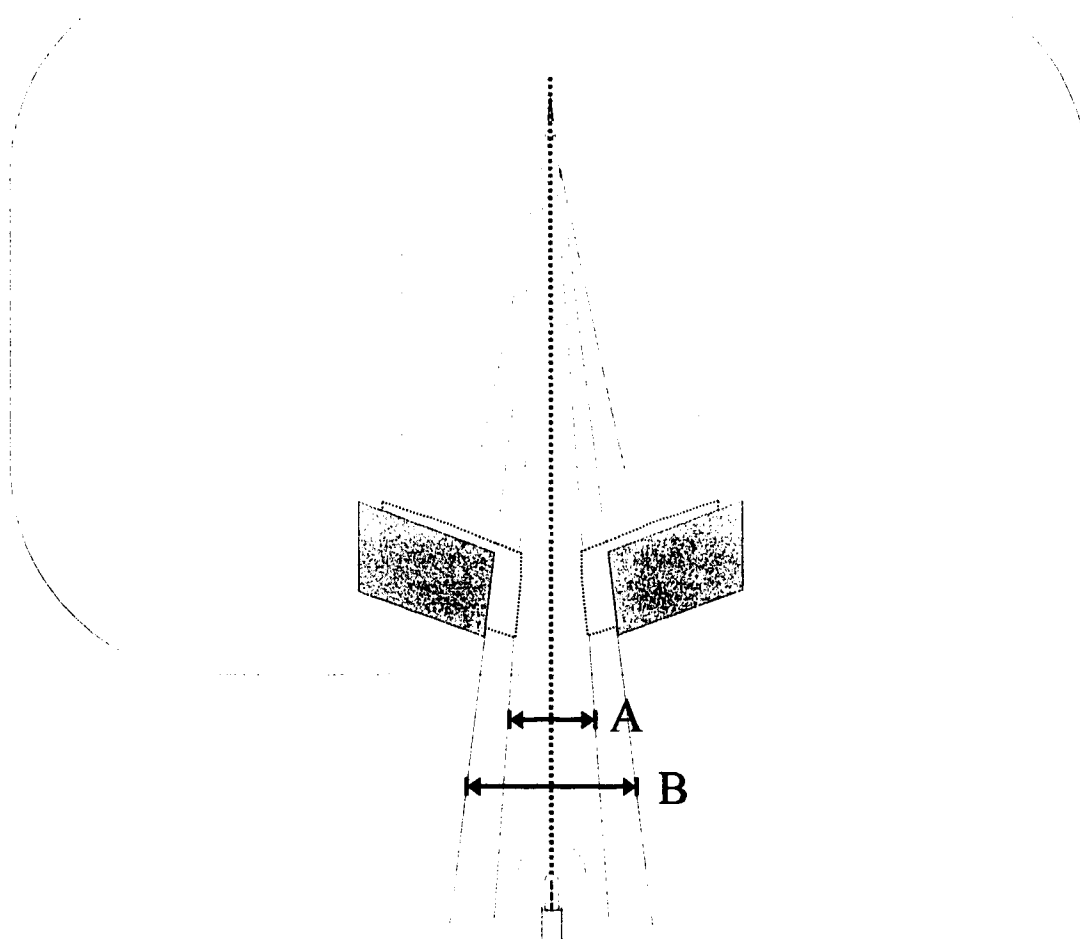


*Figure 3.9 Experimental method of measuring relative output factors.*

The means for the determination of these values is quite straightforward. A measuring device, such as an ion chamber or diode, with a suitable minimum amount of buildup medium (referred to as a buildup cap) is placed at isocentre. A fixed number of monitor units are delivered for fields of various jaw separations which are symmetric about the CAX. The charge collected by the electrometer is directly proportional to the relative amount of energy received for this field. The electrometer reading is recorded, and normalised to the electrometer reading for a  $10 \times 10 \text{ cm}^2$  field. These values are then put into a suitable form for use as correction factors (such as a table or a graph -- see figure 3.10).

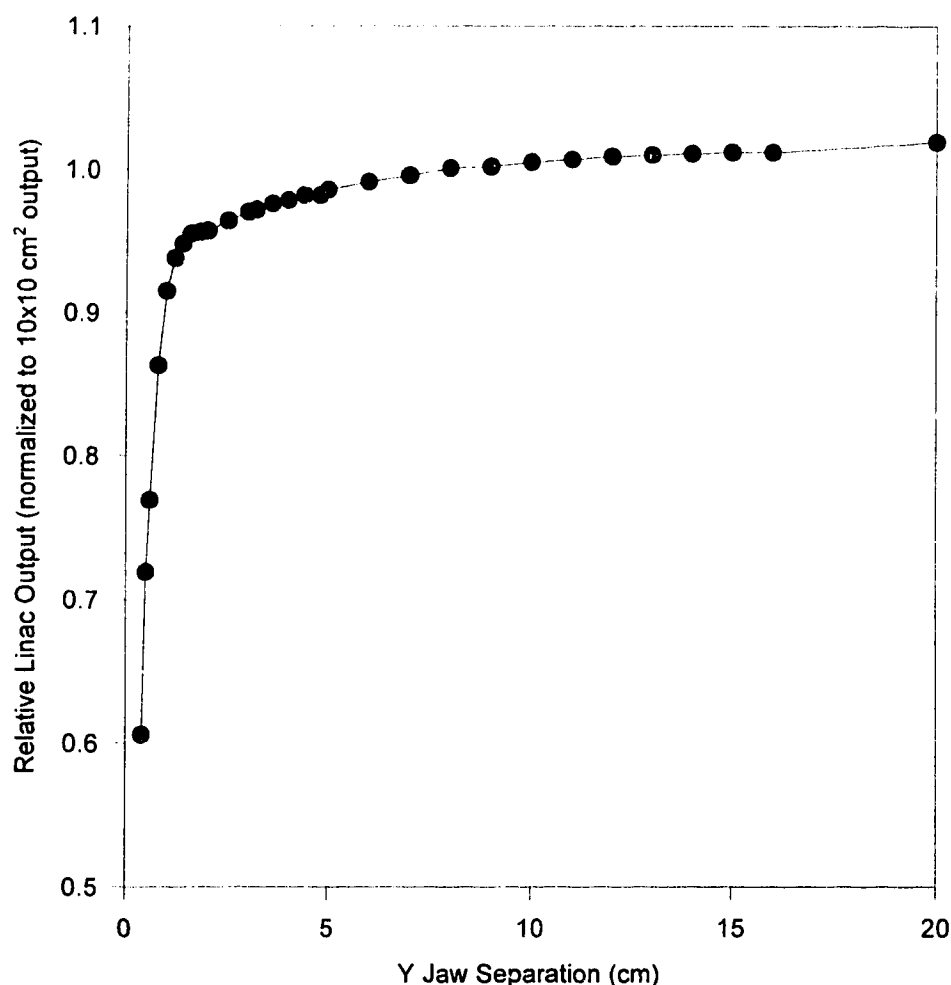


*Figure 3.10 Relative output factors as a function of field size with X jaws fixed (6MV beam, Varian 2300CD, ion chamber).*

The varying field sizes required for a dynamic treatment, given a desired profile, correspond to the full range of possible jaw separations. Some of the field sizes (as defined at isocentre) for which ROF values are required are smaller than the diameter of the buildup cap. This would result in the loss of electronic equilibrium, making the relative measurements no longer meaningful. In order to circumvent this limitation, the detector was moved to a suitable distance so that the effective field size at that distance was greater than the diameter of the buildup cap. This was accomplished by rotating the gantry to 270 degrees and taking the readings at a source to detector distance (SDD) of approximately 4.5 metres.

The readings taken at the greater distance are for a number of field sizes and normalised to the reading for a jaw setting of a  $10 \times 10 \text{ cm}^2$  field at isocentre as before. Readings for the larger field sizes are compared to previous readings taken at isocentre (100 SSD), and the correlation ( see figure 3.11) indicates this to be a valid

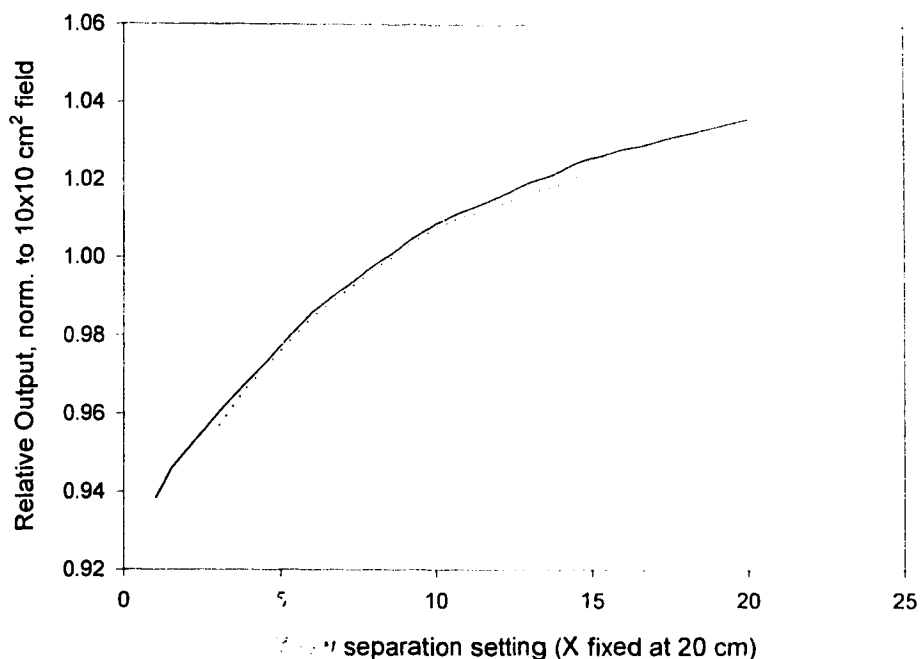


*Figure 3.11 Relative output factors as a function of field size for standard (dotted) and far field (solid) measurements.*

method for measuring ROF values (the maximum variation is about 0.6 %, or about 0.007 absolute difference, in the values when normalised to a 10 by  $10 \text{ cm}^2$  field output). The agreement is best for the smaller field sizes.

### 3.3.3 Collimation and Penumbra Effects

The dynamic fields generated in this work employ the time varying position of the secondary collimating jaws to define the field intensity. One may assume perfect collimation at the field edges, but this assumption is not correct. Any field produced by a linear accelerator will have a region at the field edges where the primary energy fluence drops away toward zero, but this occurs over the space of several millimetres (the penumbral width is typically measured from the 20% to the 80% points; for

figure 3.12 this width is about 5mm). This drop may be modelled using certain assumptions about the source, the gantry head and their respective geometries.

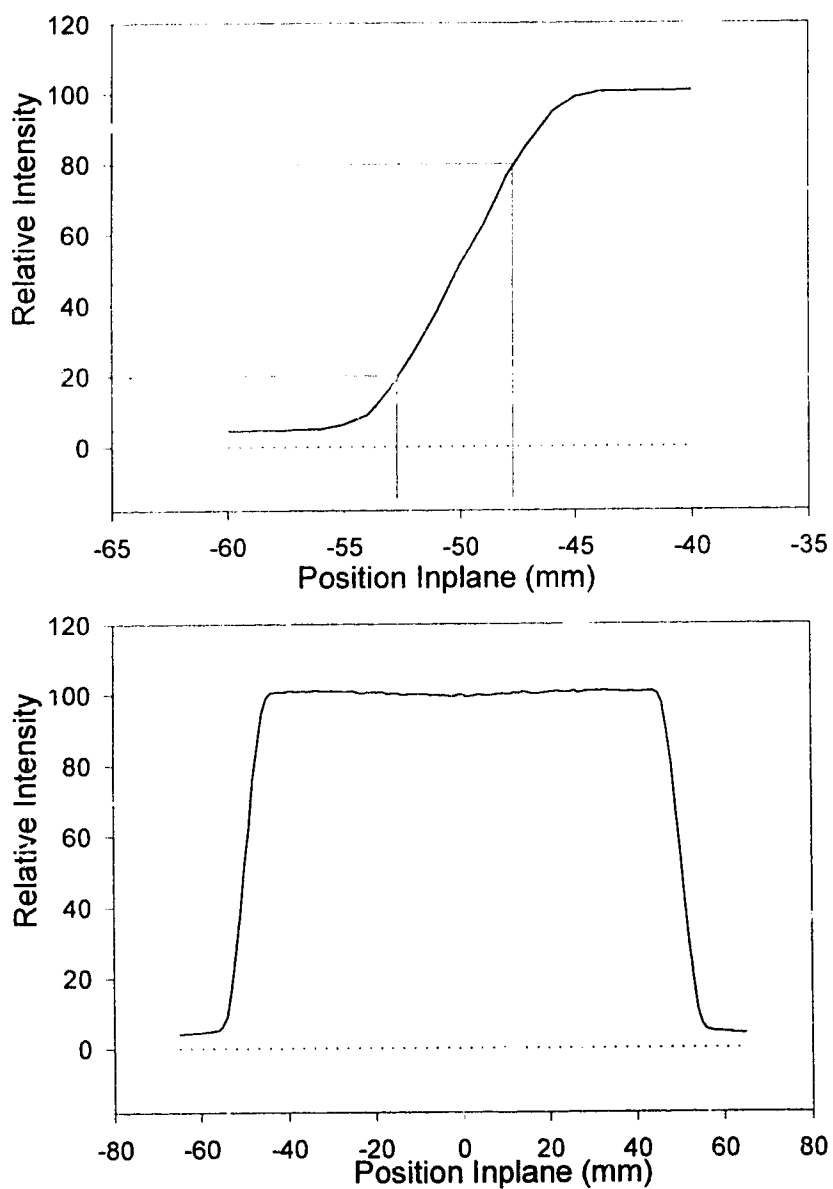


Figure 3.12 Penumbra for a  $10 \times 10 \text{ cm}^2$  field, 100 cm SAD (6MV beam, Varian 2300C'D, diode).

### 3.3.3.1 Modelling of Penumbra

A number of simplifying assumptions may be made in order to ease the calculation of the penumbra. Relaxing many of these assumptions allows progression toward a more realistic description of the physical penumbra, as will be shown.

The following assumptions may be made:

- 1) the source may be blocked by the jaw's bottom, top or by both edges (this depends on the assumed geometry)
- 2) a single or multiple source model may be employed
- 3) the geometry of the source(s) may be viewed as square, circular or some other geometry
- 4) the source strength may be considered as homogeneous or inhomogeneous
- 5) the source strength may vary in either a symmetric or asymmetric fashion
- 6) the transmission through the jaws may, or may not, be ignored
- 7) the head scatter may, or may not, be ignored

In calculating the fluence profile of an open field, one may make use of a simple geometric formula [Johns and Cunningham 1983] to model the penumbra. In the calculation of this geometric penumbra, a number of assumptions are made. These include assumptions regarding the radiation source (it is of some finite width), its intensity distribution (it is uniform), and the way radiation propagates to the region below the collimating jaws giving rise to the field penumbra (collimation is perfect). It is also assumed that all the field blocking is from the bottom of the jaws. The geometric penumbra width, from 0 to 100%, may be calculated using similar triangles as

$$\text{pen.} = (W_{\text{source}}) \frac{(\text{SAD} - \text{SJD})}{\text{SJD}} \quad [3.12]$$

where SAD is the Source to Axis Distance, SJD is the Source to Jaw Distance, ' $W_{\text{source}}$ ' is the width of the source and 'pen.' is the width of the penumbra (which one can verify by similar triangles; cf. figure 3.13). Defining the points along the measurement axis that mark the beginning and end of the penumbra as  $x_{100}$  and  $x_0$ , and if  $x_{100} < x_0$ , then, by considering the extent of the source which can be 'seen' below the collimating jaws, the field intensity at any given point  $x$  in the penumbra is given by

$$I = I_0 \left( \frac{x - x_{100}}{x_0 - x_{100}} \right) \quad [3.13]$$

according to a simple linear interpolation within the penumbral region from the 100% point to the zero point.

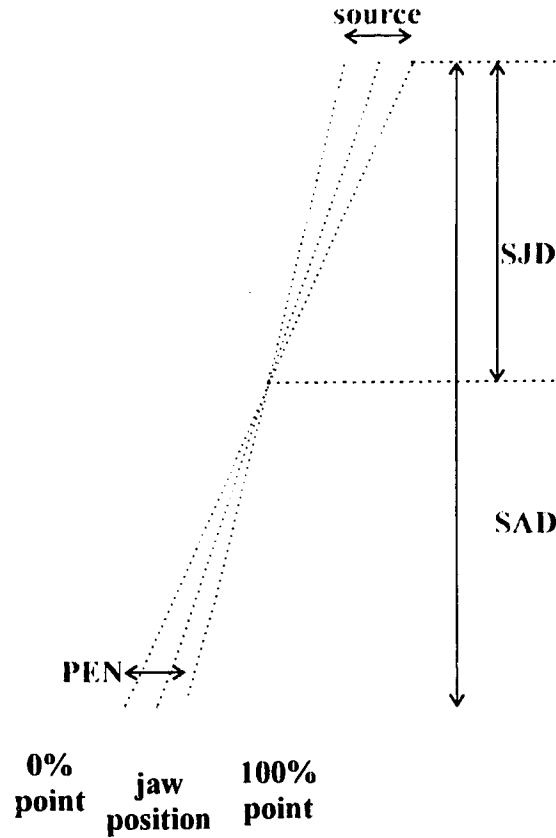


Figure 3.13 Simple geometric model for the penumbra.

Johns and Cunningham [1983] also propose an empirical fit to the penumbral region using a bi-exponential function, which depends on whether or not the point of interest,  $x$ , lies above or below the midpoint of the penumbra (the 50% point,  $x_{50}$ ). It is expressed as

For  $\text{abs}(x) < \text{abs}(x_{50})$ ,

$$\psi(x) = \psi_0(x) \cdot (1 - 0.5 \cdot \exp^{-\alpha_1 \cdot \text{abs}(x_{50} - x)}) \quad [3.14]$$

For  $\text{abs}(x) > \text{abs}(x_{50})$ ,

$$\psi(x) = \psi_0(x) \cdot (t + (0.5 - t)) \cdot \exp^{-\alpha_2 \cdot \text{abs}(x - x_{50})} \quad [3.15]$$

where  $\alpha_1$  and  $\alpha_2$  are empirically determined constants,  $t$  represents the amount of radiation transmitted through the jaw, and  $\psi_0$  is the fluence that would be seen at  $x$  if there was no collimator present. This provides only an approximate fit, and has little physical basis.

It seems reasonable to retain the assumption regarding the symmetry of the source, and it seems very reasonable to assume a circular symmetry for the source instead of a square symmetry given that the measured primary fluence below the jaws is radially symmetric. Some other assumptions of this model may be relaxed such as the assumption that the geometry of the situation is measured with the bottom of the jaw doing the blocking of the field. Hence we will assume that the field blocking is done both by the top and bottom of the jaws, and call this the extended geometric model (see figure 3.14).

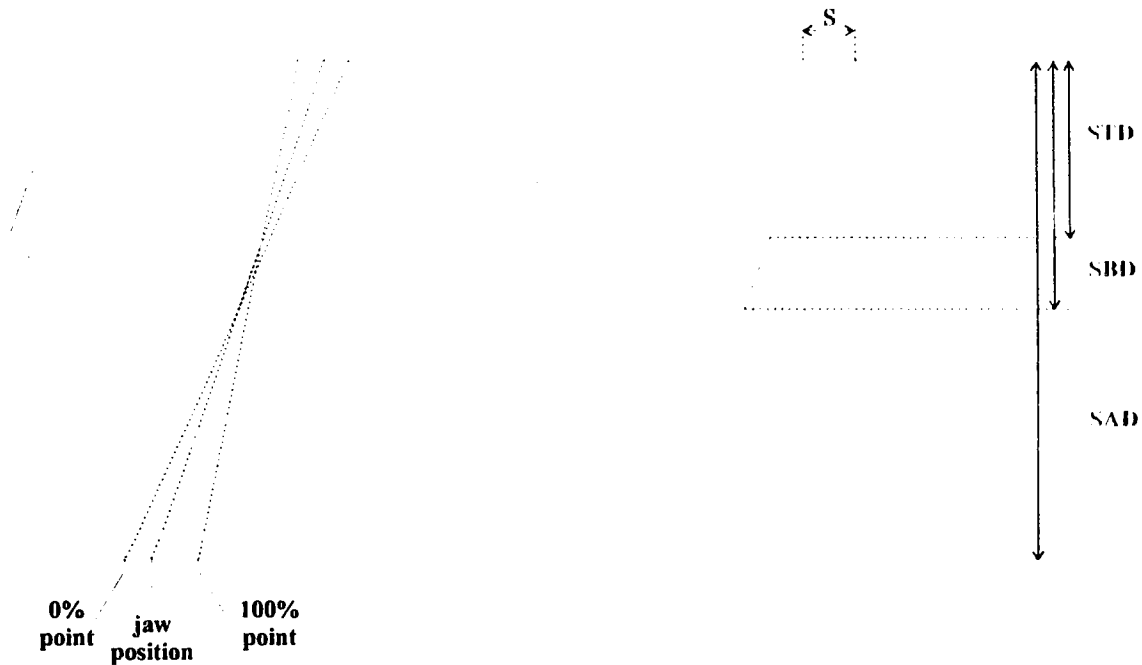


Figure 3.14 Extended geometric model for the penumbra.

Assuming, for a homogeneous source, that the fluence  $\psi(x)$  to any given point is proportional to the area of the source which can be 'seen' at that point; one has

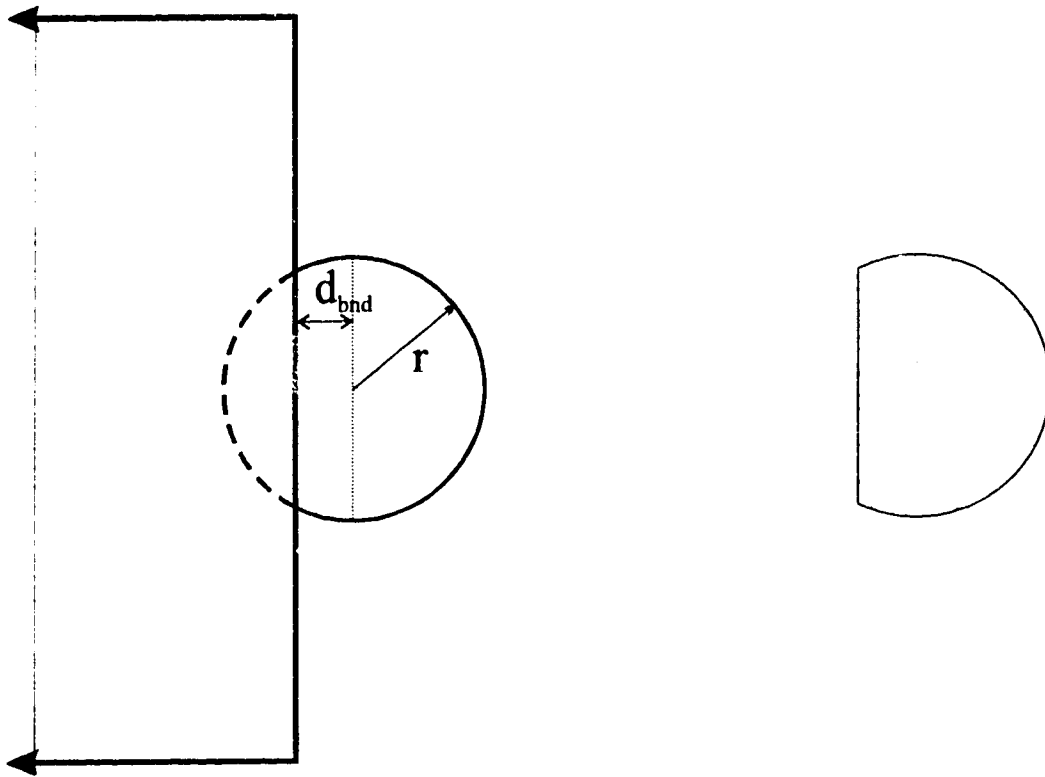


Figure 3.15 The geometry of the x-ray source.

$$\Psi(x) \propto \text{area} \Rightarrow \Psi(x) = \Psi_{\text{primary}}(x_{50}) \frac{\text{Area}}{\text{max. Area}}$$

or, for a circular source,

$$\Psi(x) = \Psi_{\text{primary}}(x_{50}) \frac{\text{Area}}{\pi r^2} \quad [3.16]$$

where  $\Psi_{\text{primary}}$  is the primary fluence at  $x_{50}$ , the fifty percent point of the penumbra ( $x_{50}$  occurs where the jaw position is set for 100 SSD);  $r$  is the radius of the circular source.

The boundaries of the geometric penumbra occur at positions  $d_0$  and  $d_{100}$  in the plane through isocentre and normal to the CAX, hereafter called the measurement plane. These values, which are relative to the settings for the jaw position, are given by



$$x_0 = x_{50} + \frac{1}{2}s \frac{(SAD - SBD)}{SBD} \quad [3.17]$$

for the  $\Psi=0\%$  to  $50\%$  region and

$$x_{100} = x_{50} - \frac{1}{2}s \frac{(SAD - STD)}{STD} \quad [3.18]$$

for the  $\Psi=50\%$  to  $100\%$  region, where STD is the distance from the source to the top of the jaw, SBD is source to bottom of jaw distance, and SAD is the source to axis distance. The constant 's' denotes the width of the source.

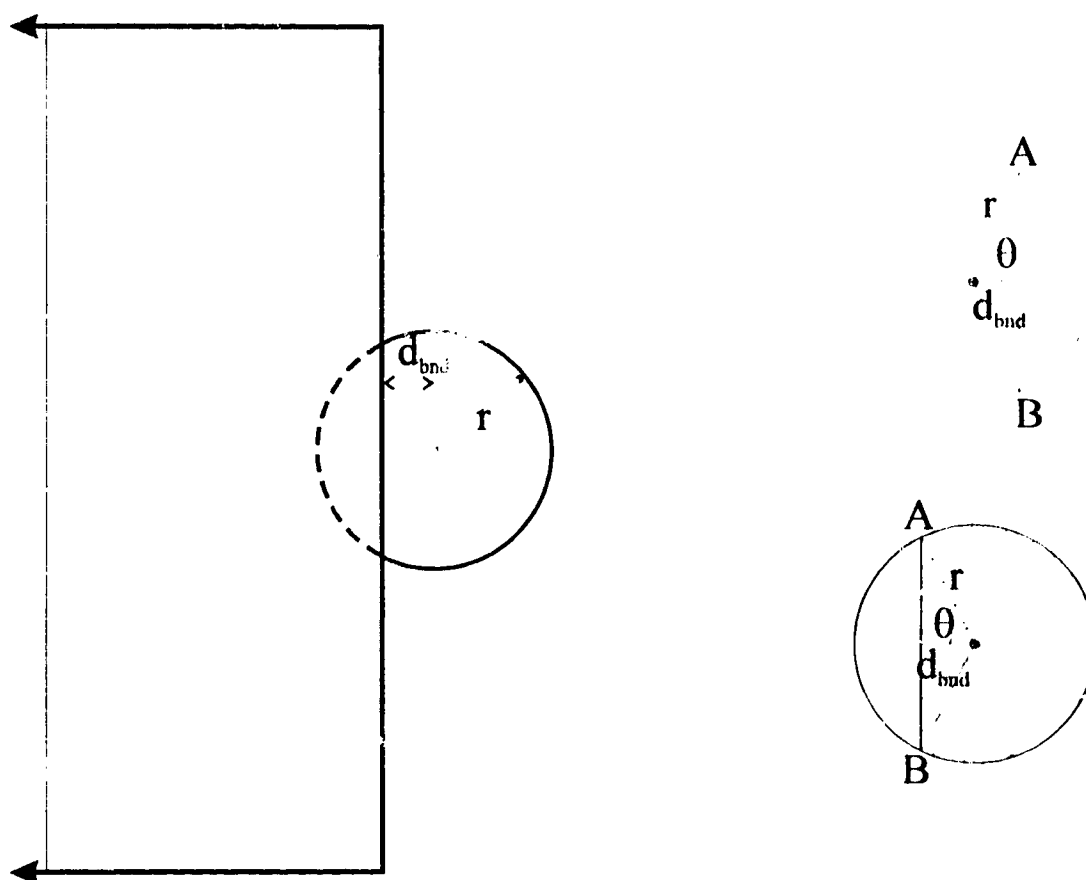


Figure 3.16 Calculating the amount of the x-ray source which is visible.

In order to discuss the variation in the amount of source visible to a point on the measurement plane, a few terms must be defined. Let the distance from the centre of the visible source to the edge of the visible region (the boundary) be  $d_{\text{bnd}}$  and the source radius be some value  $r=s/2$  (see figure 3.15). Given this arrangement, one may calculate the area visible from the measurement plane (the cross hatched area at right in figure 3.15). This may be done by calculating the angle  $\theta$  between the radius and a line of length  $d_{\text{bnd}}$  normal to the jaw, extending from the centre of the circle to the jaw (see figure 3.16).

One may derive two expressions for the area of the source which is visible; the first for the case where more than 50% is visible, and the second for the case when less than half is visible. For the cross hatched section of the circles pictured in figure 3.16, let the area of the source that is visible be denoted  $A_s$ . It can then be stated that

$$A_s = \frac{1}{2} r^2 (2\theta - \sin 2\theta) \quad [3.19]$$

where the term  $2\theta$  results from the definition of  $\theta$  as subtending half of the line A-B.

Proceeding, one may determine the value for  $\theta$ . For the case where less than half the source can be seen, one has

$$\theta = \cos^{-1} \left( \frac{d_{\text{bnd}}}{r} \right) \quad [3.20]$$

and thus

$$A_s = \frac{1}{2} r^2 \left( 2 \cos^{-1} \left( \frac{d_{\text{bnd}}}{r} \right) - \sin \left( 2 \cos^{-1} \left( \frac{d_{\text{bnd}}}{r} \right) \right) \right) \quad [3.21]$$

Similarly, for the other case where more than half the source is visible, the expression is

$$A_s = \pi r^2 - \frac{1}{2} r^2 \left( 2 \cos^{-1} \left( \frac{d_{\text{bnd}}}{r} \right) - \sin \left( 2 \cos^{-1} \left( \frac{d_{\text{bnd}}}{r} \right) \right) \right) \quad [3.22]$$

Thus, once the value of  $d_{\text{bnd}}$  is determined, the visible areas may be calculated. Looking at figure 3.14, and assuming a point of interest  $x$ , where  $d_0 > x > d_{100}$  (as per the earlier definition), then, by similar triangles, for a point between the 0 and 50% point, one has

$$d_{\text{bnd}} = \frac{\text{sbd} (\text{abs}(x - d_{50}))}{(\text{sad} - \text{sbd})} \quad [3.23]$$

and for points  $x$  between the 50% and 100%

$$d_{\text{bnd}} = \frac{\text{std}(\text{abs}(x - d_{50}))}{(\text{sad} - \text{std})} \quad [3.24]$$

A further refinement to the penumbral model may be made if the assumption of a homogeneous intensity distribution within the source is relaxed. Various investigations [Jaffray *et. al.* 1993; Loewenthal *et. al.* 1993; Lutz *et. al.* 1988] of the intensity and distribution of the x-rays from the target have found that the effective source distribution for the target is Gaussian and roughly symmetric, with a FWHM value of about 1.4 mm (giving  $\sigma = 0.6$  mm) for a Varian 6 MV beam. In particular, one investigation [Jaffray *et. al.* 1993] suggests that a dual source model best described the radiation distribution, with most of the radiation (about 95% for a  $10 \times 10$  cm<sup>2</sup> field) originating from a focal spot with the aforementioned standard deviation, and the rest resulting from a broadly distributed Gaussian extra-focal source with a  $\sigma$  of roughly 10 mm.

Using these values for a 6MV beam,  $10 \times 10$  cm<sup>2</sup> field, for the distributions of the focal and extra focal radiation,  $\sigma_f$  and  $\sigma_{\text{ef}}$ , as well as for their relative weightings,  $\text{wt}_f$  and  $\text{wt}_{\text{ef}}$ , one can define an expression for the penumbral intensity. Again, given a value  $d_{\text{bnd}}$ ,

$$\text{Pen. Wt.} = (\text{wt}_f) e^{-\left(\frac{x^2 + y^2}{2\sigma_f^2}\right)} + (\text{wt}_{\text{ef}}) e^{-\left(\frac{x^2 + y^2}{2\sigma_{\text{ef}}^2}\right)} \quad [3.25]$$

which is the weighting for the calculation of the penumbra. Assuming that the area of the source varies only along one dimension (say along the  $x$  direction), then one has

$$\begin{aligned}
\int e^{-\left(\frac{x^2+y^2}{2\sigma_f^2}\right)} &= \int e^{-\left(\frac{x^2}{2\sigma_f^2}\right)} \int e^{-\left(\frac{y^2}{2\sigma_f^2}\right)} \\
&= \int e^{-\left(\frac{x^2}{2\sigma_f^2}\right)} \int_{-\infty}^{\infty} e^{-\left(\frac{y^2}{2\sigma_f^2}\right)} \\
&= \frac{1}{\sigma_f \sqrt{2\pi}} \int e^{-\left(\frac{x^2}{2\sigma_f^2}\right)}
\end{aligned} \tag{3.26}$$

and the same derivation applies to the extra focal component.

### 3.4 Dose Calculation

In order to arrive at the fluence required to deliver a desired dose profile in phantom, a means of calculating the dose distribution of a given fluence profile must be available. Given such a dose calculation technique, it is possible to iteratively arrive at a solution for a required fluence profile.

There are a number of techniques that can be used for the calculation of dose profiles, from semi-empirical methods such as differential scatter air ratio integration (dSAR), to more complex first-principles techniques such as Monte Carlo algorithms and convolution algorithms.

#### 3.4.1 Calculation Technique

A dSAR dose calculation technique was employed in this study. In order to calculate the dSAR values, the SAR values from a particular linear accelerator were first determined for a particular energy, and for various field sizes and various depths. Recall that the SAR(f.s.,d) is a ratio of the contribution of scatter in a medium to the dose in free space. It can be calculated knowing the TAR and TAR0 values for a particular geometry, since SAR(f.s.,d)=TAR(f.s.,d)-TAR0 (cf. section 2.4.1.3).

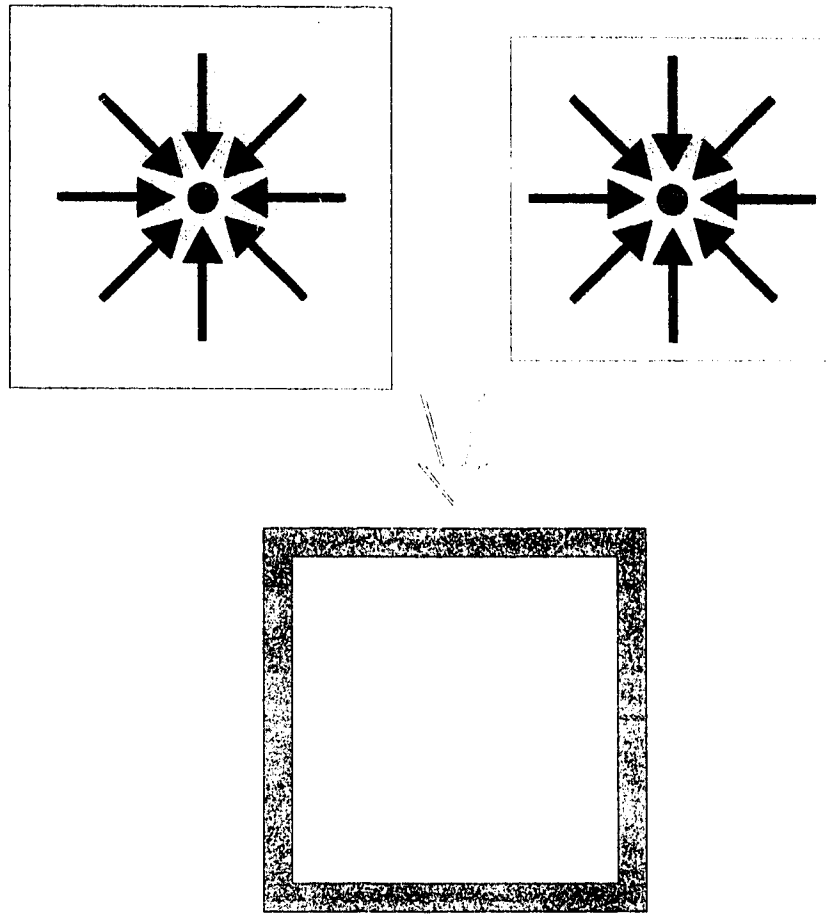


*Figure 3.17 Calculation of a dSAR value.*

The SAR values used for this work were collected by another research project [Kollar 1996] at the CCI. The SAR values were measured for various square field sizes which were symmetric about the CAX, and for multiple depths. In order to obtain the scatter contribution from a particular region, the scatter from a square field can be subtracted from the scatter from a larger square field. This leaves the scatter contribution from the peripheral square region (see figure 3.17); this is referred to as a dSAR value. It is possible to relate this square region to an equivalent circular region of radius  $r$  (see figure 3.18). Using these equivalent circular regions it is possible to generate an array of SAR( $r$ ) values for discrete values of  $r$ , for various depths.

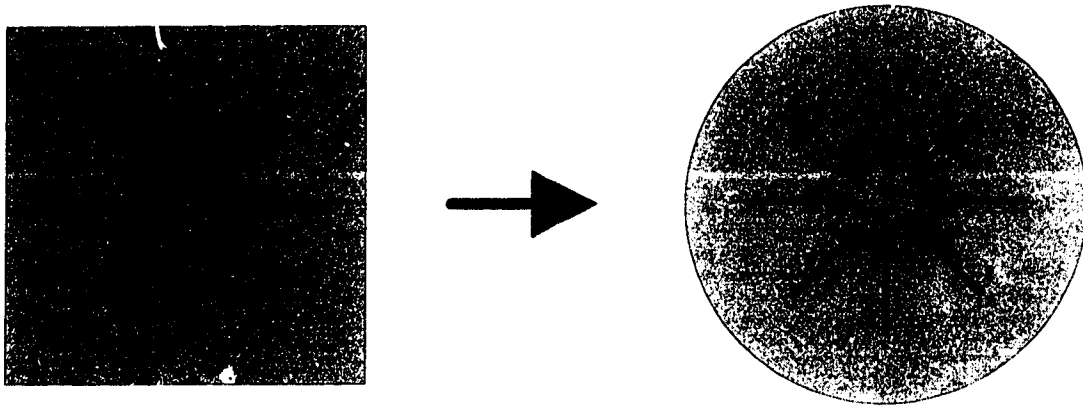


*Figure 3.18 Equivalent circular field calculation*

SAR values for intermediate radii to those measured were obtained by linear interpolation. Denoting the desired radius at which an SAR value is needed as  $r$ , and the measured radius which is just larger as  $r_+$ , and the first value which is just smaller as  $r_-$ , thus

$$\text{SAR}(r) = \text{SAR}(r_-) + \frac{\text{SAR}(r_+) - \text{SAR}(r_-)}{r_+ - r_-} (r - r_-) \quad [3.27]$$

The circular dSAR values can now be calculated for annular rings by subtracting the SAR for a field of radius  $r$  from the SAR for a field of larger radius  $r'$  (see figure 3.19). This annular dSAR cone, assuming it is radially symmetric, is then broken into dSAR 'pencils' of width  $\Delta\theta$  by dividing the contribution from the cone by some value  $n$ , where

$$n = \frac{2\pi}{\Delta\theta} \quad [3.28]$$

The dSAR pencils can then be used to calculate the contribution from slab-like regions. Consider a dSAR pencil at distance  $r_{pt}$  (left, figure 3.20), which contributes scattered radiation to the point on the CAX. This can be equated with the contribution from a pencil at a distance  $r_{pt}$  to a point not on the CAX. In order to do

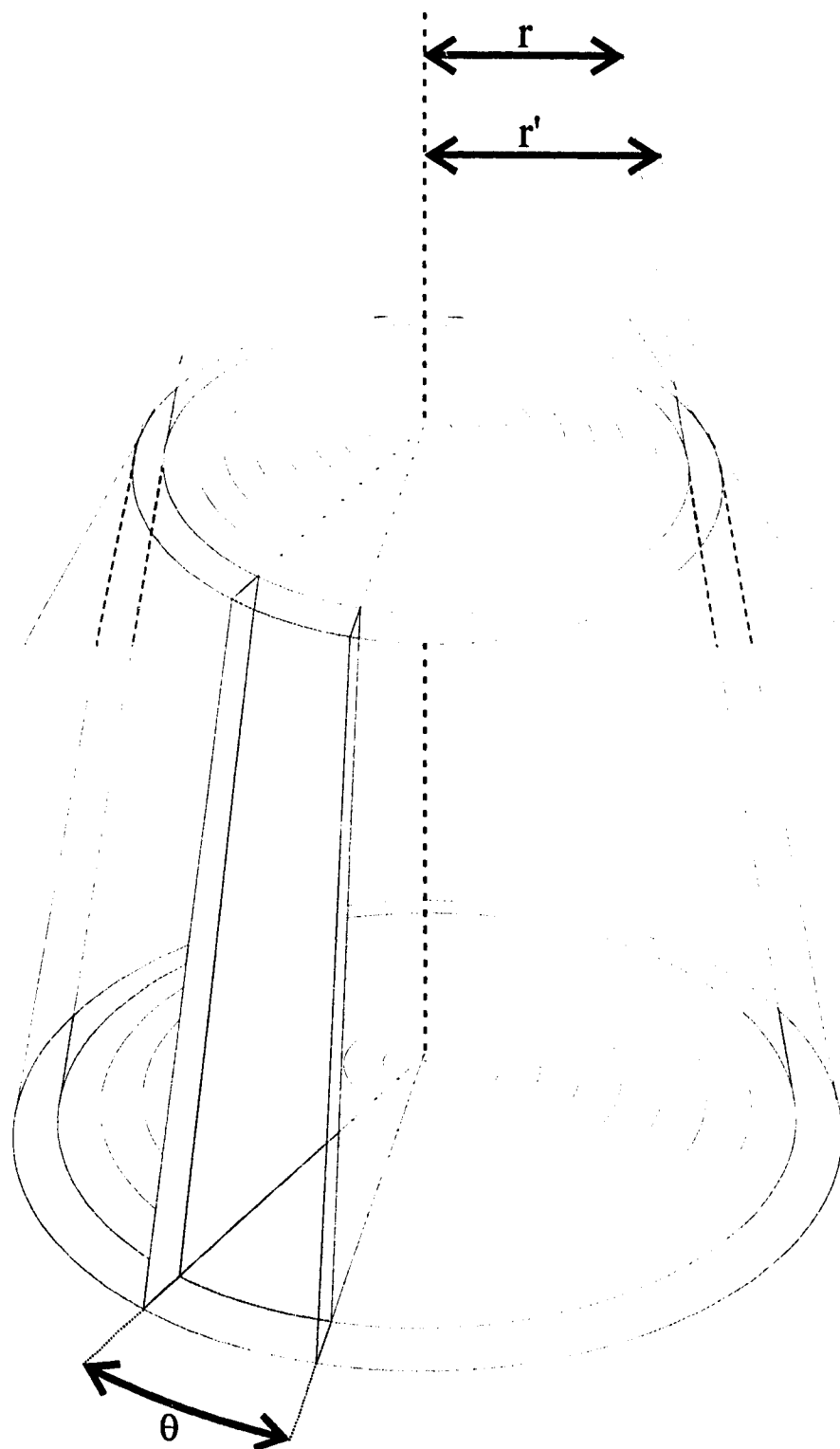


Figure 3.19 Calculating a dSAR pencil of width  $\theta$ , using  $SAR(r)$  and  $SAR(r')$ .

this, the pencil value is corrected for the AOF that would have affected the original value for the pencil at a distance  $r_{pt}$  from the CAX. The true AOF for the pencil can then be accounted for based on its actual distance from the CAX,  $r_{CAX}$  (see figure 3.20, centre).

Calculating the scatter contribution from a slab-like region (figure 3.20, right) to a point of interest starts by choosing a spacing/thickness for the slabs. Once this is done, the slab is approximated by a series of pencils for gradually incremented values of  $\theta$  between varying distances  $r$  and  $r+\Delta r$  from the point of interest. The contribution from the pencils within the slab, after making the AOF corrections to pencils, are summed. If a small enough value of  $\Delta\theta$  is chosen, the value of which determines both the thickness of the pencil and the number of pencils used (by specifying by how much the value of  $\theta$  is incremented), a good approximation to a slab can be arrived at.

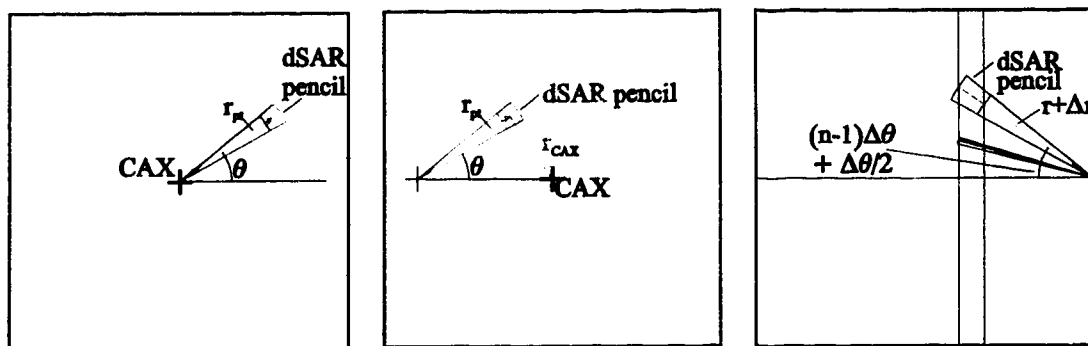
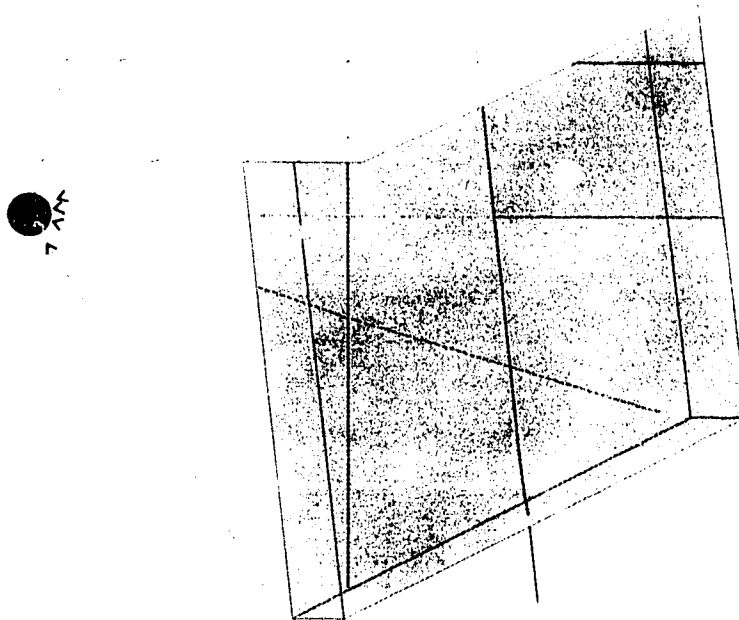


Figure 3.20 Calculation of the scatter contribution from slabs.

For calculation purposes, the slabs one requires are easily determined since they are symmetric about the inplane or crossplane axes, and a flat phantom surface is assumed. The technique used to calculate the dose to any point in the phantom is to use the measured SAR data to derive dSAR data. This dSAR data are then used to calculate the pencil contributions, which in turn are used to calculate the contribution from the slabs. The slabs are multiplied by their respective relative fluence at that point, and these values are summed and added to the primary contribution to the point of interest using the TAR0 (see figure 3.21).



$$\Phi(x) \quad CAX \quad \Phi(x_i)$$



$$D(x,d)=\Phi(x)\text{TAR}(0,d)+\Sigma(d\text{SAR}_{\text{slab}})(\Phi(x_i))$$

*calculating dose using slabs constructed with dSAR pencils.*

to any given point in the dynamic application is given by:

$$\left( \sum_{i=1}^N \left[ \sum_{j=1}^n \frac{\text{SAR}(r_j + \Delta r_j) - \text{SAR}(r_j)}{\Phi_{\text{open}}(r_{\text{CP}})} \Delta\theta \right] \Phi_{\text{open}}(r_{\text{CAX}}) \Phi_{\text{dyn}}(x_i) \right) \quad [3.29]$$

$$+ \text{TAR}(\cdot, d) \Phi_{\text{dyn}}(x)$$

where  $N$  is the number of slabs,  $n$  is the number of pencils defining a slab,  $\Phi_{\text{open}}(x)$  is the relative energy fluence one would expect from an open field at the point in

question, and  $\Phi_{dyn}(x)$  is the relative energy fluence expected at the given point from the dynamic field. The radii are calculated as

$$r_j = \frac{x}{\cos[(j-1)(\Delta\theta) + \Delta\theta / 2]},$$

$$\Delta r_j = \frac{\Delta x}{\cos[(j-1)(\Delta\theta) + \Delta\theta / 2]}, \quad [3.30]$$

$$r_{CP} = r_j + \Delta r_j / 2$$

Again,  $r_{AX}$  is the distance to the centre of the dSAR pencil from the central axis, and  $r_{CP}$  is the distance to the pencil centre from the calculation point at  $x$  (see figure 3.22).

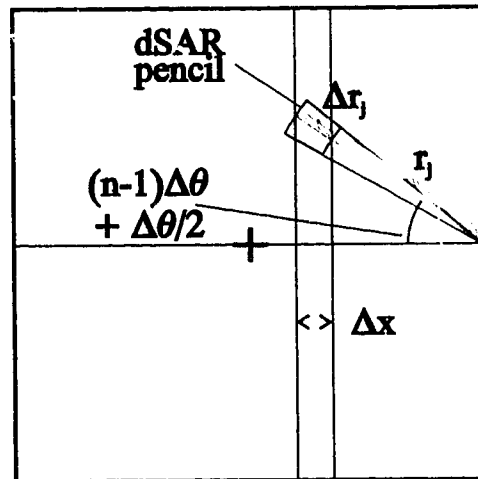


Figure 3.22 The values of  $r_j$  and  $\Delta r_j$  in the calculation of the scatter slab.

### 3.4.2 Evaluation of Dose Algorithm

The dose algorithm was tested for a number of  $10 \times 10 \text{ cm}^2$  fields. Based on an input fluence profile, and using the dSAR technique outlined above, a resultant dose profile was calculated. The results compare favourably with measured dose profiles (see figure 3.23), with a slight discrepancy at the field edge. This may be due to loss of lateral electronic equilibrium in the measurement of the dose profile.

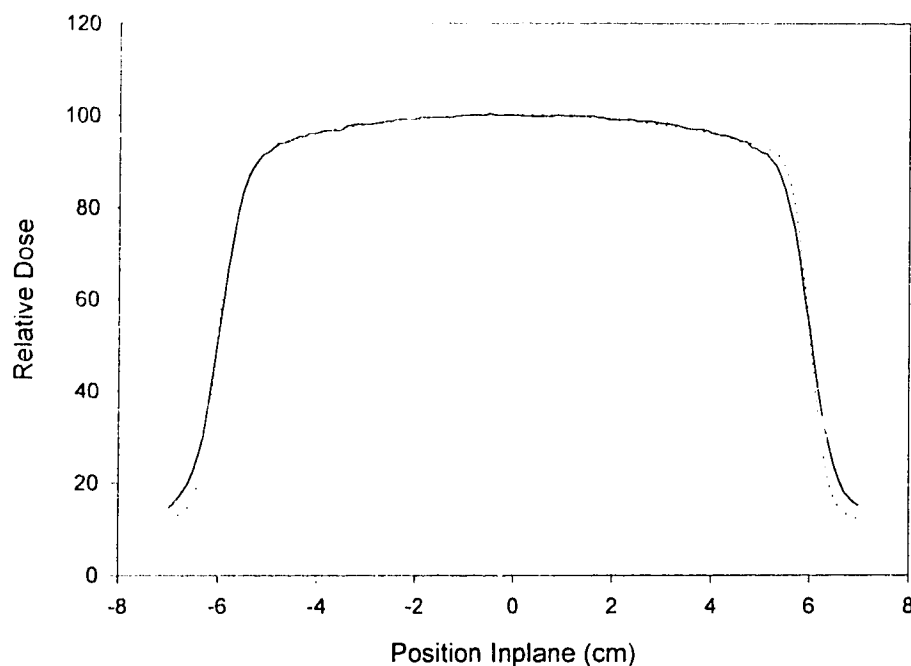


Figure 3.23 Comparison of dose distribution calculated using a dSAR technique (dotted) and a measurement of the same profile,  $10 \times 10 \text{ cm}^2$  field, 20 cm depth (6MV beam, Varian 2300CD, ion chamber).

### 3.4.3 Iterative Correction

In this work, an iterative method is employed to determine the energy fluence profile required to generate a desired dose profile by making an initial guess at the fluence profile from which the resulting dose profile is calculated. Once this is done, the resulting dose profile is compared to the desired profile, and the original fluence profile is modified, by increasing the fluence delivered to the regions that were underdosed, and decreasing the fluence profile where the resulting dose profile was overdosed. This is similar to the approach taken by Kijewski et. al. [Kijewski et. al. 1978] for the calculation of dynamic wedge dose profiles; cf. 3.2.1.

## 3.5 Dynamic Field Verification

In order to verify the results of these calculations and to justify the various corrections made to the field, one must be able to accurately and reproducibly assess

the relative fluence or dose delivered during a dynamic treatment. This requires both predictors and dosimeters which are capable of handling dynamic treatments.

If a fluence or dose delivery proceeds as planned, then the prediction of the result of any treatment is straightforward, as it should be equal to the desired dose/fluence. If the signal from the dosimeter is not equal to the true dose or if the device used to measure the relative energy fluence does not directly yield a true signal, then this should be taken into account when comparing measured data to predicted data.

A good dosimeter for dynamic fields must be capable of measuring the integral dose from a dynamic profile, given the temporally varying nature of the dynamic field. The dosimeter should, as well, be able to do so in a reasonable amount of time (single ion chamber point measurements would take a prohibitively long time to map a dynamic field with good spatial resolution).

### 3.5.1 Comparisons

For any given measurement, it is desirable to compare the results to predicted values. The predicted values may be some initial desired input value (i.e. the dose profile measured should be equal to the dose profile entered as input), or may require some computation (due to some distortion by the measurement device, as discussed below).

#### 3.5.1.1 Predicted Fluence

Ideally, it is desired that the measured fluence profile be equal to the actual fluence profile produced. This would be the case if it were possible to measure the true relative energy fluence profile without distortion, but this would require a point detector that is insensitive to electron contamination in the beam.

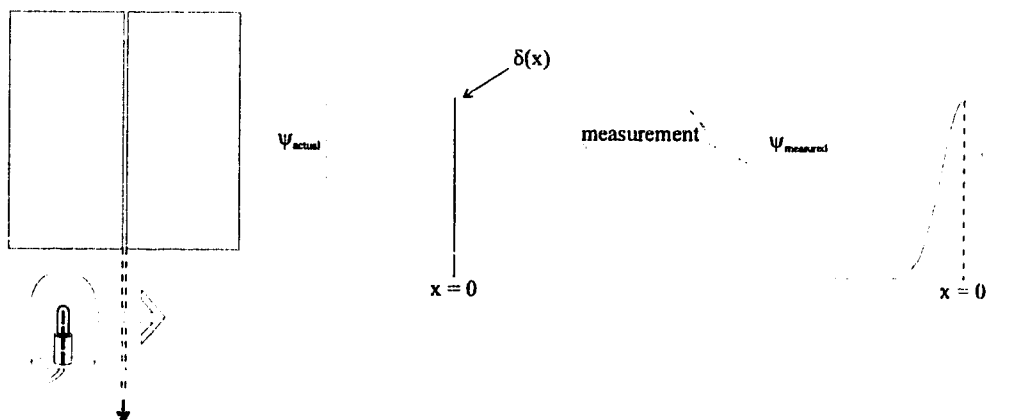


Figure 3.24 Probe response function measured by scanning thin ( $\delta$  function) beam.

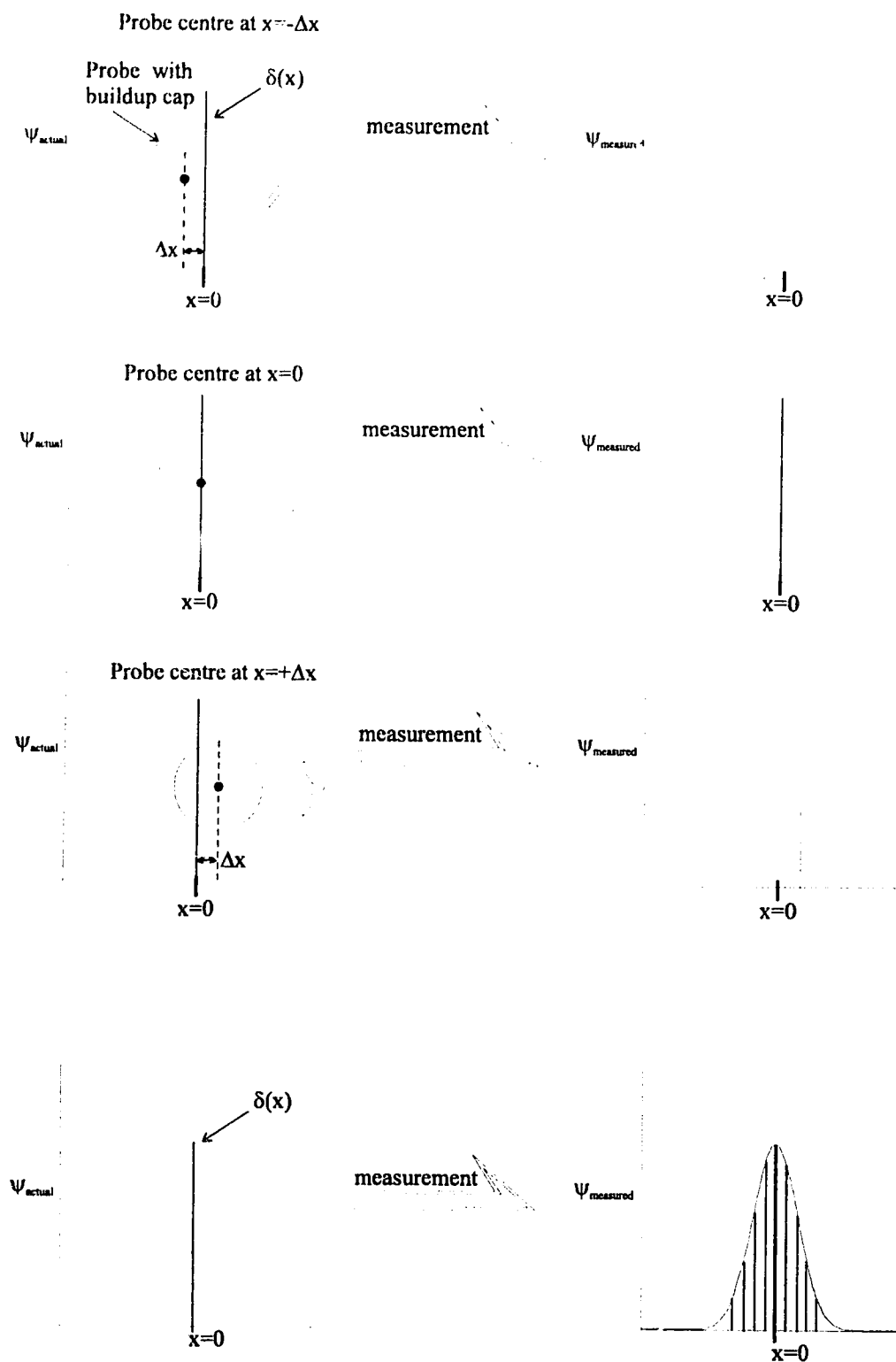
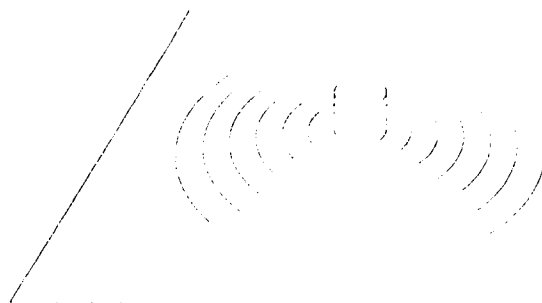


Figure 3.25 Probe response function, using integrated point measurements.

Measurements were made in air with a suitable amount of buildup material in order to screen out contaminant electrons and, in the case of ion chambers, provide electronic equilibrium. The practical limitation on the measurements is therefore the buildup cap, which tends to smear out the recorded signal; as an example, a cap being either scanned across a thin  $\delta$  function-like beam (see figure 3.24) or translated step wise across, taking integral measurements (see figure 3.25), would register some sort of a broad signal. This signal could, in principle, be deconvolved with a response function, which would be characteristic of the buildup cap and the dosimeter, to give the signal that would be recorded by a point detector. This, however, does not prove to be practically feasible due to the comparably large amount of noise (large for the purposes of deconvolution) that was present in the measurement of the response function.

For fluence profiles which were measured with film, a minimum amount of buildup material was placed over the film. This was in order to eliminate any electron contamination in the beam. As well, a thick (20 cm) slab of Styrofoam was placed beneath the film in order to reduce backscatter. An attempt to measure the effect of the scatter from the buildup layer on the measurements was made. This was done by measuring the affect for numerous readings of the OD on the CAX, given equal MU and field size settings, and with buildup discs of increasing size (see figure 3.26). These differential OD (dOD) values give a measure of how low energy scatter from increasing distances affects the final OD value at a measurement point. These values can be used to arrive at a set of differential scatter data which can be used to calculate the effect of scatter on a film reading, effectively allowing one to predict what a measurement should look like, given an actual fluence value. This is to say that the ideal value for the fluence is 'smeared' using the dOD values, and this is then compared to the film measurements.



*Figure 3.26 Measurement of the effect of buildup on fluence measured with film.*

### 3.5.1.2 Dose Profiles Using ATP

The in-house treatment planning system at the Cross Cancer Institute, ATP, has been outfitted with a subroutine which calculates the resultant isodose lines given an input file in Varian segmented treatment table (STT) format. This is done on the principle that the STT file is directly related to the relative energy fluence profile for a specified x-ray beam. This allows for a prediction of isodose distributions based on a generated dynamic beam delivery schedule. This feature has been tested by comparing the predicted isodose values with the values measured using a linear ion chamber array.

## 3.5.2 Beam Measurements

As has already been mentioned, an integrating dosimeter is needed in order to evaluate the performance of any dynamic techniques. The dosimetry techniques used in these studies were chiefly of two types: film measurements and ion chamber array measurements. Some use was also made of single ion chamber (point measurements and profile scans of non-dynamic fields) and diode measurements.

The Wellhöfer<sup>TM2</sup> water tank scanning system was used extensively in these investigations, in conjunction with the single ion chamber, diode and ion chamber array. This tank is a 48 cm by 48 cm by 48 cm acrylic plastic tank which can be rotated and translated, and filled with water for use as a water phantom, or emptied to measure in-air profiles. It is capable of  $\pm 0.1$  mm precision in positioning.

### 3.5.2.1 Fluence Measurements

Although a point detector is required in order to truly measure fluence, one may attempt to take measurements which are as close to being point measurements as possible. This means using a minimum amount of buildup, with a suitable small active measurement volume.

#### 3.5.2.1.1 Film

For any given set of films, a number of calibration exposures must be performed to allow the correlation of optical density to relative intensity. The set-up used for the exposure of both the calibration and evaluation films is kept as identical as possible, films are taken from the same batch and are processed at roughly the same time. All this is done to minimise any errors due to the calibration film's exposure or processing conditions being different from that of the films used for evaluation of the dynamic fields.

---

<sup>2</sup> Wellhöfer Dosimetrie, Nürnberg, Germany

The film used in these investigations was Kodak<sup>3</sup> X-OMAT XV2 diagnostic film. Films were exposed with a 1.5 cm polystyrene buildup plate to screen out contaminant electrons in the beam. They were set at 100 SSD and rested on about 20 cm styrofoam to minimise backscatter onto the film. The film processing was done with a Kodak X-OMAT 270 RA Processor, and all readings were taken with a Wellhöfer™ WP102 film scanning densitometer system.

### **3.5.2.1.2 Diode**

The peculiarities of diodes and diode measurements were laid out in section 2.4.3. The diode's small active volume is of use when evaluating fluence measurements as it approaches an ideal point detector. With a small buildup cap made of brass, scans were taken in air with a Therados GR p-type silicon semiconductor detector (0.3 mm<sup>3</sup> active volume, 0.5 mm below surface of diode, casing roughly 7 mm in diameter). This was assumed to be a reasonably good approximation to the relative fluence.

The brass buildup cap allows for the use of a much thinner layer for screening out electrons, since it has a higher effective Z than the acrylic caps normally used. The thinner cap exposes the dosimeter to a smaller area of the beam, and slightly limits the scattering of photons into the detector.

### **3.5.2.1.3 Ion Chamber**

The use of the ion chamber for the evaluation of radiation fields is commonplace. This is mostly due to the reliability and reproducibility of such measurements, as well as its ability to convert measurements to absolute dose. The ion chamber used in these investigations was the Wellhöfer™ IC10 ion chamber.

The chief drawback in the use of the ion chamber for evaluation of a dynamic field is its inability to do rapid integrated measurements of temporally variant fields. It is possible to collect data for a single point, and move the ion chamber to collect data from other points, but this becomes quite time consuming if good spatial resolution of the field is desired. Furthermore, if a summation of static fields is being used to simulate a dynamic treatment, where an individual dynamic field can take on the order of twenty minutes to produce, then measurement time becomes unacceptably large. As well, charge leakage from the electrometer has the potential to render this park and measure technique unacceptable for dynamic simulations. Another drawback of the ion chamber is that it requires electronic equilibrium in order to give meaningful data (making data taken at field edges and near the phantom surface somewhat suspect).

---

<sup>3</sup> Eastman Kodak Company, Rochester, New York



#### 3.5.2.1.4 Ion Chamber Array

A line ion chamber array (Wellhöfer™ CA24), with 23 ion chambers (0.4 mm thick walls) with a 2cm spacing between chambers, in conjunction with the Wellhöfer™ MD240 multichannel electrometer, was used extensively for park and measure data acquisition. The ion chamber array allows for (relatively) fast acquisition of point measurement profiles of dynamic fields, but it is only truly practical for measurements of true dynamic fields as opposed to dynamic fields that are simulated with summed static fields. This is due to the charge leakage which may occur during the long production times for summed static fields.

The ion chamber array has been outfitted with a number of brass buildup caps in order to allow for the collection of relative fluence profiles, as per the assumption laid out in 3.5.2.1.2, as well as an acrylic cap.

#### 3.5.2.2 Dose Measurements

Many of the considerations for the measurement of dose are the same as for the measurement of fluence, most notably the requirement that, for dynamic fields, the dosimeter be able to handle time integrated fields.

##### 3.5.2.2.1 Film

The utility of film in the study of dynamic fields has been widely noted [Leavitt 1990b; 1994a,b,c], mostly due to the speed with which film can be used, its relative ease of use, and the efficiency with which it collects time integrated dosimetric information. The difficulties associated with using film for photon dosimetry are also well documented [Anderson 1979; Williamson 1981; Hale 1994; Leavitt 1994b,c], but it is possible to achieve reasonable results using film dosimetry, through proper calibration techniques (within 2 or 3 % of the ion chamber values [Williamson 1981; Hale 1994]). The methods currently being used are similar to those put forward by Hale *et. al.* [1994] for calculating the appropriate curves for the O.D. (optical density) to dose conversions (the paper cites better results than those for the Williamson technique, and without recourse to the more complex method of calculating correction factors). Several films of the same field size as those to be converted are exposed parallel to the beam, in arbitrary 20 MU increments (from, say, 20 to 140 MU). These films will give a depth specific conversion function for profiles. For the conversion of isodoses measured from film for dynamic fields, a variant on a technique suggested by [Leavitt 1994c] was employed, which assumes an optical density to dose conversion function that varies by some factor between depths.

The calibration of the film is based on the H and D curve response of the film. Within a certain region, the response of the film to increasing dose is roughly linear (notwithstanding energy degraded photons). It is therefore possible to construct a

curve of optical density versus dose based on films exposed to fields producing known doses to the medium, and therefore to particular points on the film.

In order to achieve maximum reproducibility with the film, all films are processed at the same time (i.e. the same night, all within two or three hours of each other), and a set of calibration films is taken at the same time. As well, all films are taken from the same batch of film. This is done because the accuracy of the film dosimetry drops for films processed separately, and also for films taken from different batches instead of from the same batch. For each film, a small portion is cut off and processed, unexposed, for a background fog reference. The films themselves are encased between two  $3 \times 29.5 \times 29.5 \text{ cm}^3$  slabs of solid water (which have guides for reproducible  $0 \pm 0.2$  degree alignment with respect to the central axis of the beam). These slabs are further surrounded by polystyrene blocks to give an approximately  $30 \times 30 \times 30 \text{ cm}^3$  solid phantom thus providing full phantom scatter.

#### **3.5.2.2.2 Ion Chamber Array**

The characteristics of ion chambers and ion chamber measurements have been discussed (cf. section 2.4.2). As previously stated, the ion chamber is ideal for most dosimetric measurements. The practical time limitations on single point measurements of a true dynamic beam delivery are overcome when using the array, since the data being collected have a minimum 2cm resolution, and this can be increased by increasing the number of measurements taken. This gives readings with ion chamber accuracy and 2mm spatial resolution in minutes for the average dynamic field (assuming 100MU, 0.3-0.5 minutes per dynamic field, 10 acquisitions). As has been already mentioned, this is still only practical for truly dynamic fields, due to potential charge leakage occurring over the long periods of time associated with the summation of static fields.

## Chapter 4

### Results

The findings of this work can be divided into several distinct areas: performance and utility of the various dosimeters used; results on the necessity of the corrections made to the fluence profiles; results from the generation of arbitrary fluence profiles by both the sum of static fields and by true dynamic motion of opposing collimator jaws; and the generation of dynamic dose profiles by dynamic collimation.

#### 4.1 Dosimeters

The dosimeters used in this study were chiefly of two types: film and ion chamber. Both film and ion chamber were used for the evaluation of fluence and dose profiles. Limited use of diode measurements was made for the evaluation of non-dynamic in-air profiles, and these served as the measurements to which the results of the penumbral modelling were compared (cf. 4.2.3).

##### 4.1.1 Fluence Measurements

In the evaluation of dynamic fluence profiles, two dosimeters were used: film and ion chamber array.

The film technique is found to yield reproducible results. The results from five  $10 \times 10 \text{ cm}^2$  open field films, processed at the same time and under identical conditions, and all calibrated with a single calibration function, were examined. The maximum variation in the PDD between any two films was 2%, but this was an extreme, with the mean variation within 0.5% to 1%.

A difficulty with the use of film for the measurement of the fluence profiles is the smearing of the signal resulting from scatter generated within the buildup plate. This effect of scatter is in part due to the lateral range over which incoming photons may be scattered away from their initial trajectory (see figure 4.1). This effect was measured using the set up shown in figure 4.2 with a 6MV beam incident on 10 cm thick blocks of lead, or approximately 7.5 half-value layers of lead, defining a slit width of 0.25 mm. In one measurement, a buildup plate is placed on top of the thin slit to screen out contaminant electrons in the x-ray beam, and in the other measurement the plate is used to provide scatter below the slit. When the films that were exposed in this manner were developed and scanned with a densitometer, the resulting profiles (figure 4.3) clearly show the effect of scatter on the film signal when the buildup is employed, with the profile of the signal with the poly block in direct contact with the film showing a marked widening.



Figure 4.1 Blurring of signal on film from scatter in the buildup plate.

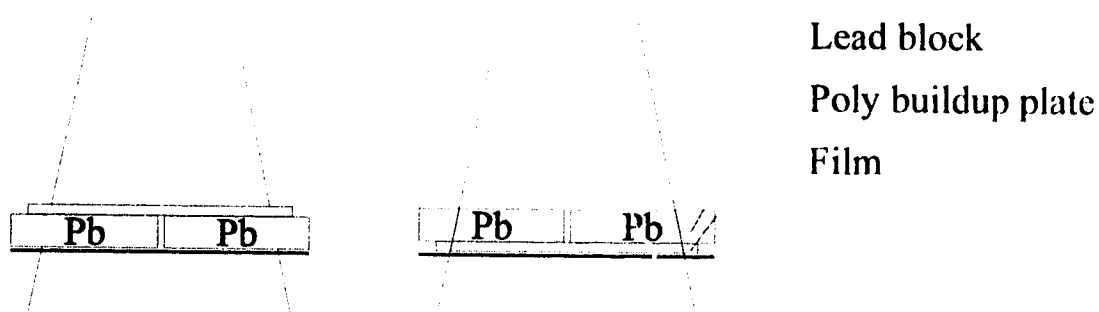


Figure 4.2 Experimental set-up to examine blurring of signal on film from buildup plate.

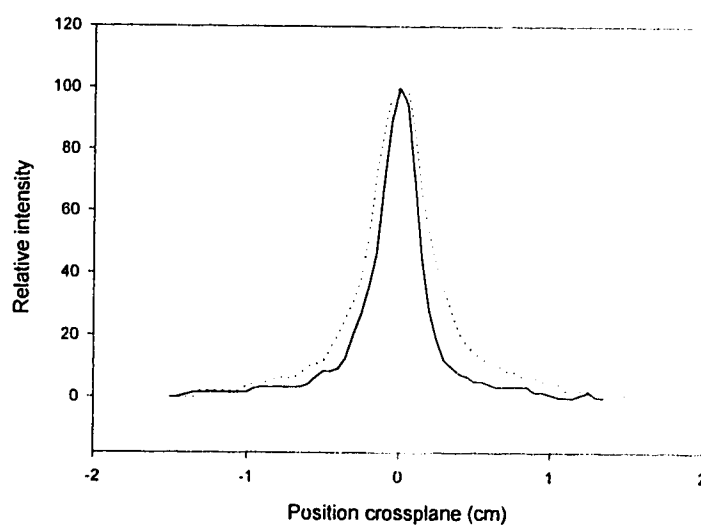
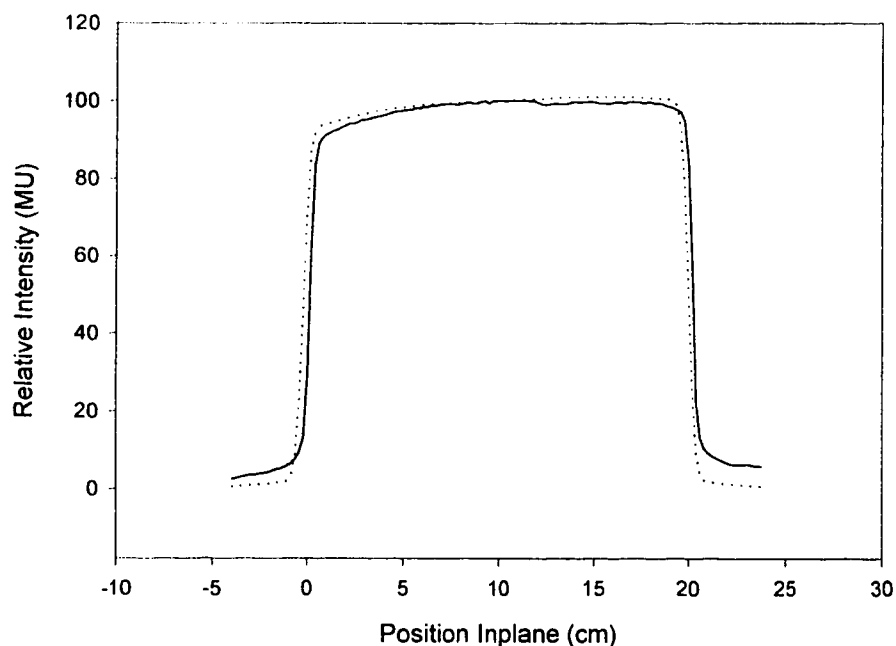


Figure 4.3 A comparison of the measurement of signal on film with (dotted) and without (solid) buildup plate (6 MV, Varian 2300CD).

By using the differential OD technique outlined in 3.5.1.1, it is possible to compare a measured profile with the prediction of what one should expect to measure, i.e. a 'blurred' or 'smeared' prediction of what the actual penumbral corrected (cf. 3.3.3) fluence profile should look like. Two profiles were calculated as predictions for the measurement of an open asymmetric field, making different assumptions: the first is penumbral corrected without the effect of the buildup plate on measurement (see figure 4.4), and the second is a prediction involving both the penumbral correction and smearing of the signal due to the buildup plate (see figure 4.5).

Examining figure 4.4, one finds that the addition of penumbral effects yields only modest agreement between the actual measurement of the profile and the prediction of the measurement, giving large discrepancies (on the order of 40% in the penumbral region, and upward of 5% in the non-penumbral region) between prediction and measurement.



*Figure 4.4 Measured (solid) and predicted (dotted) 20x20 cm<sup>2</sup> in-air profiles assuming imperfect collimation, but assuming no blurring due to scatter (6 MV, Varian 2300CD).*

Figure 4.5 clearly demonstrates excellent agreement between the smeared predicted profile and the actual measured value within the upper bound of 1 to 2% variance expected in film [Waggener 1982]; this may explain the continued disagreement at the right side of the top portion of the field. This result strongly indicates that the unsmeared fluence profile as predicted by the model, with the penumbral correction, is a very good representation of the true fluence profile produced by the linear accelerator used in these studies.

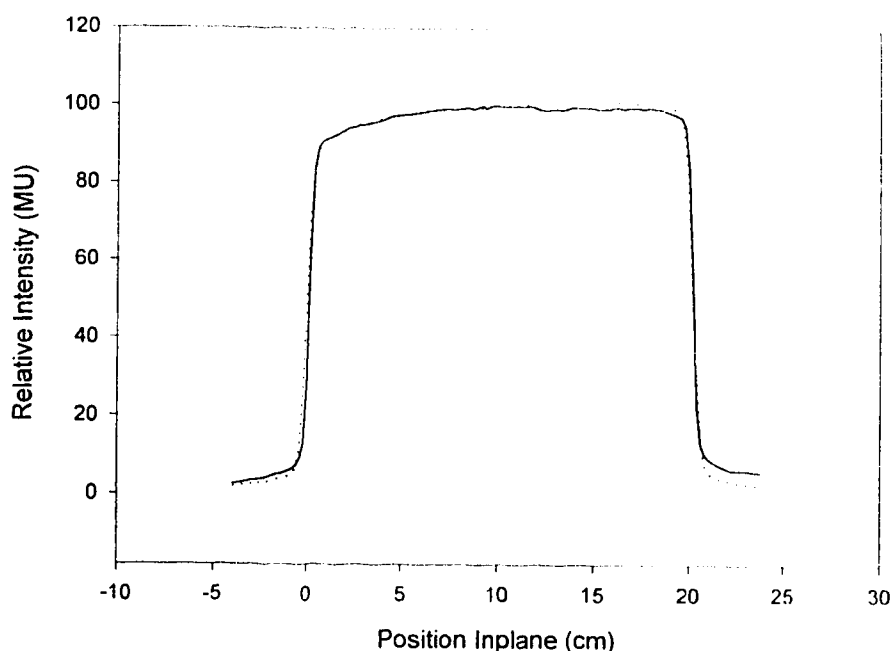


*Figure 4.5 Measured (solid) and predicted (dotted) 20x20 cm<sup>2</sup> in-air profiles assuming imperfect collimation and blurring in measuring (6 MV, Varian 2300C'D).*

The same smearing effect can be seen in measurements with an ion chamber. This effect is also due to the generation of scatter, i.e. the presence of buildup material, which modifies the signal. The smearing is characteristic of the size and composition of the buildup cap used, and is sometimes termed the probe response function. This probe response function has been measured, as was depicted in figures 3.24 and 3.25, by scanning an ion chamber through a thin slit of radiation (produced by a 6MV beam incident on 10 cm thick lead blocks, about 7.5 half value layers, defining a slit width of 0.25 mm). By inspecting the results in figure 4.6 it is clear that

the brass cap has less of a blurring effect on the measured signal under the thin slit than does the acrylic cap.

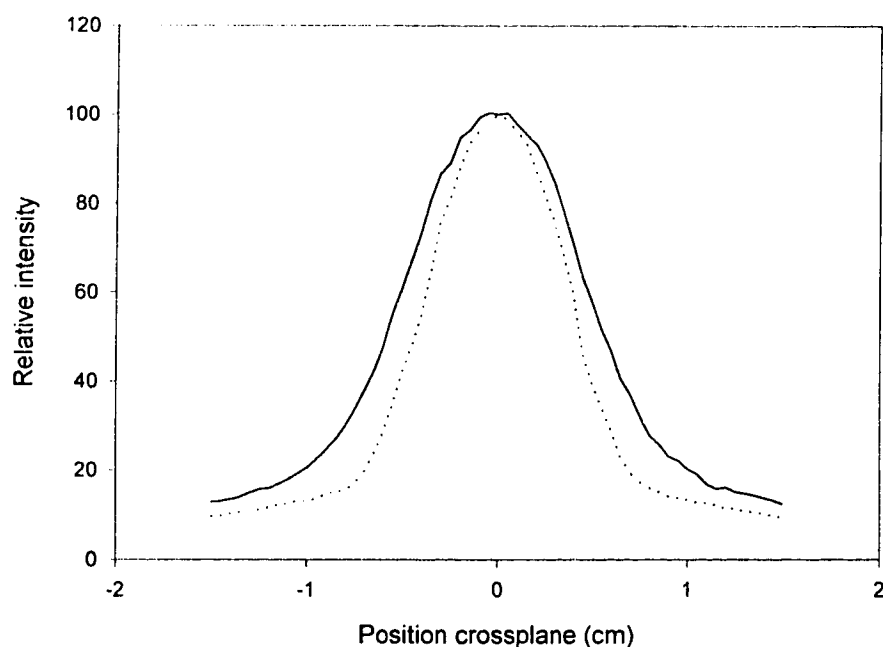


*Figure 4.6 Profiles measured with an ion chamber under a thin slit using acrylic (solid) and brass (dotted) buildup caps (6 MV, Varian 2300CD).*

Comparing, in figure 4.7, a fluence measurement in an open symmetric  $10 \times 10$   $\text{cm}^2$  field from an ion chamber array, using an acrylic buildup cap, with a measurement in the same open field from an ion chamber array using brass buildup caps, the thinner high Z brass caps demonstrate a significant improvement toward measuring the true fluence over that achieved with the acrylic cap. This effect is due to the smaller diameter of the brass buildup caps (recall figure 3.24, 3.25), and therefore the lower flux incident on a given cross section. In this study, measurements with brass caps are thus taken to be a good approximation of the true fluence produced by the accelerator.

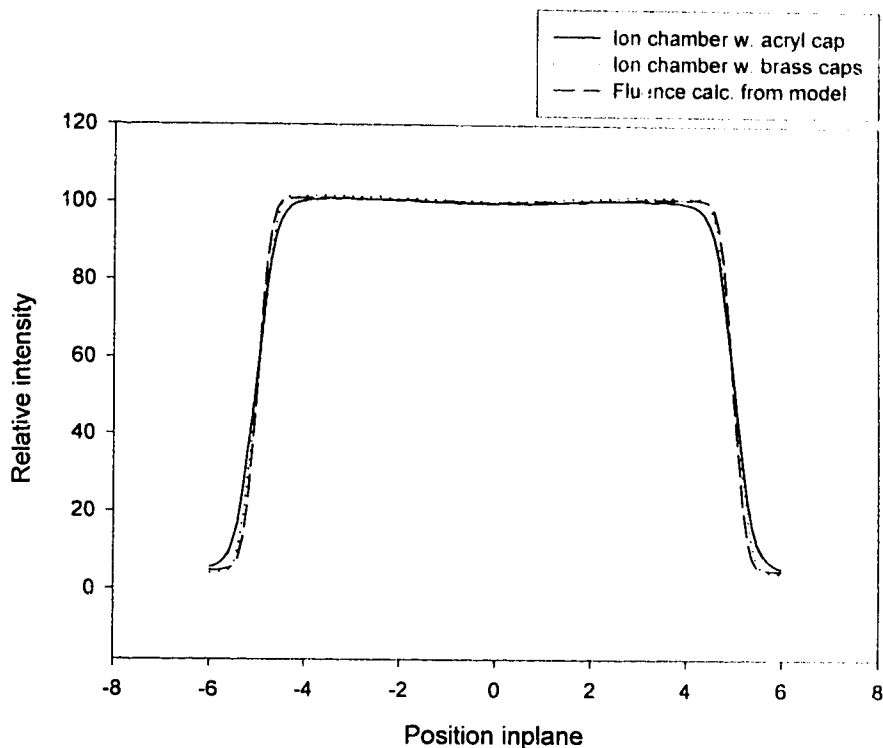


*Figure 4.7 A comparison of measurements of a  $10 \times 10 \text{ cm}^2$  open field with the ion chamber array, with both brass caps (dotted line) and a thicker acrylic cap (solid line), to a predicted value for the true fluence (dashed line) (6 MV, Varian 2300C'D).*

#### 4.1.2 Dose Measurements

For the evaluation of dose measurements, the ion chamber array was used exclusively for the final results. Film was used for early evaluation of dynamic wedge isodose profiles, but more recent results with the ion chamber array have cast doubt on the validity of the conversion method used in these earlier attempts at dynamic wedge dosimetry (see figure 4.8); the failure toward the heel of the wedge is chiefly due to changes in the field spectrum in this region as the jaw closes.

The dosimetry of the dynamic wedge with film was much more difficult than with the ion chamber array, and a comparison of the two techniques shows that the results from the initial calibration of the dynamic wedge films were incorrect. This is due to some assumptions made about the spectrum of the beam across the field, especially in the high gradient regions; as well, this failure casts doubt on some



assumptions made by others [Leavitt 1994c] with respect to dynamic wedge film dosimetry. The major complicating factor in the use of film as a dosimeter is the change in film response with depth. This is a factor which has been widely noted (see section 3.5.2).

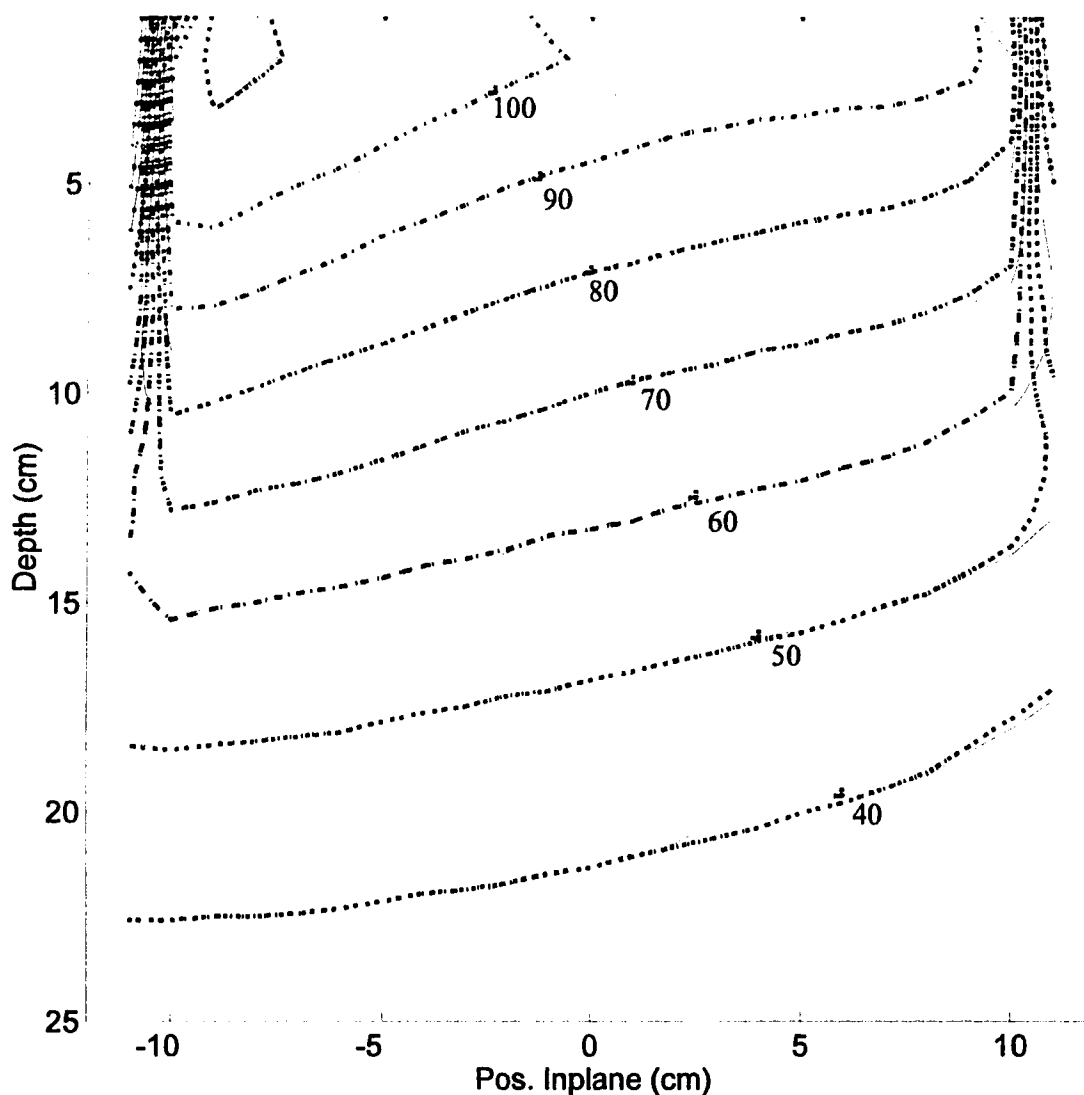


Figure 4.8 15 degree  $20 \times 20 \text{ cm}^2$  field dynamic wedge isodose measurement made using film (dotted line) and linear ion chamber array (solid line) (6 MV, Varian 2300CD).

Results from ion chamber measurements are taken to be correct, as ion chambers do not exhibit the energy dependency inherent in film. As mentioned

previously (cf. 3.5.2), ion chamber measurements form the gold standard for measurements in radiotherapy dosimetry. The utility of any other dosimeter is always assessed by comparison to that of an ion chamber.

## 4.2 Corrections

A number of simplifying assumptions were made for the purposes of calculating the jaw motions for a dynamic treatment. These include assumptions about the energy fluence distribution, the variation of output with both the asymmetric offset of fields and with field size, and assumptions about the degree of collimation that is truly present. Looking at the results from the generation of example profiles with and without certain corrections highlights the necessity of these corrections.

The corrections addressed in this work are, in particular, for the variation of output with any offset from the CAX (the AOF mentioned in 3.3.1), the variation of output with field size (the ROF described in 3.3.2), as well as the cumulative effect of the penumbra arising from the jaws (this effect was discussed in 3.3.3). The methodology of implementation of these corrections is also laid out in section 3.3

### 4.2.1 AOF Correction

The variation of the output for asymmetric fields is tied to the variation of the primary energy fluence profile (as per figure 3.6). The assumption is made that correction for the AOF can be made by simply modifying the desired input profile on a point by point basis, based on the position of the points defining the profile with respect to the CAX. By dividing the profile through by the value of the relative primary energy fluence profile, normalised to the value on the CAX, the input profile is modified such that the actual output is the desired profile (see figure 4.9). An example desired profile is given in figure 4.10 for a  $20 \times 20 \text{ cm}^2$  asymmetric field (10 cm offset), both with and without the correction.

Making no assumptions about energy fluence variations in the field with position or field size, or about the degree of collimation, the attempt is made to generate the profile shown in 4.9 as a solid line. The result of this is shown as a dotted line in figure 4.10. Subsequently, using the modified relative fluence distribution as the input profile (the dotted line in 4.9), another output fluence profile was generated (shown as the solid line in figure 4.10). Comparing the profile generated with the AOF correction and the profile generated without the AOF correction to the desired profile (figure 4.10), the utility of the AOF correction is demonstrated, as agreement with the ideal profile is improved, especially in the region close to  $x=0$  (where the gradient of the primary fluence is steepest; cf. section 2.3.2).

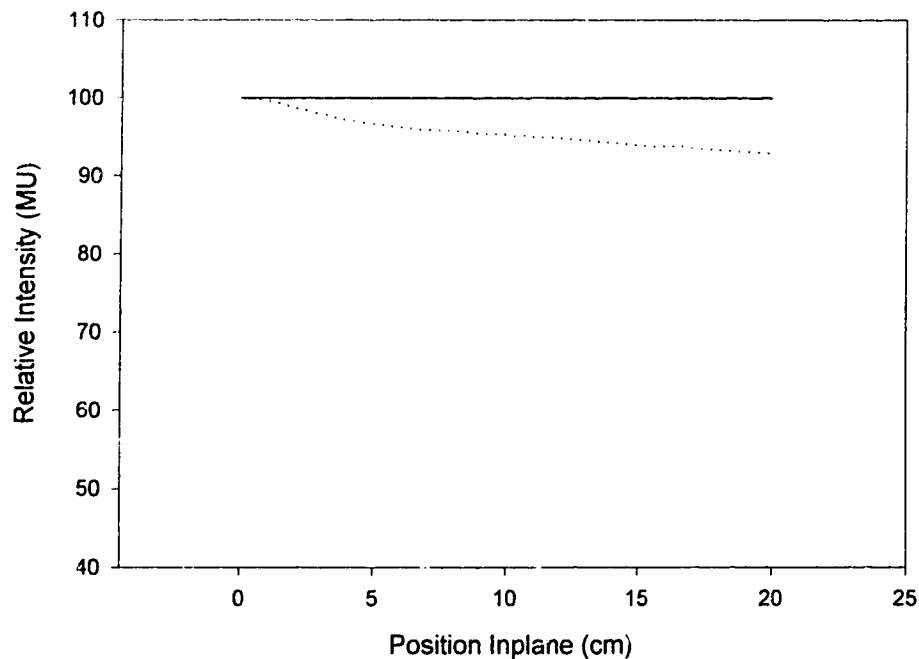


*Figure 4.9 A desired profile (shown as solid line) is modified (shown as dotted line) according to the relative primary energy fluence values, giving the AOF correction. The output resulting from the dotted profile should be close to the form of the solid line (see figure 4.10) (AOF from 6 MV beam, Varian 2300CD).*

It is evident that there is still some discrepancy between the ideal desired profile and the profile generated with the AOF correction. This is due to other factors that are not corrected for in this example, namely the imperfect collimation of the beam (the penumbral effects) and the variation of output with field size (the ROF effect). The ROF effect is most dramatic for small fields and results in the discrepancy between the AOF corrected profile and the ideal desired profile being larger close to  $x=0$  as compared to the region close to  $x=20$  cm.

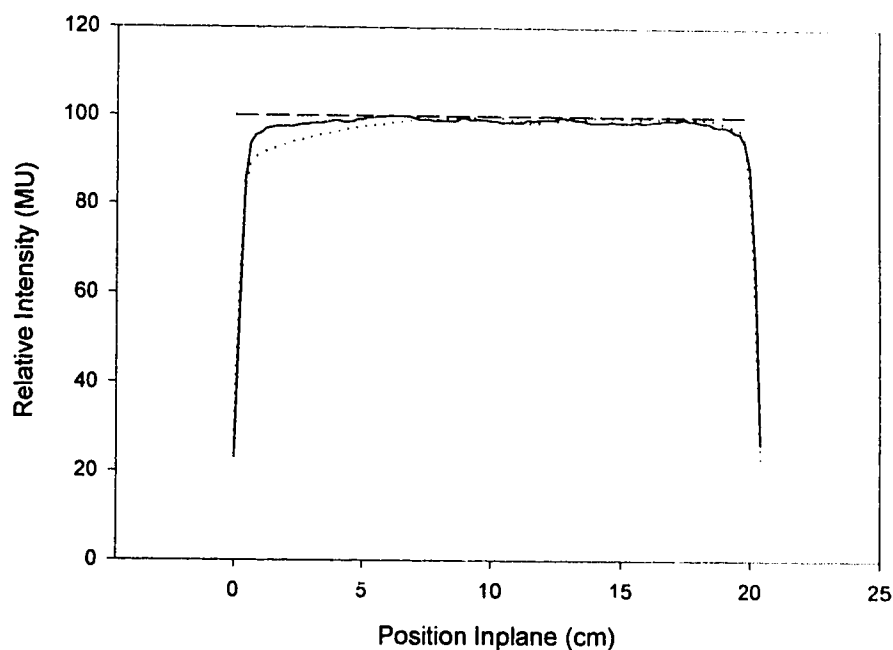


*Figure 4.10 The 20x20 cm<sup>2</sup> field profile generated with the AOF correction (solid) and without (dotted), compared to the desired profile (dashed); generated with simulated DBD, using film as dosimeter (6 MV beam, Varian 2300CD).*

#### 4.2.2 ROF Correction

The variation of output with field size is a factor that must also be corrected for in the generation of dynamic fields since the instantaneous field size changes during beam delivery. This correction is performed by first generating a delivery schedule (the jaw positions as a function of time or cumulative intensity in MUs), then modifying the incremental output values based on the varying field size. Values for the ROF were measured using an ion chamber with a brass cap, positioned at a far field distance (cf. 3.3.2).

Consider the fluence profiles as shown in figure 4.11. The desired output is 100% relative fluence within the plateau of all three segments (shown as A, B and C). Failure to correct for the variation in relative output (ROF) as a function of field size (jaw opening) results in the fluence profile described by the solid line. The relative output for the segment generated by a smaller opening (B) is clearly less than that for

the larger jaw openings (A and C). Correcting for the variation in output as a function of field size using the ROF data collected as per 3.3.2 yields the desired output fluence profile (the dotted line), except near the edge of each segment. This discrepancy in high gradient regions, also seen in figure 4.11, is due to penumbral effects not accounted for in this example, although this example does employ the AOF correction.

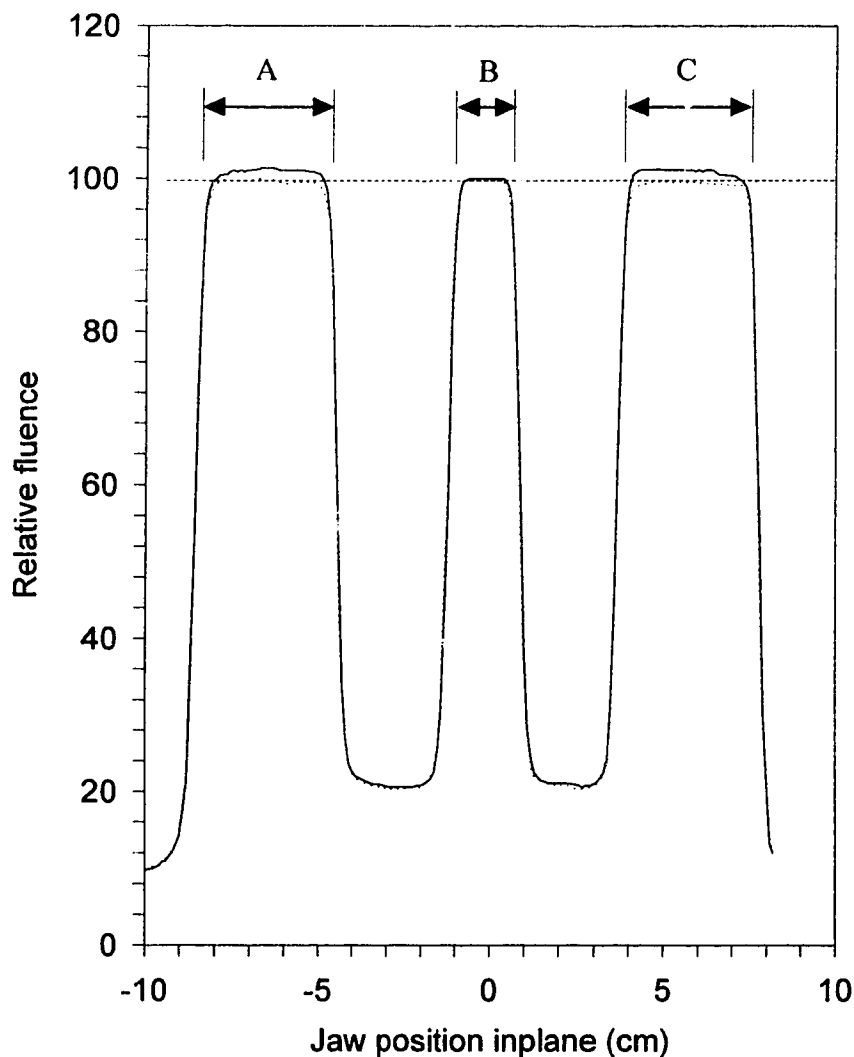


*Figure 4.11 The profile generated with the ROF correction (dotted) and without (solid); generated with simulated DBD, using film as dosimeter. A solid line is given at 100 arbitrary units to show relative positions of the peaks (6 MV, Varian 2300CD).*

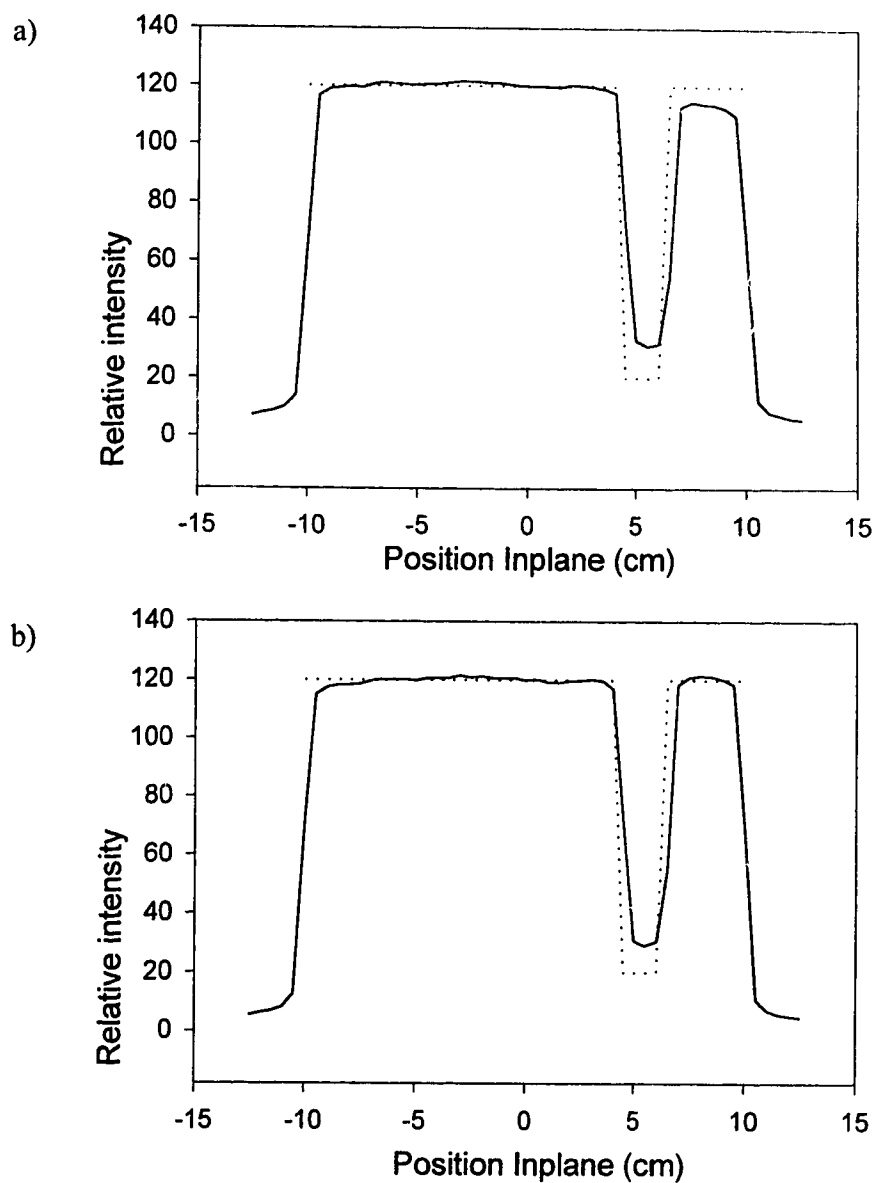


*Figure 4.12 Another example comparing a delivered field (solid) to an ideal desired profile (dotted); generated with simulated DBD, using film as dosimeter. The top graph shows a field prior to ROF correction, and the bottom indicates the field achieved after corrections are taken into account (6 MV, Varian 2300CD).*

A second example with more extreme variations in field size also serves to highlight the necessity of accounting for the variations in output that arise with these

changes in field size (cf. figure 4.12). Figure 4.12 a) is the desired versus the delivered field without the ROF correction but with the AOF correction. Figure 4.12b) is the desired versus the delivered field with both the ROF and AOF corrections. ROF correction was achieved by using measured ROF data (cf. 3.3.2.1) to dictate the amount by which the smaller segment of the field (at right in figure 4.12b) must be 'overdosed' relative to the larger segment of the field (since the smaller segment receives less actual output for the same MU setting).

### 4.2.3 Penumbra Model and Corrections

The simple geometric model and the extended geometric models alone do not suffice to accurately model the penumbral region. They produce only a narrow linearly varying penumbra without any of the rounding and gradual tapering seen in the measured penumbra (cf. figure 3.12). For this work the extended geometric model is combined with a source distribution as predicted by a dual source model (focal and extra focal components), each with a Gaussian distribution. This, along with the one dimensional integration simplification suggested above, produces results in good agreement with experiment, as seen in figure 4.13.

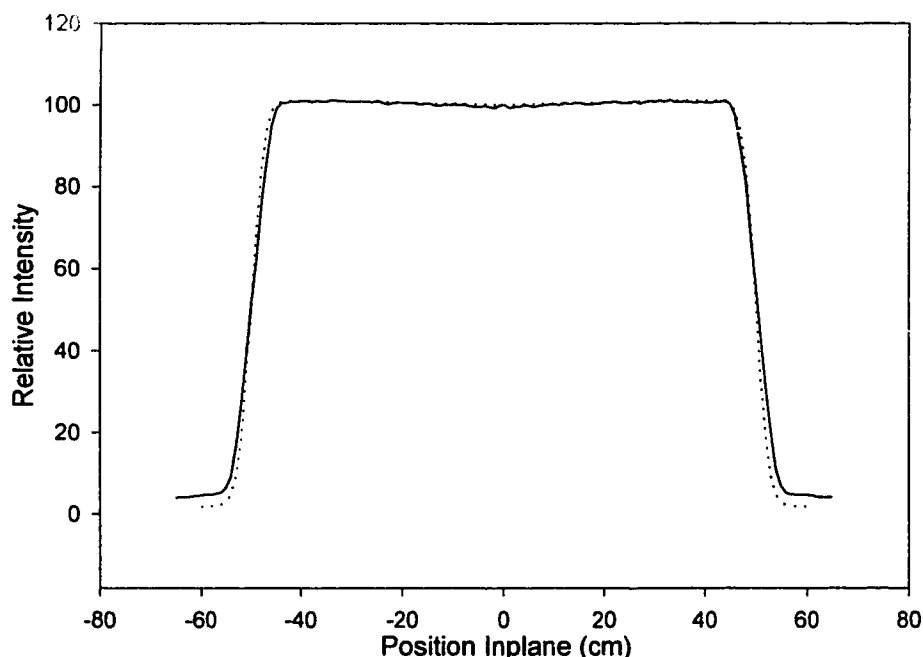


*Figure 4.13 Comparison of calculated (dashed) and measured (solid) fluence profiles, 10x10 cm<sup>2</sup> field (6MV beam, Varian 2300CD, diode).*

The discrepancies seen in the  $< 5\%$  region of the penumbra are due to the lack of inclusion of jaw transmission in the model, which, as has been noted, should be about 2-3%. This is an aspect of the assumption of perfect collimation that has not been relaxed. Were one to add a constant 3% transmission through the jaws at the field edges, the penumbra would appear as they do in figure 4.14.

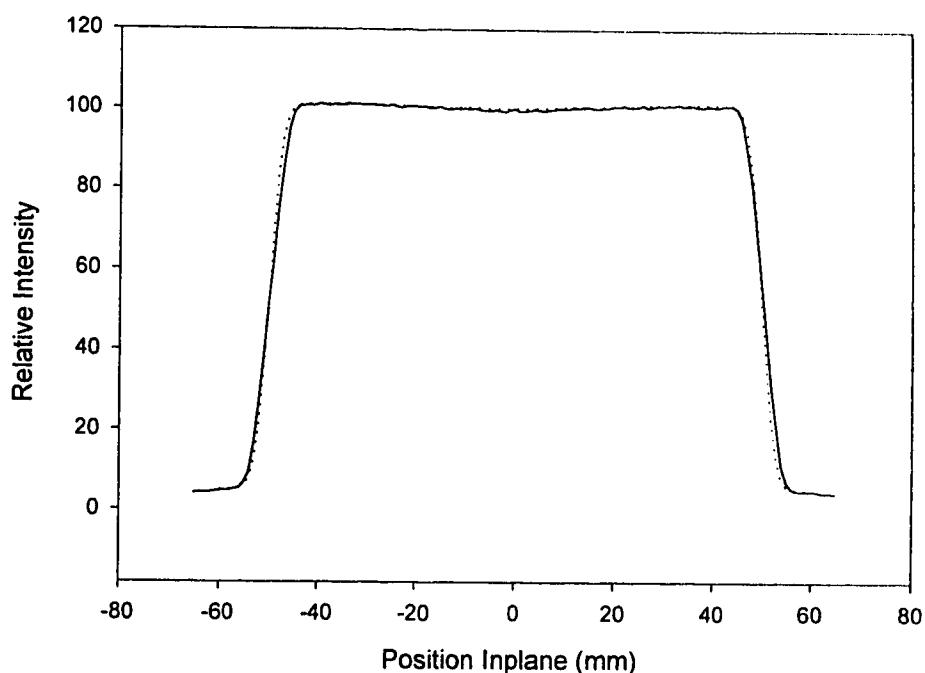


*Figure 4.14 Comparison of calculated (dashed) and measured (solid) fluence profiles, assuming 3% transmission through the jaws,  $10 \times 10 \text{ cm}^2$  field (6MV beam, Varian 2300CD, diode).*

For any field, imperfect collimation by the collimating jaws gives rise to penumbral regions at the jaw's edge. Within this penumbral region, the field will deviate from the desired profile. This will be most evident in high gradient regions. By calculating the penumbra associated with each collimating jaw one may in turn correct for its presence. This will be realised by increasing the fluence in regions that are underdosed, and vice-versa for the overdosed regions. The jaw motions are then recalculated based on this new input profile. By doing this iteratively (calculate penumbral effect, make a correction to achieve a new input profile, calculate new jaw



motions, calculate new penumbral effects, ...) one may converge to a solution for the motions required to deliver the desired profile.

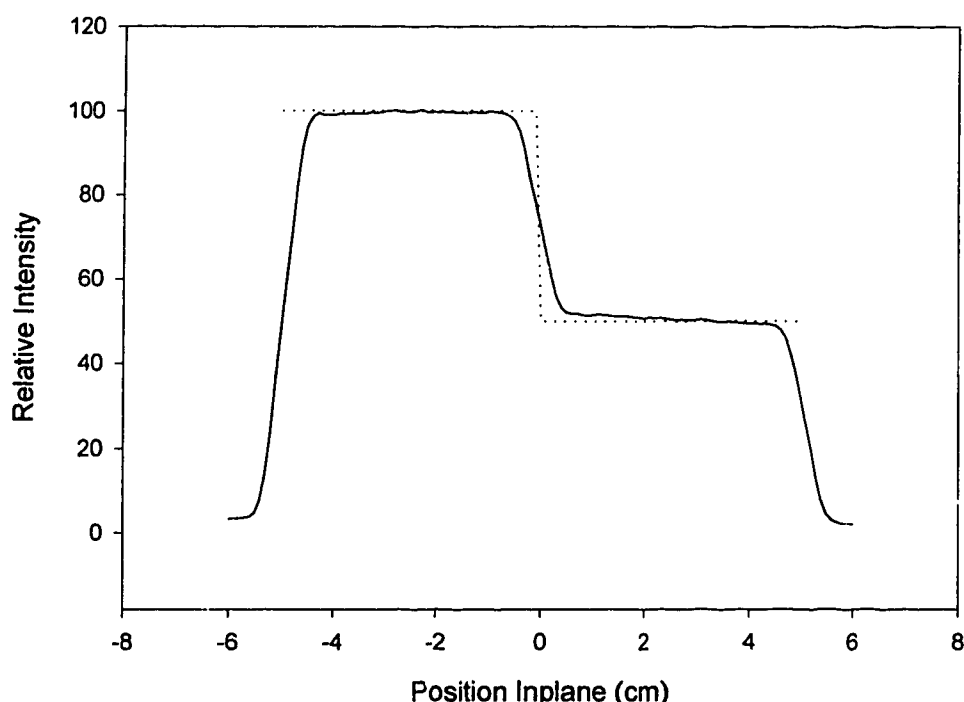


*Figure 4.15 A comparison of a desired step profile (solid) versus a profile measured in air with ion chamber array (dotted), generated by true DBD<sup>4</sup>, and employing the AOF and ROF corrections, but without any penumbral corrections (6 MV, Varian 2300CD).*

The impact on the generation of a dynamic field due to penumbral effects was examined. For the case of an open field, departure from the desired profile is evident at the field edge. An attempt to generate an idealised step fluence profile is shown in figure 4.15. The dotted line is the desired step profile and the solid line is the measured output profile generated using AOF and ROF corrections, but without corrections for the penumbral effects. If, using the dual Gaussian penumbral model of section 3.3.3, penumbral effects are included in the desired step fluence profile, then the dotted line of figure 4.16 results. The good agreement between the experimental data and the theoretical profile (with the penumbra added according to the model) is evident. This indicates that the penumbral model may be used as an accurate predictor of the penumbral effect.

<sup>4</sup> Using dynamic beam delivery research software

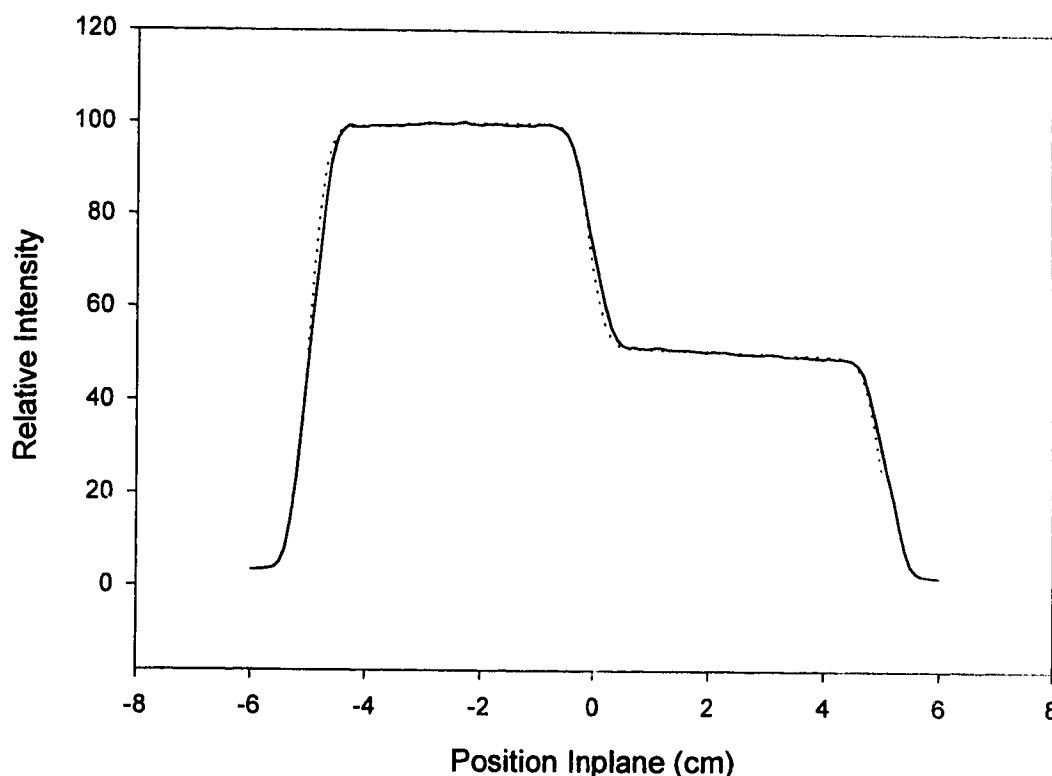


*Figure 4.16 A comparison of the predicted profile (dotted) versus a measured profile (solid) (6 MV, Varian 2300CD).*

In order to improve the adherence to the desired profile at sharp discontinuities, an iterative penumbral correction is performed on the input profile. The limitation of imperfect collimation which gives rise to the field penumbra suggests perfectly sharp field edges are physically impossible to achieve. This is indeed the case, as is demonstrated in figure 4.17. The dashed line represents the ideal profile, with perfectly sharp boundaries. The solid line is the profile produced with the AOF and ROF corrections, but without any penumbral correction. The dotted line is the generated profile using the AOF, ROF and penumbral correction. In this example, the iterative penumbral correction results in only a moderate improvement in the sharpness, when the goal is perfect sharpness. This appears to indicate that one should only require reasonable sharpness (i.e. not too steep a gradient, as opposed to the high gradient that perfect collimation would deliver) and not expect perfect sharpness at these interfaces.

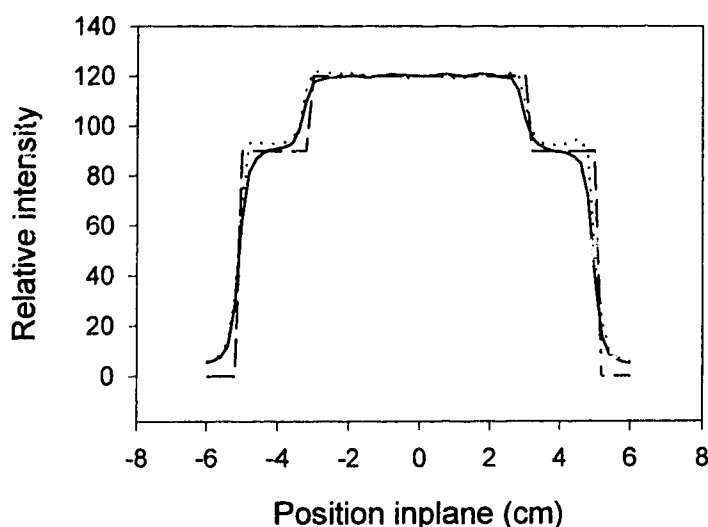


*Figure 4.17 A comparison of a desired profile (dashed) along with profiles measured with film, produced by a sum of static fields without (solid) and with (dotted) penumbral corrections (6 MV, Varian 2300CD).*

As a final example of the necessity of the various aforementioned correction factors, these corrections are successively applied to the generation of a flat, symmetric  $10 \times 10 \text{ cm}^2$  field. These fields are generated by true DBD and measured using the linear ion chamber array, with brass buildup caps and a spatial resolution of 2mm between measured points -- it is this finite resolution that gives rise to the jagged appearance of the profiles.

In figure 4.18, the open and uncorrected field is compared to the desired flat profile. Clipping off the geometric penumbral region from the scan, the disagreement is on the order of upwards of 1.5 % high for the open field scan which is well outside the 0.5% variance one might expect due to noise in the signal. The AOF corrected field shown in figure 4.19 lies as much as 2.5% below the desired profile, due to a failure to account for the broad rounding due to the penumbra which is accounted for by the secondary, lesser strength Gaussian source of 3.3.3. From the field in figure 4.20 it can be seen that the ROF correction, added to the AOF correction, fails to improve the adherence of the profile, due to the fact that the field size for this particular delivery never falls below 5cm, so the output variation with field size is not an issue. Accounting for the penumbral effect in the dynamic field of figure 4.21 produces a flat field with the range expected due to the noise in the signal, except for

some overdosing at one field edge (this is due to a failure in the penumbral model to account for physical limitations in jaw separation).

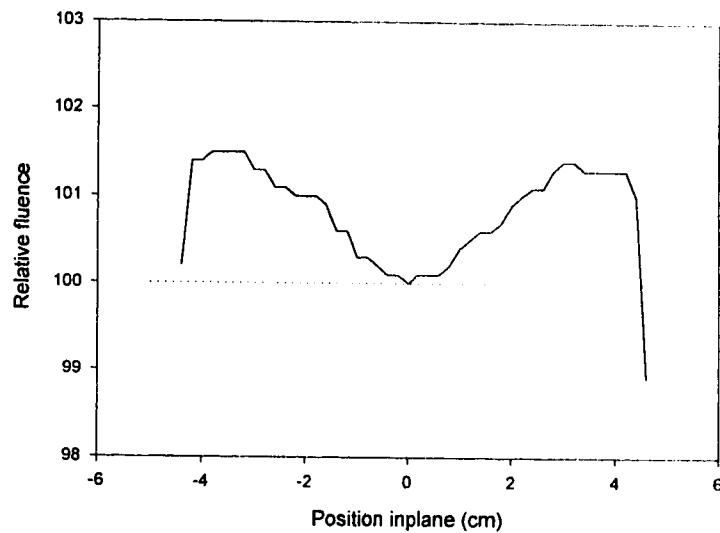


*Figure 4.18 A comparison of a desired flat profile (dotted) to the 10x10 cm<sup>2</sup> open profile measured with ion chamber array in air with brass buildup caps (solid) (6 MV, Varian 2300CD).*

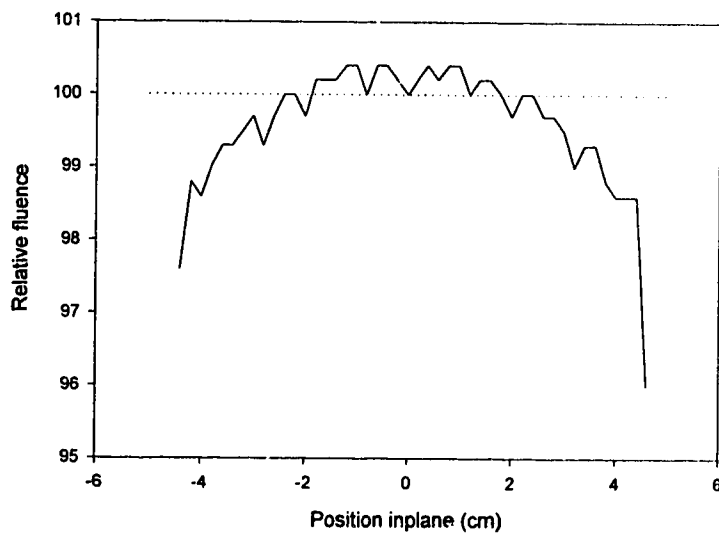


*Figure 4.19 A comparison of a desired flat profile (dotted) to the 10x10 cm<sup>2</sup> open profile measured in air (with ion chamber array with brass buildup caps) using the AOF corrections (solid) (6 MV, Varian 2300CD).*

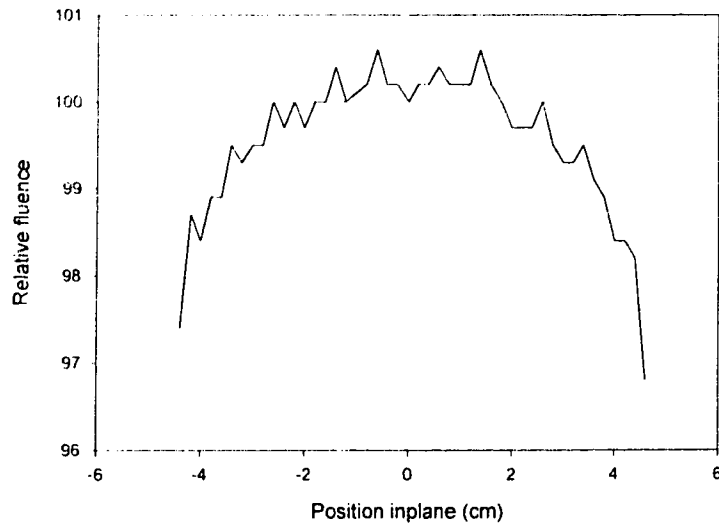


*Figure 4.20 A comparison of a desired flat profile (dotted) to the 10x10 cm<sup>2</sup> open profile measured in air (with ion chamber array with brass buildup caps) using the AOF and ROF corrections (solid) (6 MV, Varian 2300CD).*

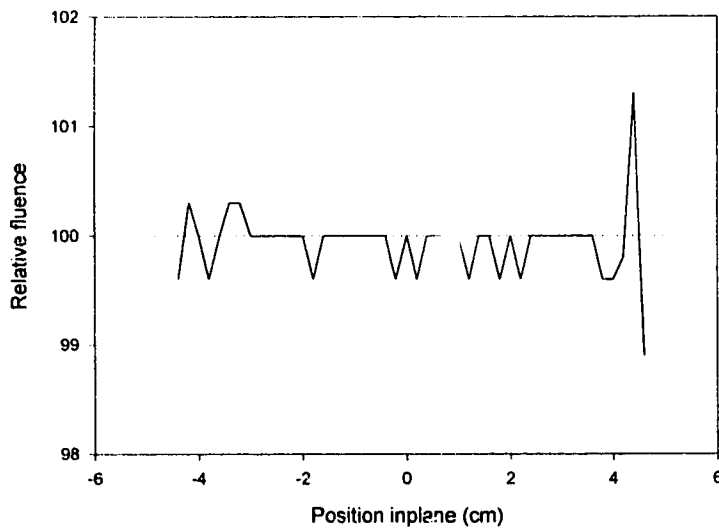


*Figure 4.21 A comparison of a desired flat profile (dotted) to the 10x10 cm<sup>2</sup> open profile measured in air (with ion chamber array with brass buildup caps) using the AOF, ROF and penumbral corrections (solid) (6 MV, Varian 2300CD).*

### 4.3 Dynamic Fluence Profiles

Taking into account the aforementioned necessary correction factors, a number of arbitrary and progressively more complex profiles were generated by both the sum of static fields technique, with film as the dosimeter, and by true dynamic beam delivery (DBD), with both film and linear ion chamber array as dosimeters.

#### Electrometer Reading vs. MU settings

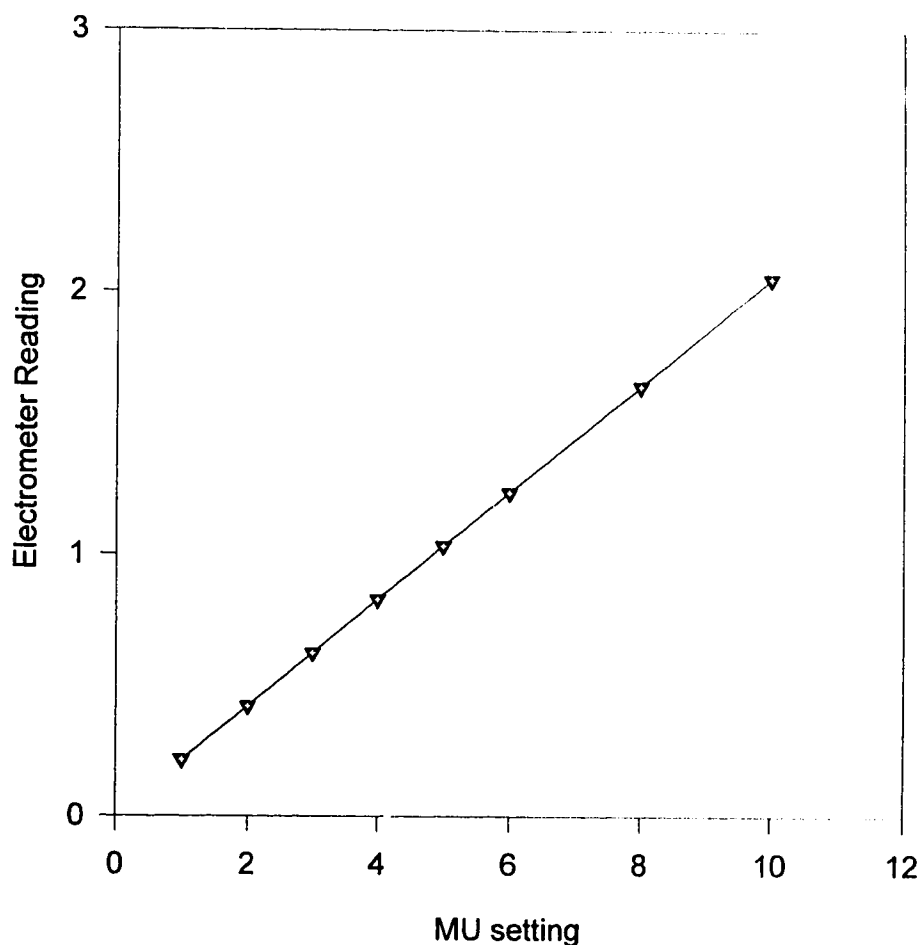
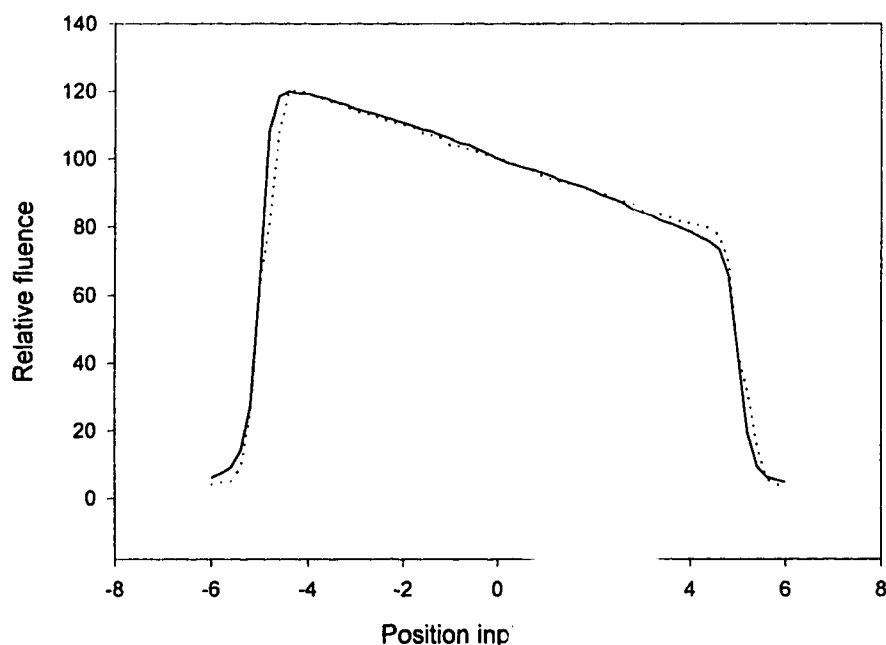


Figure 4.22 Electrometer response (linac output) at low monitor unit settings (6 MV, Varian 2300CD, 10x10 cm<sup>2</sup> field)

A concern in this work for both dynamic fluence and dynamic dose profile production is the linearity of linac output at low dose levels. Any slowly varying region requires that the jaw move at a high speed, and therefore deliver a very low

dose. Some profiles require the delivery of one or two monitor units for a field segment. If the output of the linac is not linear in the low dose region, this would be problematic; the results from tests on the linac output over a large range, including numerous points at the low end of the output range (see figure 4.22), indicate the response is very close to being linear and so this is not currently thought to be a concern.

Three examples of true DBD fields measured with both film and ion chamber array are compared in figures 4.23, 4.24 and 4.25, and good agreement is seen, showing the equivalency of the two dosimetric techniques, except at the field edge. The problem at the field edge is due to the loss of lateral electronic equilibrium (resulting in a lower signal for the ion chamber array) and an over-response to degraded photons (resulting in a higher response by the film).



*Figure 4.23 Comparison of in-air measurements from film (solid) and ion chamber array with brass caps (dotted) of a simple wedge profile generated by true DBD (6 MV, Varian 2300CD, 10x10 cm<sup>2</sup> field).*

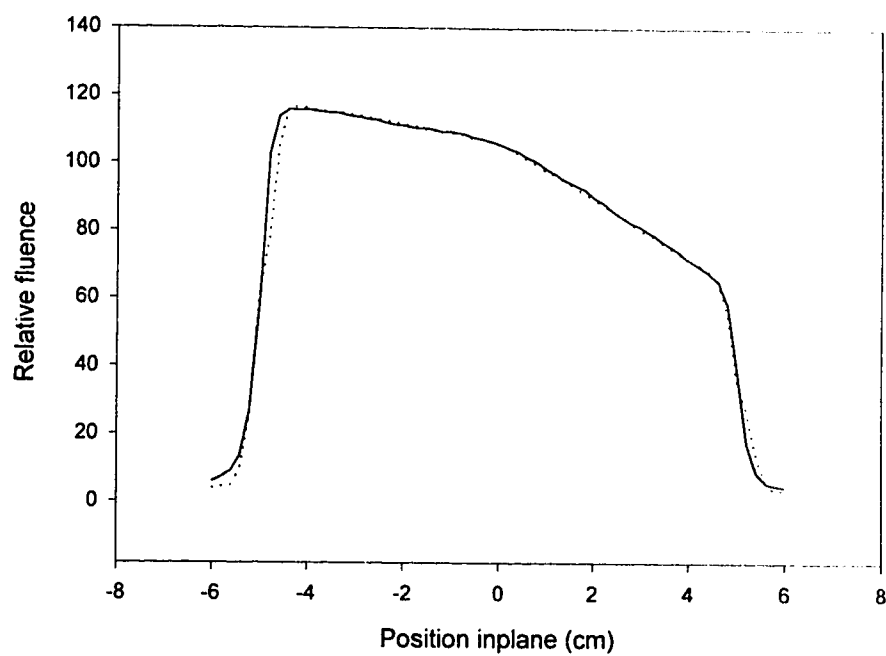


*Figure 4.24 Comparison of in air measurements from film (solid) and ion chamber array with brass caps (dotted) of a split wedge profile generated by true DBD (6 MV, Varian 2300CD, 10x10 cm<sup>2</sup> field).*



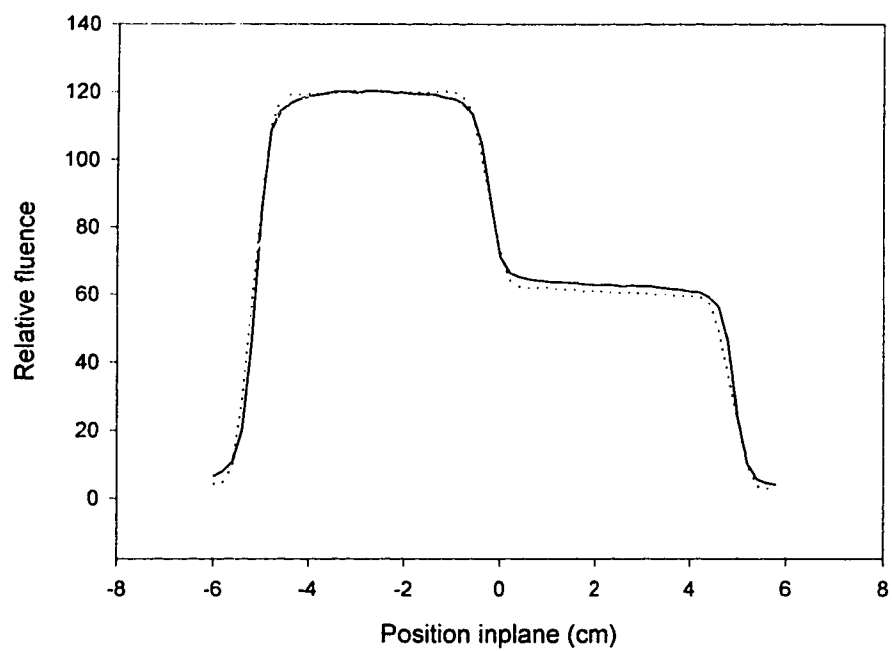


*Figure 4.25 Comparison of in air measurements from film (solid) and ion chamber array with brass caps (dotted) of a step profile generated by true DBD (6 MV, Varian 2300CD, 10x10 cm<sup>2</sup> field).*

The example desired profiles seen in figures 4.23 and 4.24 were also generated using the sum of static fields technique (figures 4.26 and 4.27). The comparisons of generated profiles in figures 4.26 and 4.27 as measured with film serve to demonstrate the equivalency of the two techniques.

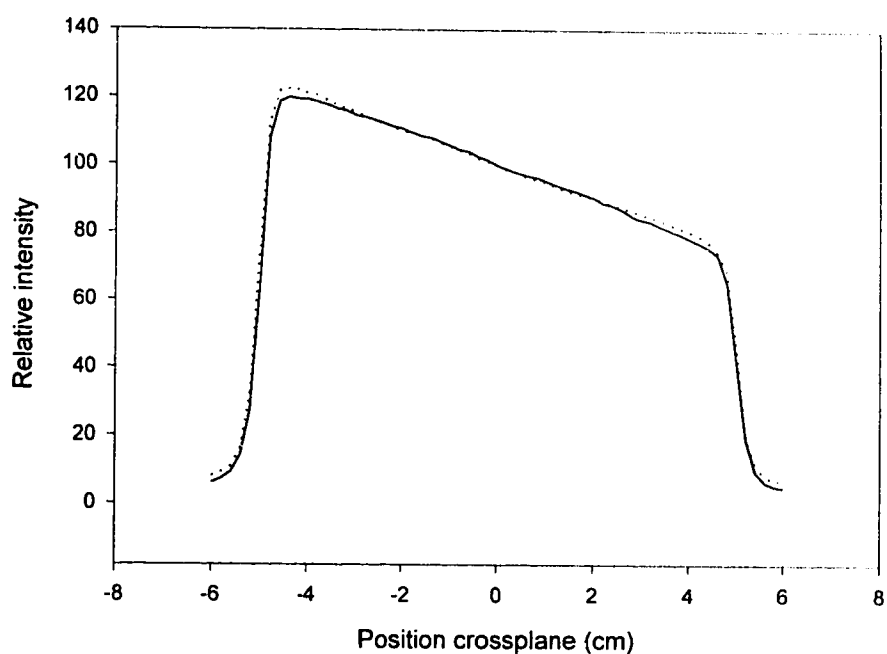


*Figure 4.26 Simple in-air fluence wedge; true DBD (solid) and simulated DBD (dotted) both measured with film (6 MV, Varian 2300CD, 10x10 cm<sup>2</sup> field).*

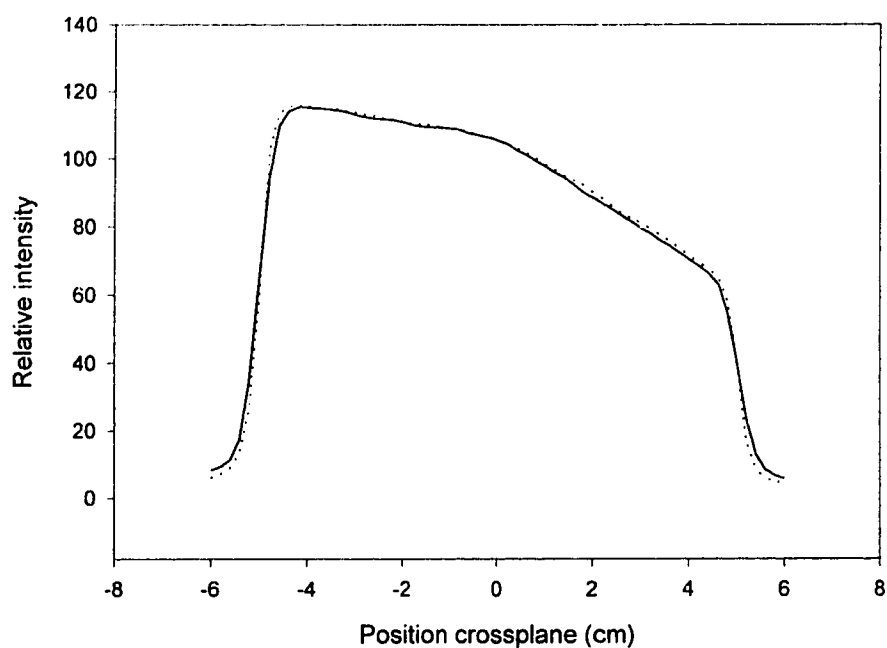


*Figure 4.27 Split wedge in-air fluence profile; true DBD (solid) and simulated DBD (dotted) both measured with film (6 MV, Varian 2300CD, 10x10 cm<sup>2</sup> field).*

Figures 4.28 through 4.30 are generated with true DBD, and the measurements are made using the ion chamber array with brass buildup caps as the dosimeter. The departure from the desired profile seen at the field edges is due to the physical limitation of imperfect collimation.

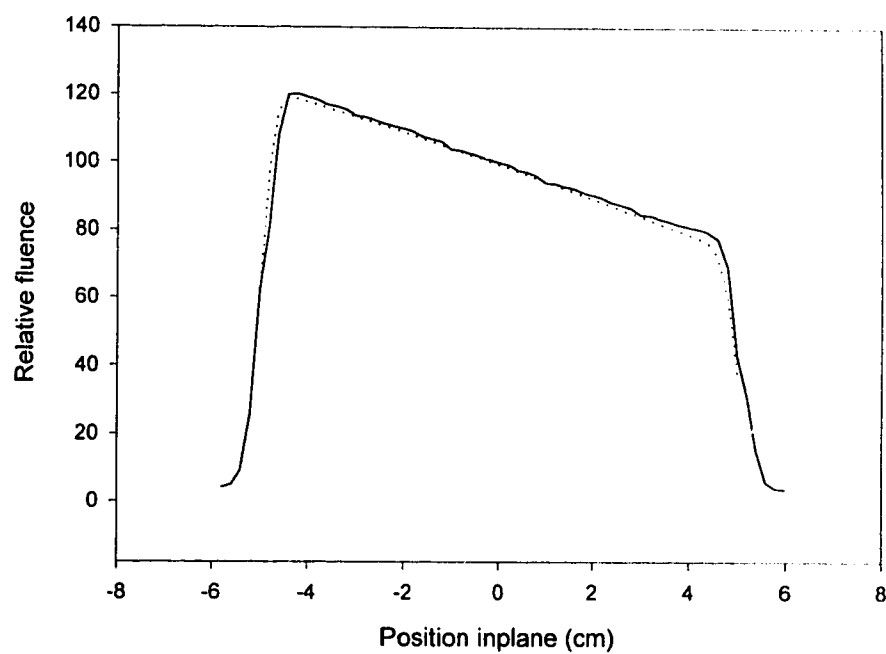


*Figure 4.28 Simple in-air fluence wedge measured with ion chamber array and brass caps; measured (dotted) and ideal (solid) (true DBD delivery, 6 MV, Varian 2300CD, 10x10 cm<sup>2</sup> field).*

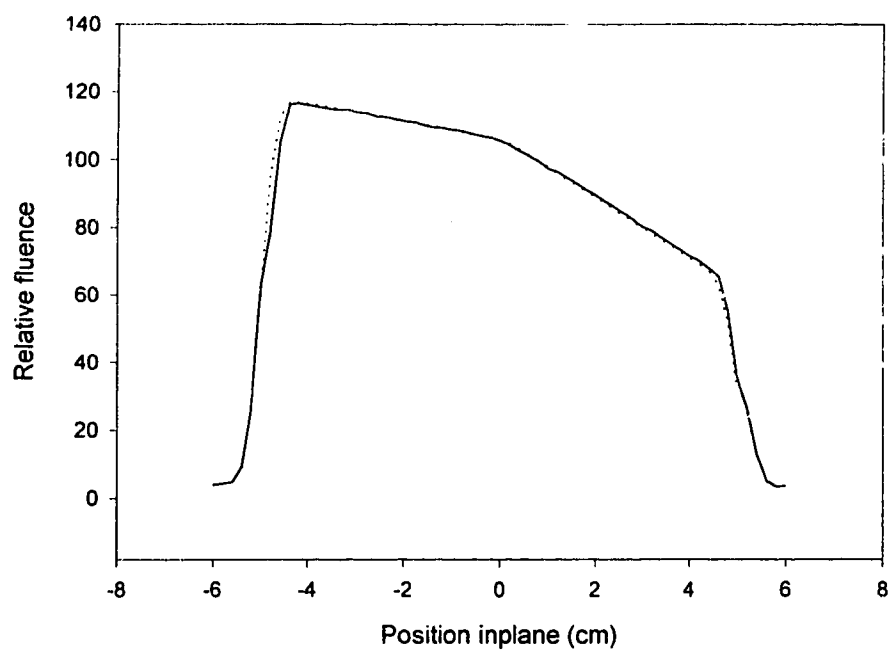


*Figure 4.29 Split wedge in-air fluence profile measured with ion chamber array; measured (dotted) and ideal (solid) (true DBD delivery, 6 MV, Varian 2300CD, 10x10 cm<sup>2</sup> field).*

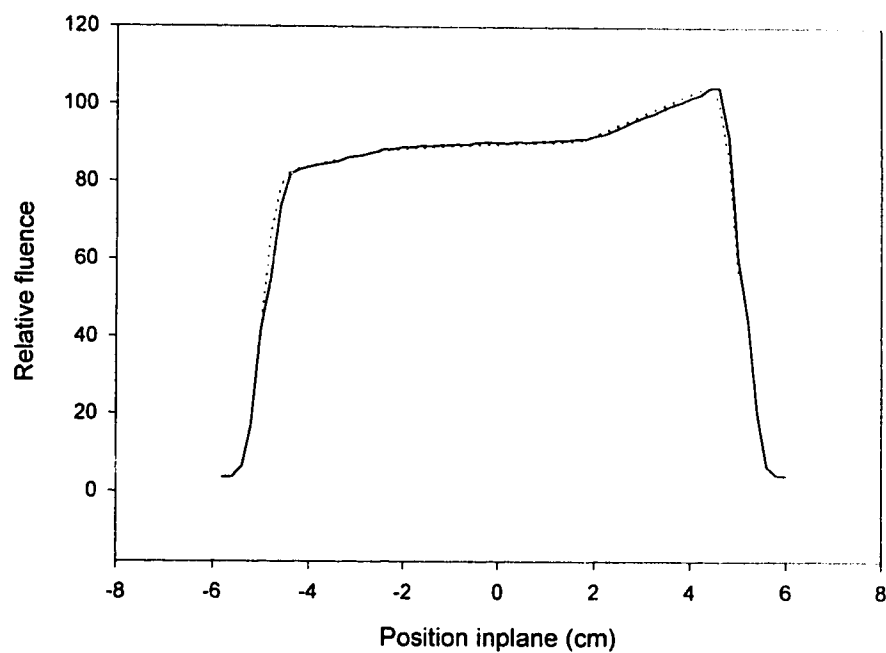


*Figure 4.30 Three section split wedge, in-air fluence measured with ion chamber array; measured (dotted) and ideal (solid) (true DBD delivery, 6 MV, Varian 2300CD, 10x10 cm<sup>2</sup> field).*

A more complex profile was generated, and the ideal profile was modified to allow for a realistic comparison between the measurement with film of the sum of static fields profile and the expected final result. This modification included adding penumbra corrections, as per section 3.3.3.1, and smearing out the ideal signal as per the method outlined in section 3.5.1.1. The final result is pictured in figure 4.31, and yields excellent agreement between the predicted and measured profiles.

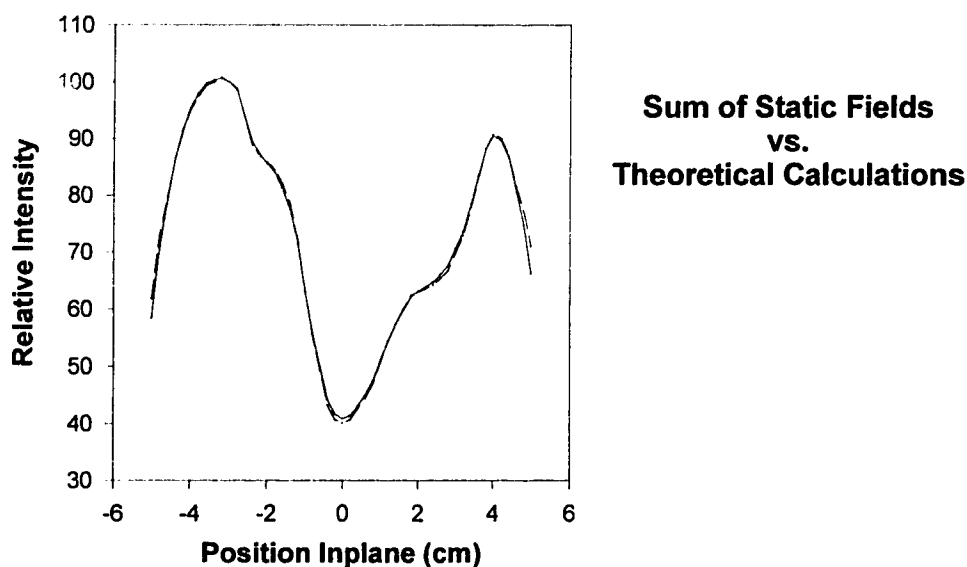


*Figure 4.31 A comparison between the modified desired complex in-air energy fluence profile (dashed) and the measured profile generated via simulated DBD (solid) (6 MV, Varian 2300CD, 10x10 cm<sup>2</sup> field).*

A comparison is also made for the same profile between the fluence profile generated by true DBD, measured with the linear ion chamber array using brass as a buildup medium, and the desired profile. The result is shown in figure 4.32, and the agreement again is quite favourable. This demonstrates the equivalency of the two delivery techniques.

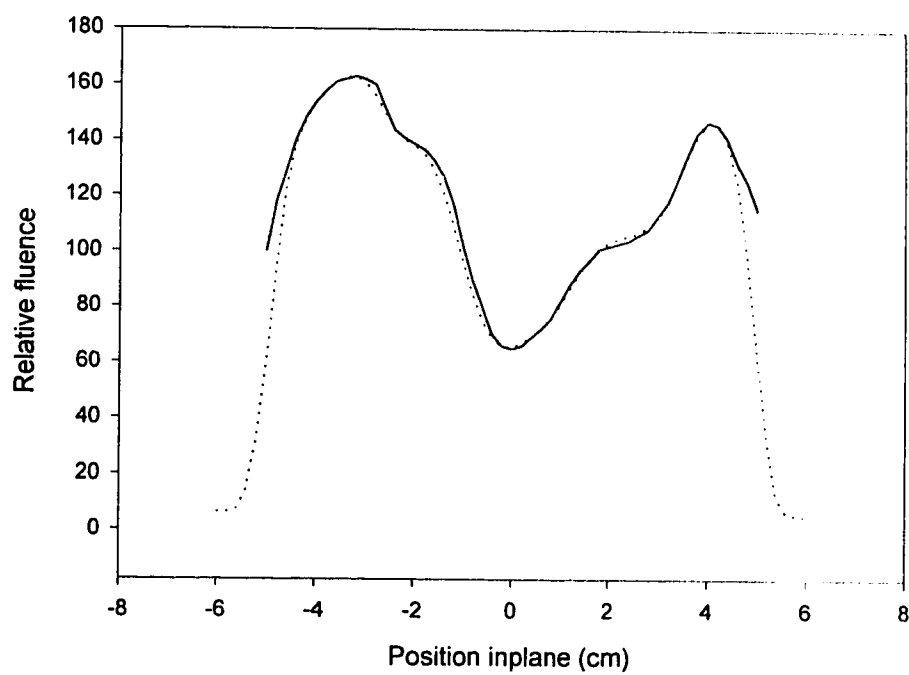


*Figure 4.32 A comparison between the desired, ideal complex in-air energy fluence profile (solid) and the profile generated by true DBD (dotted) (6 MV, Varian 2300CD, 10x10 cm<sup>2</sup> field).*



#### 4.4 Dynamic Dose and Isodose Profiles

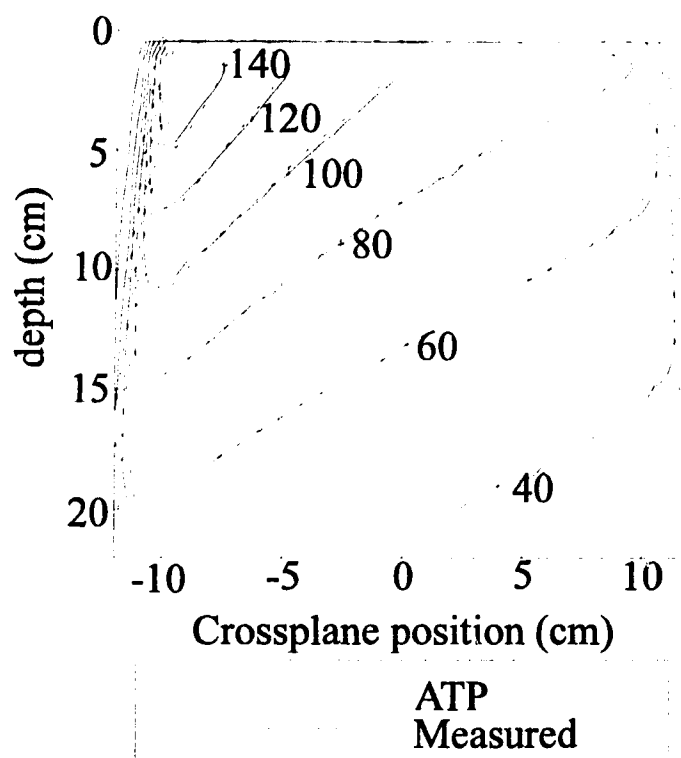


*Figure 4.33 Isodose measurement made using a with a linear ion chamber array (solid line) and calculated by ATP (dotted line) (6 MV, Varian 2300CD, 20x20 cm<sup>2</sup> field).*

Using the ATP treatment planning system to generate the dose distribution that will be produced for a given STT has already been touched on (cf. section 3.5.1.2). The comparison of ATP predictions for a Varian STT to the isodoses measured with the linear ion chamber array in phantom are quite favourable (see figure 4.33), except for areas well into the penumbral region (this is due to a problem with the modelling of the penumbra by ATP).

# Varian STT vs. CCI STT, 45deg. dyn.wdg.

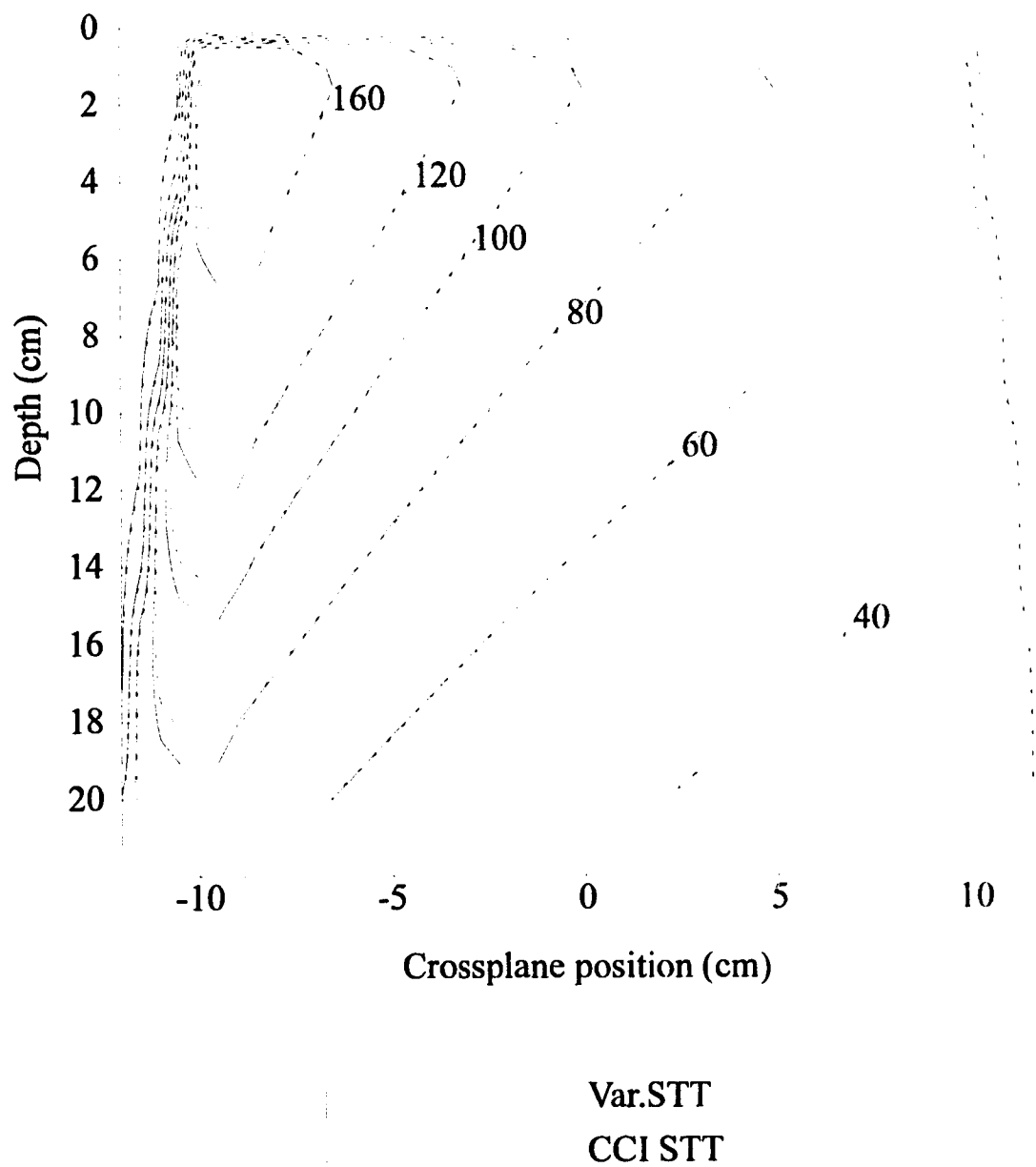


*Figure 4.34 A comparison between predicted isodose profiles for a Varian dynamic wedge and the dynamic wedge produced from an STT calculated by the model presented in this work given a desired fluence profile from measurement (assuming a 6 MV beam, 20x20 cm<sup>2</sup> field).*

The model has been tested in relation to the well-known case of the dynamic wedge. The in-air fluence profiles for a number of Varian STT generated dynamic wedges were measured with a linear ion chamber array and brass buildup caps. These profiles were corrected for their penumbra (increasing the fluence at the edges by a fraction calculated by the penumbral model based on the position of the measured point in the field) and then passed to the model to calculate the jaw motions required to produce those fluence profiles. The resulting STTs were then passed to ATP in order to check that the predicted isodose distribution in phantom was equal to that produced by the Varian STT generated dynamic wedge. The result of this calculation is shown in figure 4.34, and the results are quite favourable (aside from a minor discrepancy at the heel of the wedge, due to the technique used to remove the penumbra from the measured fluence profiles).

This technique has also been employed to predict the results for a dynamic dose delivery schedule that has been generated by the model. In the example of figure 4.35, the isodose distribution predicted to result from attempting to dynamically improve the flatness of the field at 20 cm depth is shown. This STT was then used to generate a true DBD field, and the profile at 20cm depth in phantom was measured with a linear ion chamber array.

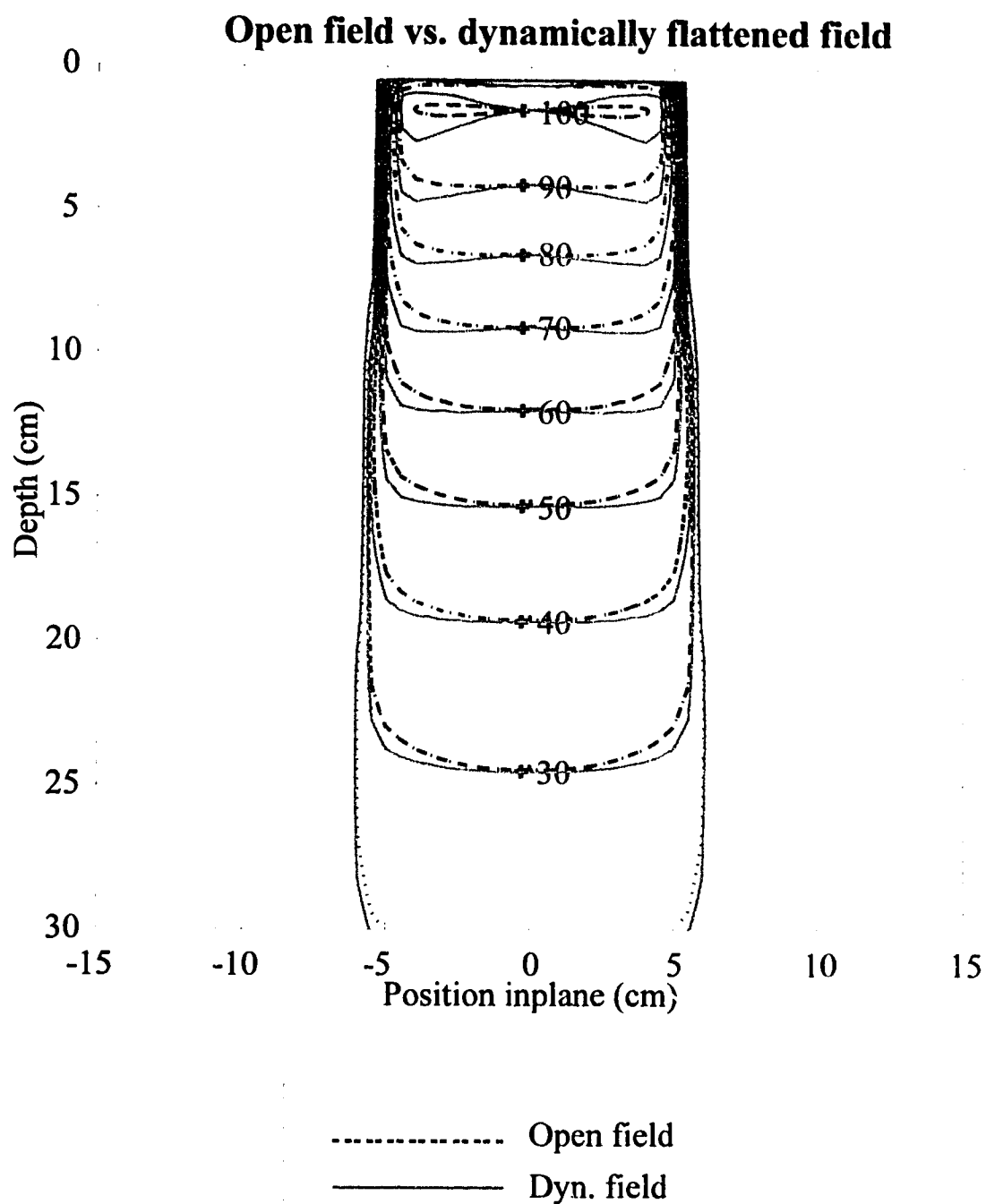


*Figure 4.35 A comparison of ATP generated isodose distributions, namely an open field and the distribution predicted for a dynamically flattened field (6 MV, Varian 2300CD, 10x10 cm<sup>2</sup> field).*

The measured dose profile at 20 cm depth for an open field using a linear ion chamber array at depth in phantom is shown in figure 4.36. A dynamic field was

designed to improve the flatness of this field, and the ion chamber array measurement of the field is shown in figure 4.37; the flatness is indeed improved, although the adherence at the field edges is still off due to penumbral effects.

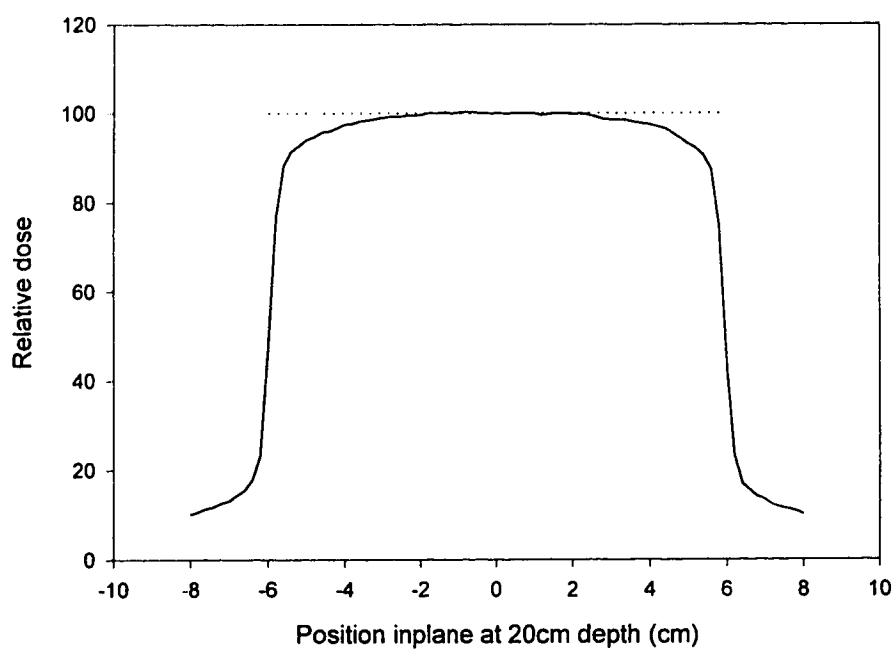


*Figure 4.36 Open field profile measured with ion chamber array at 20cm depth (6 MV, Varian 2300CD, 10x10 cm<sup>2</sup> field).*

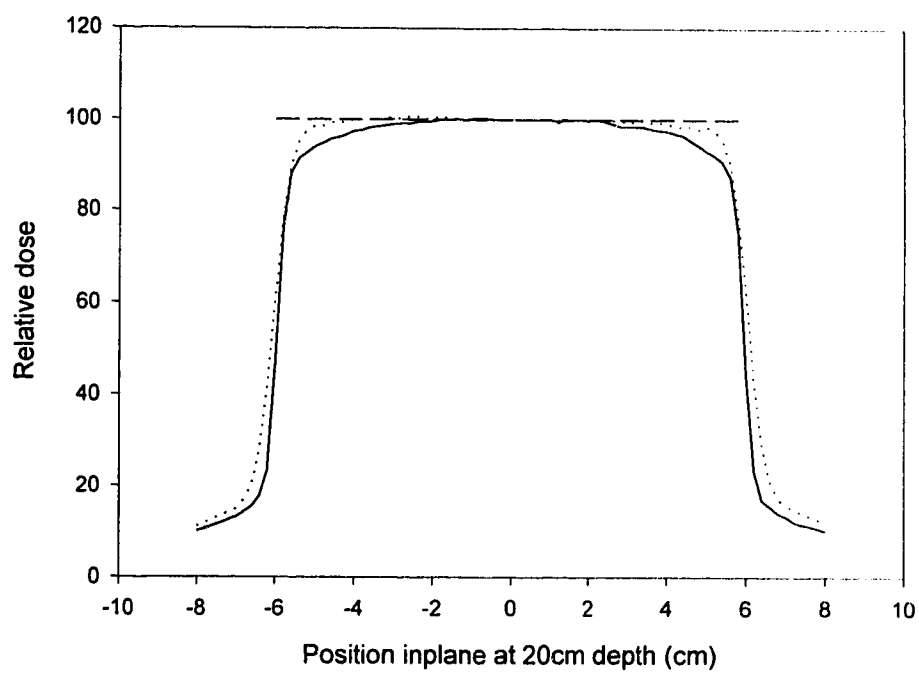


*Figure 4.37 Dynamically flattened field profile, measured with ion chamber array (dotted), 20cm depth in phantom (generated with true DBD), as well as the open field profile (solid) and the ideal desired flat profile (dashed) (6 MV, Varian 2300C'D, 10x10 cm<sup>2</sup> field).*

A dynamic treatment was also devised to produce a wedge shaped dose profile at 10 cm depth using true DBD, with a relative dose ranging from 75 to 125 (arbitrary units). The result of this treatment can be seen in figure 4.38. The maximum variance of the measured value from the desired is, aside from the region at the field edge, on the order 1 arbitrary unit (about 1.5%). This is only slightly outside the 0.5% variance one may expect due to noise in the measurement.

Another generated true DBD dynamic dose field is shown in figure 4.39. This field, a split wedge profile, shows a slightly greater variance than the first example, on the order of 2 arbitrary units (about 2%). This is due to a minor limitation with the dose calculation-iteration algorithm.

The complex profile pictured in figures 4.31 and 4.32 was also generated as a dose profile by true DBD, and the results are given in figure 4.40. The general agreement is fair (most variation less than 3-4%), limited again by limitations in the dose calculation-iteration algorithm.

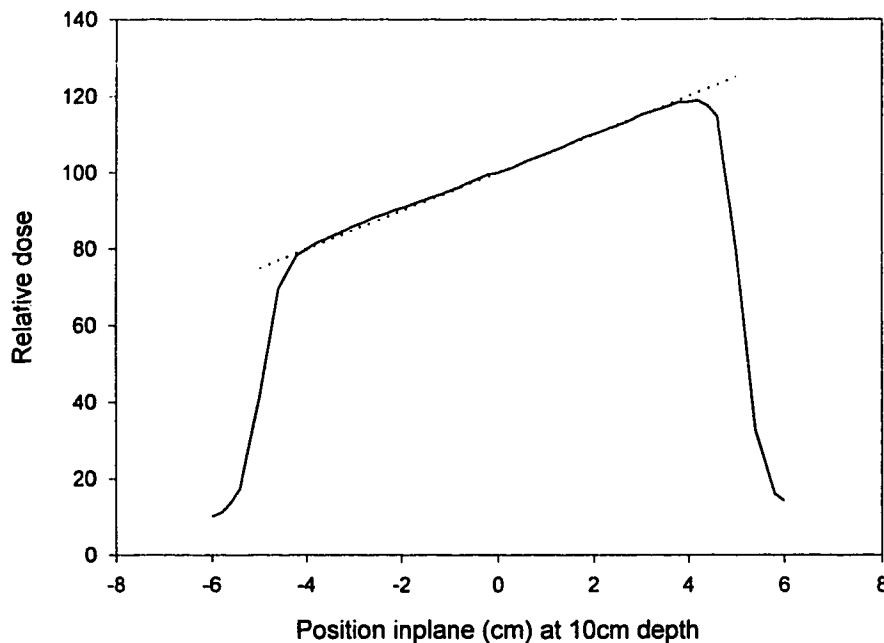


*Figure 4.38 A wedge shaped dose profile measured at 10cm depth with an ion chamber array; desired (dotted) and measured (solid), generated with true DBD (6 MV, Varian 2300CD, 10x10 cm<sup>2</sup> field).*

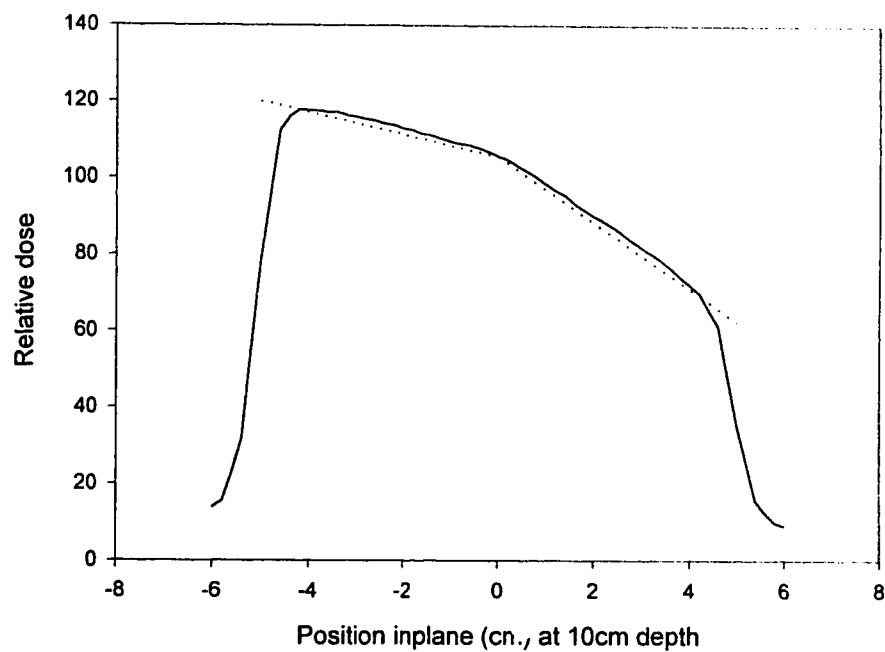


*Figure 4.39 A split wedge shaped dose profile measured at 10cm depth with an ion chamber array;) desired (dotted) and measured (solid), generated with true DBD (6 MV, Varian 2300CD, 10x10 cm<sup>2</sup> field).*



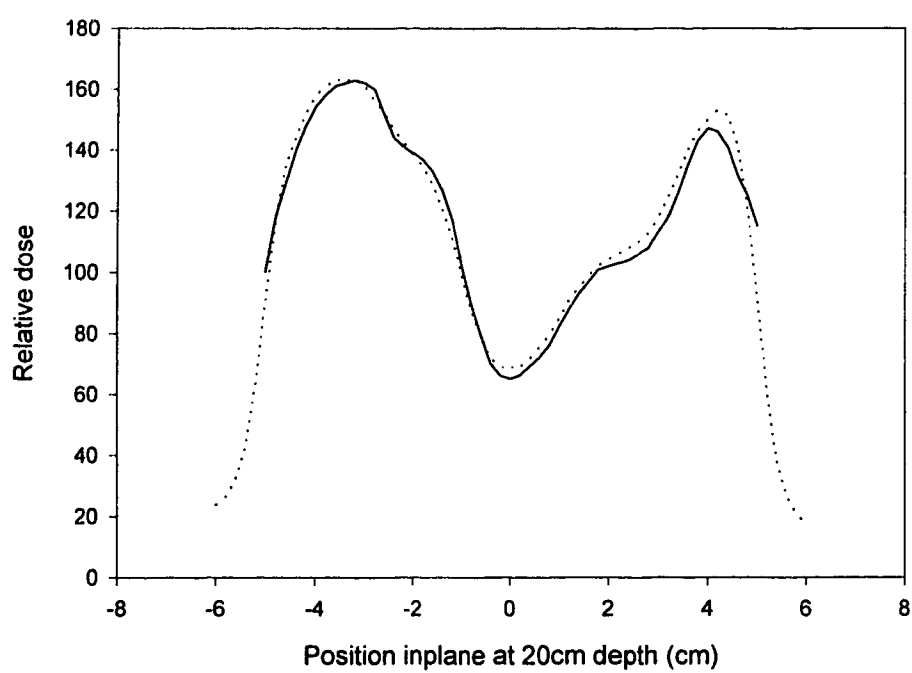


*Figure 4.40 A more complex dose profile measured at 10cm depth with an ion chamber array;) desired (dotted) and measured (solid), generated with true DBD (6 MV, Varian 2300CD, 10x10 cm<sup>2</sup> field).*

## **Chapter 5**

### **Discussion and Conclusions**

#### **5.1 Calculations**

The two models employed in this study were the simplified analytic method outlined in section 3.2.3, and the Simplex optimisation method (cf. 3.2.2.1). These techniques were compared (cf. 3.2.3) and found to produce identical results. This was expected given that there are at least two alternate proofs of the optimisation achieved by maximising jaw velocity for one jaw depending on the intensity gradient of the field (cf. 3.2.3 and [Spirou *et. al.* 1994]).

The chief limitations of the Simplex method are the calculation time, and the relative complexity of the formulation of the initial tableau for a multi-point profile. The calculation time for a 101 point profile is on the order of minutes on an IBM PC with a pentium 133 MHz processor. This calculation time also increases nonlinearly with the specification of more points to define the profile. This compares to a calculation time of seconds for the analytic approach; the analytic method is greatly preferable in terms of overall calculation time, particularly if an iterative calculation is required.

The simplified version of the analytic technique used is not truly calculating the jaw motions required, but rather the cumulative number of monitor units that have been delivered when each jaw reaches a given position. The actual jaw kinematics are unimportant in this study for both the static delivery and DBD technique. Jaw velocity and acceleration are rendered unimportant when dynamic fields are approximated by a sum of static fields. When true dynamic fields were produced, they were delivered through the use of the DBD software provided by Varian Oncology Systems<sup>5</sup>. This software calculates the required jaw velocity and dose rate in a 'black box' fashion according to user supplied data (jaw positions as a function of cumulative monitor units).

Minor modifications may be made to the model from its present form, but no major changes are indicated. Such changes would include placing minor but realistic limitations on the range of jaw separation possible (no smaller than 5 mm; this is a jaw separation limitation imposed by the present machine).

---

<sup>5</sup> Varian Oncology Systems, Palo Alto, California

## 5.2 Dosimetry

Fluence measurements were performed using both film and ion chambers. The results for the measurement of fluence with the ion chamber array and film were compared (cf. section 3.5), and yielded good agreement (see figure 4.5; figures 4.31, 4.32) when fluence smearing was taken into account.

A layer of buildup material is required for film measurements in order to screen out contaminant electrons from the beam. This introduces scattered radiation, generated within the buildup plate, hence producing “smeared” fluence measurements. Using a differential OD approach it is possible to predict the amount of smearing produced. By smearing a predicted fluence profile, the expected measured fluence profile may be generated and compared to the actual measured fluence profile. The high degree of agreement between these predicted fluence and measured fluence profiles demonstrates both the utility of this method of analysis in film fluence densitometry and the accuracy of the unsmeared predicted fluence profiles.

A small buildup cap was also required to screen out contaminant electrons when making measurements with ion chambers. The degree of “fluence smearing” produced by an ion chamber buildup cap is less than that produced by the film buildup plate due to the much smaller spatial extent of the ion chamber buildup cap. The “fluence smearing” associated with ion chamber measurements was significantly reduced by using a smaller buildup cap of greater density. As the fluence profiles measured with these smaller brass buildup caps closely matched the unsmeared predicted fluence profiles, the ion chamber measurements with these brass buildup caps were considered accurate representations of the true fluence profile.

For fluence, all dosimeters were limited by the need for some finite amount of buildup. As noted in section 4.1.1, the use of brass buildup caps gives a notable improvement in the sharpness of the penumbra. This produces a truer picture of the fluence in high gradient regions (since with a smaller buildup cap, it is less susceptible to the smearing effect pictured in figures 3.24, 3.25). For film, a thinner, higher Z buildup layer would give improved results, as is already evident with ion chamber measurements.

For future ion chamber and diode measurements of the fluence, it is possible that with mathematical smoothing of the data to reduce the amount of noise, inherent to the measurement of probe functions, that deconvolution of a measured signal is possible. Such a deconvolution would yield a truer picture of the fluence at a point than is presently available, and would allow for improved modelling of fluence penumbra.

### 5.3 Dynamic Field Corrections

The necessity of the AOF correction is quite evident, as is the ROF correction (cf. figures 4.10, 4.11 and 4.12). The penumbral correction has a limitation in that it does not appear to be possible, with imperfect collimation, to achieve perfectly sharp interfaces within a dynamic field (and it is physically impossible to do so at the field edges); despite this, it does provide improved adherence through the penumbral region of the field. The inclusion of all three of these correction factors is necessary to the production of accurate dynamic fields.

The penumbral model is borne out both by its agreement with measurements, as well as its ability to serve as a predictor of the fluence in the analysis of film and ion chamber array dosimetry.

As has been noted, the effect of the transmission of radiation through the jaws has been ignored in this work. A further refinement to the calculation would also be to include the effect of transmission through the jaws. This is thought to be a minor effect, but it would place a lower global limit on the minimum delivery within a dynamic field. The effect of such an addition has already been noted with respect to the predicted fluence for an open field (see figure 4.14).

### 5.4 Simulated DBD

In general, the results from the simulated dynamic fields were equivalent to the results of the truly dynamic fields. The major limitation of this technique was the time required for field delivery. This was due chiefly to the step size resolution required to produce a smoothly varying profile. As well, the dose resolution required for certain parts of the beam delivery schedule for the simulated dynamic field were not achievable (i.e. the schedule often called for fractional monitor units).

The results from the simulated dynamic fluence profile generation are in good agreement with the all desired profiles tested. There were also encouraging results from the simulated dynamic dose profiles films produced with simulated dynamic beam, namely the simple wedge profile, and the flattened dose profile.

The main limiting factor in the acquisition of a simulated dynamic collimation field is the relatively long time required to deliver a given field. This necessitates the use of film as it is the only practical integrating dosimeter suitable for the long data acquisition times required and for the high resolution evaluation of temporally variant fields.

The technique of simulating dynamic delivery will, in all likelihood, be abandoned in future studies in light of the availability of software allowing for true dynamic control over machine parameters.

## 5.5 True DBD

The results from the true dynamic fluence profile generation are in excellent agreement with all the desired profiles tested. The results from the generation of true dynamic dose profiles are also in good agreement with all the desired profiles tested.

Most of the true DBD results were measured with the ion chamber array, although there are a number of comparisons that can be made with films. The results from the use of the true DBD are very close to those which were realised with the use of summed static fields (see figure 4.26 and 4.27), for identical delivery schedules and dosimeters (film, in this case). The agreement of the fluence profiles with the desired profiles is better with the ion chamber array than is seen with film, due mostly to negligible energy response of ion chambers (film response can vary with processing conditions, batch characteristics, and it does show energy dependency -- it can, in other words, be quite noisy).

The true dynamic beam delivery has the advantage of delivering a dynamic beam schedule as a linear interpolation between specified points (instead of being delivered as discrete steps), and doing so in a reasonable time. The linear interpolation between the defined points is not a problem, as this was always assumed to be the case, and it would only pose a problem if the defining spatial resolution for a dynamic field were particularly low.

## 5.6 Overall Model Evaluation

The computational implementation of the model has proved to be a flexible and rapid means of generating dynamic beam delivery schedules for disparate desired dynamic beam profiles. The final results of this work from dosimetric investigations have shown that a number of correction factors are necessary in order to realise a given output for a dynamic field. The results from the generation of fluence profiles show the model to yield excellent results for a variety of fields once these factors are taken into account. The final results with dose profiles in phantom are quite encouraging as well, and any small discrepancies are due to minor limitations of the dose calculation algorithm presently employed (notably the inherent problems in using TAR values collected on the CAX for off-axis point dose calculations).

## 5.7 Future Work

This work may serve as the basis for an extension to the case of 2D and 3D dynamic fields. This could take the form of using the techniques outlined herein to deliver numerous 1D ports to achieve some net 2D or 3D dose distributions in phantom.

For the production of a single 2D field, the desired dose distribution may be realised using the dynamic driving of the leaves of an MLC across the field while the

beam is on. The required motions for each opposing leaf pair could likely be calculated using a minor variant of the model described in this work. In the absence of true dynamic control over the leaves, a summation of static fields may be employed as was done for the early work outlined in this thesis. A particular 2D dose distribution may also be realised using multiple orthogonal passes of opposing jaws (or passes at non orthogonal angles) to achieve some net desired profile. An equality constraint may be placed on the production of such a field much like for the 1D case, where the net to any given point is the sum of intensity during the time that point is exposed. A numerical optimisation routine may be employed in determining the delivery schedule in the absence of an analytic technique.

For 3D treatments, it is possible that a numerical optimisation technique may be required to calculate the beam profiles and arrangements to achieve the best possible adherence to a given 3D PTV. Each of the beams required may have some desired 2D in air fluence profile, and these may be produced using the techniques described above.

As well, dynamic control over numerous machine parameters is now available, and the modulation of a number of these parameters may be employed in achieving some desired dose distribution (cf. section 1.4).

## Bibliography

AAPM "A protocol for the determination of absorbed dose from high energy photon and electron beams" *Med. Phys.* 10:741-771 (1983)

Anderson, D.W.; St. George, F. "Comparison of film and ion chamber systems for depth dose measurements for a 25 MV beam" *Phys. Med. Biol.* 24:636-638 (1979)

Attix F.H. "Introduction to Radiological Physics and Radiation Dosimetry" New York, U.S.A. John Wiley & Sons (1986)

Björngård, B.E.; Kijewski P.K. "The potential use of computer control to improve dose distributions in radiation therapy" *Proc. 5th Int. Conf. on the Use of Computers in Radiation Therapy*. ed E S Sternick (Hanover, NH: The University Press of New England). pp 110-124. (1976)

Carrier, R.; Cormack, D.V. "Physics of Radiation Therapy and Medical Imaging - An Historical Overview" *Physics in Canada* 51:162-168 (1995)

Chui, C.; Mohan, R.; Fontenla, D "Dose computations for asymmetric fields defined by independent jaws" *Med. Phys.* 15:92-95 (1988)

Convery, D.J.; Rosenbloom, M.E. "The generation of intensity modulated fields for conformal radiotherapy by dynamic collimation" *Phys. Med. Biol.* 37:1359-1374 (1992)

Evans, R. "The Atomic Nucleus" Malabar, Florida, Krieger Publishing Co. (1955)

Field, G.C. "Dose Calculations for Megavoltage Photon Beams Using Convolution" Master's thesis, University of Alberta (1988)

Gill, P.E.; Murrey, W; Wright, M.H. "Practical optimization" London, U.K. Academic, 1981

Hale, J.I.; Kerr, A.T.; Schragge, P.C. "Calibration of film for accurate megavoltage photon dosimetry" *Medical Dosimetry* 19:43-46 (1994)

Huntzinger, C.J. "Dynamic wedge: a physicist's perspective" in Proceedings of the Twentieth Varian Users Meeting, Manchester (1994)

International Commission on Radiation Units and Measurements "Determination of Absorbed Dose in a Patient Irradiated by Beams of X or Gamma Rays in Radiotherapy Procedures" ICRU Report 24, Washington, D.C. (1976)

International Commission on Radiation Units and Measurements "Prescribing, Recording, and Reporting Photon Beam Therapy" ICRU Report 50, Washington, D.C. (1993)

International Electrotechnical Commission "Medical Electron Accelerators - Functional Performance Characteristics" IEC Performance Standard 976, Geneva (1993)

Jaffray, D.A.; Battista, J.J.; Fenster, A.; Munro, P. "X-ray sources of medical linear accelerators: Focal and extra-focal radiation" *Med. Phys.* 20:1417-1427 (1993)

Johns, H.E.; Cunningham, J.R. "The physics of radiology" 4th ed. Springfield, IL: Charles C. Thomas (1983)

Johns, H.E.; Whitmore, G.F.; Watson, T.A.; Umberg, F.H. "A system of dosimetry for rotation therapy with typical rotation distributions" *J. Can. Assn. Radiol.* 4:1-11 (1953)

Karzmark, C.J. "Advances in linear accelerator design for radiotherapy" *Med. Phys.* 11:105-126 (1984)

Khan, F.M. "The physics of radiation therapy" Baltimore: Williams and Wilkins (1994)

Kijewski, P.K.; Chin, L.M.; Bjärngård, B.E. "Wedge-shaped dose distributions by computer-controlled collimator motion" *Med. Phys.* 5:426-429 (1978)

Kollar, J. "Evaluation and Modification of a Differential SAR Dose Calculation Algorithm" Master's thesis, University of Alberta (1996)

Krane K.S. "Introductory Nuclear Physics" New York, U.S.A. John Wiley & Sons (1988)

Kunzi, H.P.; Tzschach, H.G.; Zehnder, C.A. "Numerical Methods of Mathematical Optimization" New York, NY Academic Press (1971)

Leavitt, D. "Dynamic beam shaping" *Medical Dosimetry* 15:47-50 (1990a)



Leavitt, D.; Martin, M.; Moeller, J.; Lee, W. "Dynamic wedge field techniques through computer controlled collimator motion and dose delivery" *Med. Phys.* 17:87-91 (1990b)

Leavitt, D. "Advances in dynamic wedge technique" in Proceedings of the Twentieth Varian Users Meeting, Manchester (1994a)

Leavitt, D. "Clinical aspects and experience with dynamic wedge" in Proceedings of the Twentieth Varian Users Meeting, Manchester (1994b)

Leavitt, D. "Ion chamber and film densitometric techniques for dynamic wedge" in Proceedings of the Twentieth Varian Users Meeting, Manchester (1994c)

Lichter, A.S. "Three dimensional conformal radiation therapy: a testable hypothesis" *Int. J. Radiat. Oncol. Biol. Phys.* 21, 853-855 (1991)

Loewenthal, E.; Loewinger, E.; Bar-Avraham, E.; Barnea, G. "Measurement of the source size in 6- and 18-MV radiotherapy linac" *Med. Phys.* 19:687-690 (1993)

Loshek, D.; Parker, T. "Dose calculations in static or dynamic off axis fields" *Med. Phys.* 21:401-410 (1994)

Lutz, W.R.; Nasser, M.; Bjarngard, B.E. "Evaluation of a beam-spot camera for megavoltage x rays" *Med. Phys.* 15:614-617 (1988)

Metropolis, N.; Rosenbluth, A.; Rosenbluth, M.; Teller, A.; Teller, E. "Simulated annealing" *J. Chem. Phys.* 21:1087-1097 (1953)

Munro, P.; Rawlinson, J.A.; Fenster, A. "X-ray sources of medical linear accelerators: Focal and extra-focal radiation" *Med. Phys.* 15:517-524 (1988)

Panofsky, W.K.H.; Philips, M. "Classical Electricity and Magnetism" 2<sup>nd</sup> edition, Reading, Mass., Addison-Wesley (1962)

Press, W.H.; Flannery, B.P.; Teukolsky, S.A.; Vetterling, W.A. "Numerical recipes" New York, NY Cambridge Press (1989)

Rubin, P. (Ed.) "Clinical Oncology" Philadelphia, W.B. Saunders Co. (1993)

Spencer, L.; Attix, F. "A theory of cavity ionization", *Rad. Res.* 3:239-249 (1955)

Spirou, S.V.; Chui, C.S. "Generation of arbitrary intensity profiles by dynamic jaws or multileaf collimators" *Med. Phys.* 21:1031-1041 (1994)

Svensson, R; Källman, P; Brahme, A "An analytical solution for the dynamic control of multileaf collimators " *Phys. Med. Biol.* 39:37-61 (1994)

Urtasun, R.C. "Does improved depth dose characteristics and treatment planning correlate with a gain in therapeutic results?" *Int. J. Radiat. Oncol. Biol. Phys.* 22, 235-239 (1992)

Waggener, R.G. (Ed.) "Handbook of medical physics, vol. 1" Boca Raton, Florida CRC Press (1982)

Wilkinson, J.H.; Reinsch, C. "Handbook for Automatic Computation" New York: Springer-Verlag (1971)

Williamson, J.; Khan, F.M.; Sharma, S.C. "Film dosimetry of megavoltage beams: a practical method of isodensity to isodose curve conversion" *Med. Phys.* 8:94-98 (1981)

Yu, C.; Symons, M.; Du, M.; Martinez, A.; Wong, J. "A method for implementing dynamic photon beam intensity modulation using independent jaws and a multileaf collimator" *Phys. Med. Biol.* 40:769-787 (1995)